DYNAMIC EVALUATION OF THE SOLAR CHIMNEY

by

Jean-Pierre Rousseau

Thesis presented in partial fulfilment of the requirements for the degree of Master of Engineering at the University of Stellenbosch

Study leader: Prof G.P.A.G van Zijl

December 2005

DECLARATION

I, the undersigned, hereby declare that the work contained in this document is my own original work and that I have not previously in its entirety or in part submitted it at any university for a degree.

Signature:_____ Date:_____

SYNOPSIS

Previous studies on the solar chimney have shown that its structural integrity might be compromised by the occurrence of resonance. A structure may displace excessively when a load of the same frequency as a structural eigen-frequency is applied. The wind gust spectrum peaks near the solar chimney's fundamental resonance frequency. This phenomenon poses a reliability threat, not only to the solar chimney, but also to all high-rise, slender structures.

Structural dynamics describe the response of a structure to a varying load. The dynamic equation incorporates four terms that bind the factors responsible for resonance: kinetic energy, dissipated energy (damping), stiffness energy and input energy (loading). After a brief literature study on classical chimney design procedures, the study scrutinises each of these terms individually in the context of the solar chimney as designed to date.

A dynamic analysis is undertaken with all the above-mentioned parameters as defined and estimated by the study. The results from the analysis show amplifications of approximately three times the static displacements. In load cases where the wind direction inverts along the height, higher eigen-modes are excited. However, the most severe dynamic amplification occurs at the fundamental eigen-mode. In the context of solar chimney research, this study brings valuable new insights regarding the dynamic behaviour of the chimney structure to the fore.

OPSOMMING

Vorige studies van die Sontoring het aangedui dat die strukturele integriteit in gedrang mag wees vanweë resonansie. Wanneer 'n ossilerende las, van dieselfde frekwensie as 'n strukturele eigen frekwensie, op 'n struktuur inwerk, kan oormatige verplasings voorkom. Die spektrale verdeling van wind piek in die omgewing van die fundamentele frekwensie van die sontoring. Hierdie verskynsel bedreig nie net die betroubaarheid van die Sontoring nie, maar bedreig alle slank, hoog-reikende strukture.

Struktuur dinamieka omskryf die reaksie van a struktuur weens 'n variërende las. Die beweginsvergelyking inkorporeer vier terme wat die faktore wat resonansie veroorsaak, saam bind: versnellende massa, ge-absorbeerde energie (demping), styfheid en las energie. Na 'n kort literatuurstudie met betrekking tot vorige ontwerpsprosedures van torings en skoorstene, word elk van die dinamiese faktore fyn bestudeer in die lig van die huidige sontoring ontwerp.

'n Dinamise analise word uitgevoer op die struktuur met die bogenoemde faktore in ag genome soos nagevors in hierdie studie. Die resultate dui op ossilasie-amplitudes van ongeveer drie maal die statiese las toestand verplasings. Hoër eigen modusse word opgewek deur las toestande waar die wind van rigting verander oor die hoogte van die struktuur. Die mees kritiese geval is egter steeds die resonansie van die eerste eigen modus. In die konteks van sontoring navorsing bring die studie belangrike nuwe insigte met betrekking tot die dinamiese gedrag van die stuktuur na vore.

ACKNOWLEDGEMENTS

Professor G.P.A.G van Zijl, my promoter.

Dr. Phillippe Mainçon, my teacher and mentor in the theory of structural dynamics.

Dr. Jan Wium, for practical advice and encouragement.

Cobus van Dyk, for his enthusiasm concerning the solar chimney project.

Billy Boshoff, for assisting me in developing the gust accelerometer.

Riaan Smit at the South African Weather Bureau Cape Town, for taking the time to chat with me.

My ouers, vir hulle deurlopende ondersteuning en aanmoediging.

My vriendin en regterhand, Imke, vir haar morele ondersteuning en bystand die afgelope jaar.

TABLE OF CONTENTS

LIST OF FIGURES AND TABLES

List of Figures:

List of Tables:

KEY TO USE THIS REPORT

References in the text appear in brackets. They show the author(s) and the published date. In the references section at the end of this report, all the references are listed in alphabetical order.

Appendices are located at the end of the report, after the "References" section.

When passages from the literature are quoted, the text might be slightly adapted for more comfortable reading. Such passages are printed in square brackets.

Matrices are indicated with double bars over the symbol in all equations whereas vectors are indicated with single bars.

All digital data referred to in the text are available on a compact disc that should accompany this report.

Chapter 1

INTRODUCTION AND BACKGROUND

1. 1 Higher and higher

The time of super structures is upon us. No more fictional star wars like high-rise skyscrapers, fiction is turning into reality. With the assistance of computer power today, engineers are able to design buildings of larger proportions than before. There is no need for over-simplification anymore. Today it is possible to simulate a physical structure, in the finest of detail, on a regular desktop pc. Civil Engineers have acquired the ability to predict structural behaviour with accuracy, based on design and computational modelling. Only in exceptional cases it is required to study behaviour by physical, scale modelling. And it is not surprising that developers have the confidence to go wider, larger, and higher. But is it possible with our advanced design capabilities and all our detailed recordings and descriptions of nature to reach heaven today, as the builders of the tower of Babylon failed to do thousands of years earlier?

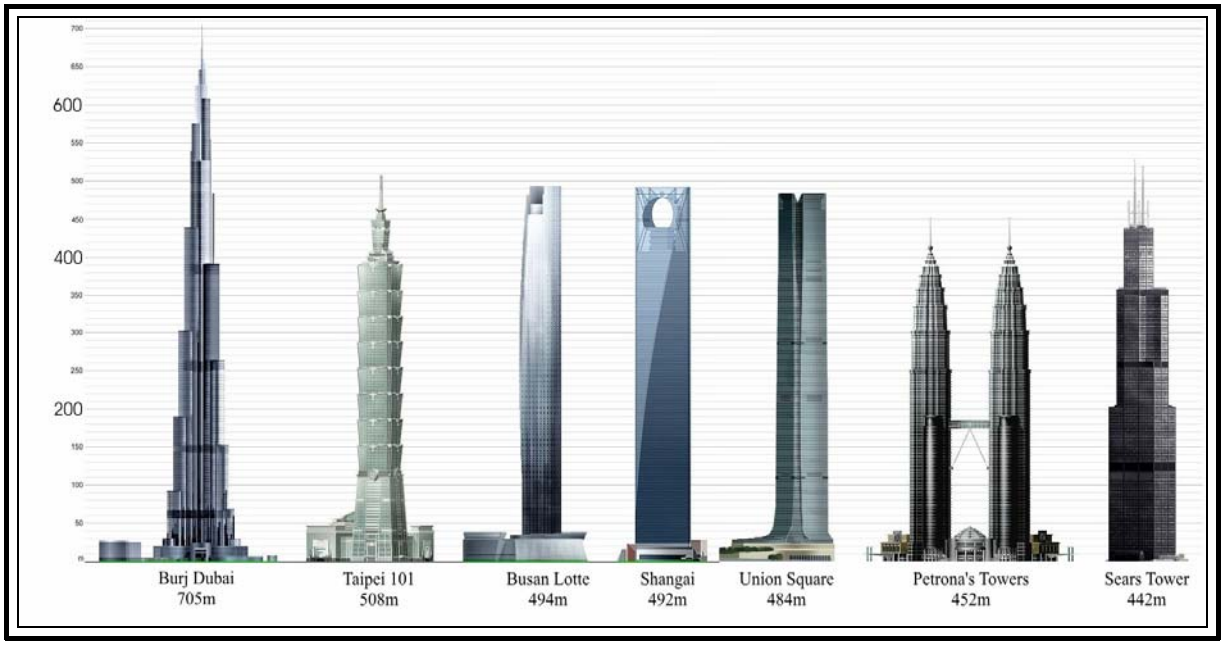

Figure 1-1: The tallest skyscrapers on earth (SkyscraperPage.com, 2005)

Indeed it seems possible. Recent advancements in the height of skyscrapers have brought new meaning to the saying 'the sky is the limit'. In 1998 Malaysia took the lead as the country with the tallest building on earth, Petrona's Twin Towers. It towers over the city of Kuala Lumpur at 452m. But plans for even higher structures are in the pipeline. Shanghai's World Financial trade centre will

stand 492m tall. In Taipei, the Taipei 101 tower will be 508m tall and the new freedom tower in New York is estimated at 541m.

More recently, United Arab Emirates announced the commission of the Burj Dubai, a tower planned at heights of above 600m. With the antenna, the current proposed height is 705m, but speculation has it that the structure might eventually stand 900m tall.

Figure 1-2: The proposed solar chimney near Upington

In the past ten years universities in Germany, Australia and South Africa have been doing research on the feasibility of a Solar Updraft Tower, or solar chimney. The system will produce energy by means of updraft airflow from under a glass collector through a chimney, turning turbines that generate power. One such system can generate at a constant rate of 200MW throughout the day and night. Schlaich Bergermann und Partner is the leading engineering company in promoting the concept to potential energy users (Schlaich *et al*, 2004).

The challenging component of the system is the tower or chimney. The planned reinforced concrete chimney will be a freestanding structure reaching to a height of 1500m. According to Schlaich Bergermann und Partner [towers 1000m high are a challenge, but they can be built today]. "What is needed for a solar updraft tower is a simple, large diameter hollow cylinder, not particularly slender, and subject to very few demands in comparison with inhabited buildings." (Schlaich *et al*, 2004). Since the publication of the first concept the height has increased to 1500m, where a higher efficiency will be reached. Figure 1-2 shows the scale of the solar chimney.

But how high can we go? Is the sky literally the limit? How critical may the demands of a 1500m tall structure be? This study will investigate one such restraining factor of the solar chimney, namely resonance when subjected to gusting wind loads.

1. 2 Background to the Solar Chimney

After the oil crisis in the mid seventies the world became aware of the limitations of natural resources and scientists and engineers started seeking elsewhere for sources of energy. Electricity in motor vehicles and household heating seemed like a good alternative for clean power, but most electricity plants at that stage were still dependent on limited natural resources such as coal and oil. Not only did they pose a threat to the depletion of these resources, but they were also criticised by ecologists for the air pollution they cause. Although hydroelectric energy seemed like a good solution, it is still dependant on a natural resource, water, which is subject to droughts and regional water crisis. Water, as a source of electric energy, has limited potential world wide. Nuclear power was another cleaner option, but the radiation risk and the ecological threat of nuclear waste ensured a decline in popularity for this energy source. These types of power plants are expensive compared to coal and gas as is illustrated by the American Wind Energy Association in table.

Power generation type	**Cost (US cents per kWh, 1996)**	**South African utilization**
Coal	4.8	92.4%
Gas	3.9	-
Hydro	5.1	1.5%
Nuclear	11.1	6.1%
Wind	4.0	-

Table 1-1: US electricity generation costs (American Wind Energy Association) and South African power utilization (Eskom).

The only utilized clean and natural, resource-independent energy generators are solar panels and wind turbines. In Germany wind turbines contribute 15% of the total energy supply. Both of these methods work well for household or estate use, but their capacity is too limited to effectively supply enough electric energy to supply a country. Figure 1-3 presents power output values of the solar chimney according to Schlaich.

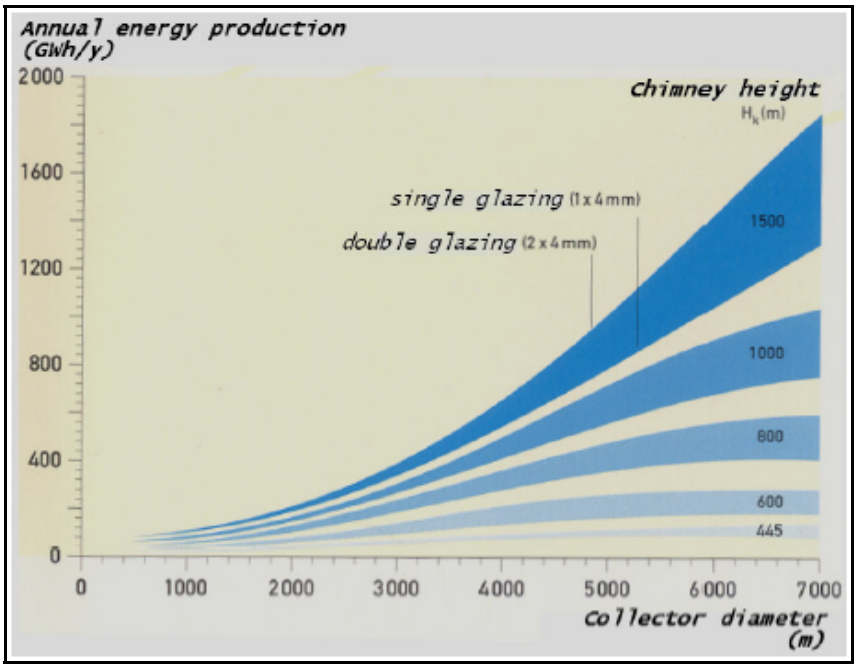

Figure 1-3: Performance curve as a function of size (Schlaich, 1995)

It was with these limitations in mind that Professor Jörg Schlaich conceived the concept of the solar chimney. By combining the technology of wind energy and solar energy generation, it is possible to generate electricity on a virtually continuous basis that will be more environmentally friendly than fossil fuel plants, operate with a non-deplete-able energy source and would be more energy effective than other non-deplete-able energy-source generators such as wind turbine- and solar panel plants. Although the concept dates back to 1931, Prof Schlaich was the first to envision such a plant on a larger scale. From 1986 until 1989 a prototype was operated in Manzanares, Spain, with a peak output of 50 kW. The chimney was 200m high with a collector diameter of 240m. This prototype proved the validity of the concept, but the power output is still not significant enough for large-scale energy supply. To deliver 200MW of electricity, the whole system needs to be implemented on a larger scale. Since 1990 engineers and scientists have been studying aspectas of solar chimney energy generation to reach this goal. By 2000 the efficiency of the system was well known, the necessary dimensions were well defined, and the financial credibility of such a project well debated.

The peak power output should be achieved with a chimney of 1500m in height and a collector 7000m in diameter (see figure 1-3) according to Schlaich (1995). With these dimensions the power output is large enough to be compared to the efficiency of small coal-fired power plants and small nuclear plants. The concept was presented to various countries around the world with the hope that someone somewhere would consider funding the construction of a full-scale prototype. It was during this marketing campaign that more questions were raised on the reliability of the project. As

mentioned earlier, the fathers of the solar chimney concept gave little attention to the scale of the structure they wanted to build. In their minds it was a fairly simple matter: construct an upright cylinder 1500m tall in the middle of a desert. But to a structural design engineer such a request is not as simple as it seems. And with questions such as the construction feasibility, a new generation of research studies was undertaken concerning the structural viability of the solar chimney.

Stellenbosch University has participated in the project for numerous years, working closely with their German colleagues searching for solutions regarding the physical feasibility of the system. The departments of Mechanical, Electrical and Civil engineering have all contributed valuable research studies on the subject. In the past 6 years the following research has been done regarding the structural validity of the chimney:

Structural integrity of a large-scale solar chimney (C. van Dyk, 2002)

The realization of the solar chimney inlet guide vanes (C. van Dyk, 2004)

Optimization of wall thickness and steel reinforcing of the solar chimney (M. Lumby, 2003)

The development of ring stiffener concept for the solar chimney (E. Lourens, 2004)

Wind effects on the Solar Chimney (L. Alberti, 2004)

These studies placed the complexity of engineering such a structure under the spotlight, but all of these aspects are related to design variables, which are concrete and very possible to define with enough research and detailed design. The Australian company, EnviroMission, has also embarked on similar investigations. The company owns the exclusive license in Australia to build such a plant, and aim to be operational within five years. Their American counterpart, SolarMission Technologies Inc, has already identified sites in Arizona in the US to construct these power plants. In South Africa, the Northern Cape has been identified as a potential site, should such a project realise. The South African initiative proposed a solar chimney plant near Upington (see figure 1-2) at dimensions of 1500m height and 7000m collector-diameter.

1. 3 Objective of the study

As mentioned in the previous section, previous research on the structural integrity of the chimney focused on static parameters or local dynamic effects. These studies have indicated that the construction of such a large chimney might be possible. However, the conditions regarded in these analyses are ideal, neglecting complex environmental actions. Although the danger of resonance

due to wind loads was identified, simplified methods of wind loading were used, probably conservative. Environmental actions should be characterised to refine the prediction of the response of the structure. Thus, the limit of the domain of applicability of engineering models has been reached and must be extended to prove the integrity of the solar chimney tower.

In structural engineering designs this is not a surprising phenomenon. Modern engineering analysis mainly deals with a load, a structural stiffness, and a response due to the load. From the response, stresses can be calculated and by iteration, structural members' stiffness can be modified accordingly. Loads comprise of live loads and dead loads. Dead loads are easy to characterise, as they are the results of weights of members or other equipment on the structure. Dynamic objects, things that move, impose live loads. This can include anything from people to cranes, even furniture, as these tend to be moved over larger time intervals as well. But live loads also include the forces of nature on a structure: Snow, precipitation, earthquakes and wind. Usually, for simplification purposes, engineers deal with these forces as equivalent static loads. The safety factor is increased to a satisfactory number to compensate for any effect that may be overlooked. The design may be regarded as conservative but safe. Many modern-day building codes apply this simplified method of dealing with loads to dynamic cases. In most cases the simplification is justified, but in some cases, conservative static loads cannot compensate for dynamic excitation.

On the 7th of November 1940, the engineering world was rocked by the collapse of the Tacoma-Narrows-bridge in the United States, Washington (see figure 1-4). The wind that caused the collapse was far from the strength and speed of the design wind, but the pulsation of the wind load made the structure resonate. Over the span of a few hours the vibration became severe enough for the bridge deck to collapse (Smith, Doug, 1974).

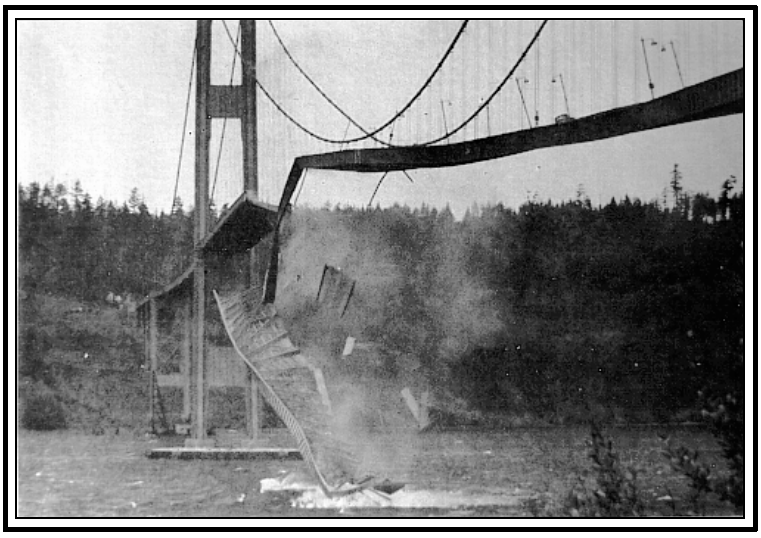

Figure 1-4: The Tacoma Narrows bridge disaster (Smith, Doug, 1974)

In 1906 San Francisco was hit by devastating earthquake. It measured about 8.25 on the Richter scale, and demolished 25 000 buildings. Although fires destroyed most of the buildings, some of the taller buildings collapsed due to movement at their bases (EyeWitness to History, 1997). With the rising popularity of skyscrapers, engineers realised that this rare but devastating force requires more sophisticated modelling than the mere consideration of static loads and load factors.

But despite the realization of these natural forces, man is still arrogant when it comes to the design of super-structures. Modern codes still allow only a static wind load, often not requiring further investigation with dynamic analyses, although some international codes make provision for these methods. It is only in the past few decades that earthquake design codes started looking at eigen-mode-characteristics of buildings and defining loading spectra's for earthquakes. But even these methods are simplified and generalized.

This study will investigate beyond the building-code requirements with respect to the integrity of a super-structure such as the solar chimney. How valid are the design requirements of reinforced concrete chimneys at the scale of the solar chimney, and how much is known about atmospheric behaviour up to 1500m? How will dynamic loads affect the tower, how resistant will it be to resonance? To find concrete answers to these questions are difficult. This study does, however, embark on a journey through the theme of dynamics, not necessarily to find concrete answers, but to gain a better understanding of the danger of resonance that might threaten the stability of the solar chimney structure.

1. 4 Limitations of the report

In this document the response of the chimney to certain load cases is simulated with certain assumptions made with regard to the chimney's structural characteristics. Therefore the limitations of the report can be summarised in four statements:

The assumptions made with regard to the structural modelling of the chimney include the meshing of the structure into elements, the way in which constraints are applied with regard to stiffeners, etc. All these assumptions will be mention in chapter 3; however, it is noteworthy to mention that they are based on previous structural studies of the solar chimney. Thus this report is limited to a single geometry and simulation representation, for it is not the purpose to investigate the physical structural design, but rather how a particular design would react to certain dynamic loadings.

The second limitation of this investigation is the accuracy of the damping characteristics of the chimney. This will be explained in detail in chapter 4. The effect of estimated modal damping

values is studied rather than the true damping itself. These estimations will be validated with literature references where appropriate. This report will therefore characterise the effect of modal damping rather than to assess it accurately.

Regarding the loads, this study will not investigate the possibility of earthquake loads, firstly because it is a study field complex enough to require a study in itself and secondly, the South African solar chimney proposal is planned to be built in an area with a small seismic risk. Therefore the report will only focus on wind and gravity loading.

Lastly, meteorological activity is stochastic in nature and thus difficult to predict in static terms. It is impossible to test the chimney for all possible dynamic load cases. Therefore analyses will be performed in worst-case scenarios, which are unlikely to occur, and several simplified dynamic load cases, based on meteorological information of the area. This can only give an indication of what might happen in the case of certain weather behaviour, but it cannot be stated that these behaviours would necessarily occur. The probability of such an event is a statistical problem, which will not be covered in detail in this report.

1. 5 Plan of development

The purpose of this chapter is to give the reader an introductory sketch of the subject of this report. It highlights the importance of such a study in today's engineering world, but also lays out the boundaries of investigation regarding the topic.

The next chapter will conduct a short literature study in previous design strategies on reinforced concrete chimneys and towers (hereafter referred to as RCC). It will also comment on the validity of these methods by applying them to the solar chimney and comparing results with a fully meshed finite element model.

The third chapter will describe the detailed finite element model, and give reasons for the choice of elements, meshing and constraints. It will confirm these choices by means of mathematical arguments as well as iterative computations. The mathematics behind eigen-values and modal reduction of the degrees of freedom will also be explained and commented on. The phenomenon of mass participation will also be discussed.

Chapter four will deal with the dynamic characteristics of the model. A short literature study will describe different types of damping and define the way in which it affects large structures. The influence of reinforcement will be looked at and a mathematical procedure to compute Raleigh

damping with eigen-modes will be evaluated. From these investigation values for the modal response analysis will be suggested.

Chapter five will conduct a brief investigation into the dynamics of wind gusts. Consulting literature, and developing an instrument to measure wind gusts a gust wind spectrum will be developed. Different load cases will be decided upon based on upper air measurements taken at Upington during the last two years.

The sixth chapter will look at the results from the modal response analysis and the different load cases. Significant results will be highlighted, explained and commented on.

The last chapter will give a summary of the findings and the knowledge gained throughout the study. It will also comment on the implications of these findings, and will make recommendations on further research regarding the field.

Chapter 2

LITERATURE STUDY: CHIMNEY AND TOWER DESIGN

2. 1 A Brief History

Chimneys and towers have been built, designed and tested for millenniums. The earliest reference of a tall chimney was Towsends chimney at Port Dundus, Glasgow (Pinfold, 1975). It stood 143m tall and was built of brickwork. Since the invention of reinforced concrete, it has also been applied in chimneys and towers extensively. In 1873 the first concrete chimney made its appearance at Sunderland. Only 19m high, it was built with one part of cement, five parts of gravel and sand. No reference is made to the use of reinforcement. By 1907 some 400 concrete chimneys had been built in the USA, as reported by Sanford E. Thompson to the Association of Portland-Cement Manufacturers. Industrial chimney heights settled at around 100m, and were the tallest concrete structures for a while, until the skyscraper buildings started overshadowing these structures in the early 1920's. But the science behind chimney design developed independently of concrete skyscrapers. Modern industrial tower designers have to deal with problems such as thermal variations over the height, chemical reactions with the building material etc. Modern TV towers have a new spectrum of criteria to be met regarding broadcasting equipment (figure 2-1).

Figure 2-1: The Ostankino tower (540m), Emley Moor tower (329m) and the CN tower (550m)

It was not until the development of radio and television technology that the height factor in tower structure design came to the forefront once more. The 1970's saw a boom in the construction of radio and television towers world wide, the one being taller than the other. In Moscow, Russia, the

Ostankino tower was completed in 1967 at 540m, and held the world record as the tallest tower for nearly a decade. The Emley Moor tower in the UK was completed in 1970 at a height of 329m. And in 1974 the CN tower in Toronto became the tallest freestanding structure in the world, upholding this title to this day. At 550m it towers above the city skyline and weighs 130 000 tonnes. Most of these types of towers have observation decks or revolving restaurants and are therefore under high constraints with regard to movement.

Both towers and chimneys are slender structures. They are the best examples of similar structures to the solar chimney. It is therefore important to study the design methods of these structures in the light of the solar chimney design, as these structures' main load source is also wind. This chapter will look at what techniques are useful in the solar chimney investigation, and what assumptions can or cannot be made.

2. 2 Defining resonance modes

The first important characteristic of a structure that is subject to dynamic loads is its modes of resonance. Just like a guitar string vibrates at different frequencies when plucked, a structure will start vibrating if some load is applied at certain intervals. This phenomenon is called resonance, and the mathematic principle behind this has been known for ages. It is only in the last century that engineers started realising resonance can occur in tall slender structures as well. The mathematical problem used to solve these 'fundamental' frequencies (those at which resonance occur) is called the eigen-value problem. In 1846 Jacobi published a paper on computing eigen-values for small linear systems (Drmac and Veselic, 2005) in order to describe the orbits of the then known seven planets. In the 1950's Arnoldi, Francis, Givens, Householder, Kublanovskaya, Lanczos, Ostrowski, Rutishauser, Wilkinson, and many others further developed algorithms and analysis for more complex eigen-problems (O'Leary, 1995). Although these pioneers furthered the development of eigen-value analysis from a few differential equations to large systems, their work was only implemented in the engineering industry during the late 1970's with the development of desktop PC's. Until then simple hand calculations were used to estimate the vibration modes of structures. It was not necessary to use complex eigen-solvers during the early years of dynamic computations. Structures were modelled with simplified mathematical models, only incorporating the most important global degrees of freedom (form here on referred to as DOF's), limiting the number of differential equations to a manageable amount. Furthermore, it was widely accepted that only the first fundamental vibration mode was of importance to resonance. As a result simple algorithms were used in chimney design to estimate these vibration frequencies.

Kenneth R. Jackson (1978) proposed one such simplified formula in his book 'A guide to chimney design'. The first natural frequency can be calculated as follows:

$$N = \frac{3}{\pi H^2}\sqrt{\frac{2 \times E \times I}{5 \times m}} \tag{2-1}$$

where N is the frequency of the first vibration mode, H is the height, E is the modulus of elasticity, m is the mass per unit height and I the moment of inertia. This equation applies to concrete chimneys specifically; a different equation is proposed for steel chimneys.

Another commonly used eigen-frequency method is Rayleigh's principal. It equates the maximum potential energy at maximum deflection and zero velocity, and with the kinetic energy at maximum velocity and zero deflection. The mathematics is shown in Equation set 2-2. Let u(x) be the deflection along a cantilever beam subject to a transverse load proportional to weight, m(x) the mass per unit length and y the instantaneous deflection (Pinfold, 1975).

$$\tfrac{1}{2}mgy + \tfrac{1}{2}m\dot{y}^2 = E$$

substituting

$$y = u(x)\sin\omega t;\ \dot{y} = \omega u(x)\cos\omega t$$

$$with: \omega t = \tfrac{1}{2}\pi \Rightarrow energy = \tfrac{1}{2}mgy \Rightarrow E = \int_0^L \tfrac{1}{2}gm(x)u(x)dx$$

$$and: \omega t = \pi \Rightarrow E = \tfrac{1}{2}m\dot{y}^2 = \int_0^L \tfrac{1}{2}\omega^2 m(x)u(x)^2 dx$$

$$\therefore \int_0^L m(x)u(x)dx = \frac{\omega^2}{g}\int_0^L m(x)u(x)^2 dx$$

$$\therefore \begin{bmatrix} area\_of\_mass \times \\ deflection\_curve \end{bmatrix} = \frac{\omega^2}{g}\begin{bmatrix} area\_of\_mass \times \\ (deflection)^2 curve \end{bmatrix}$$

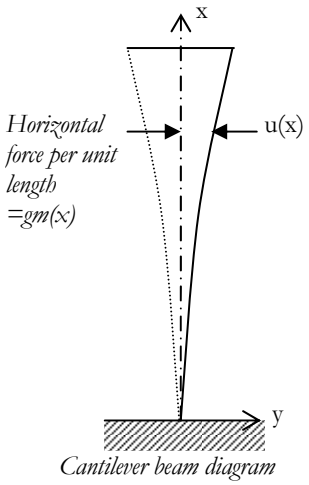

(2-2)

This would only yield an approximate answer because of the assumption that the deflection under dynamic loading would be the same as under gravity. However, the computed pulsation (ω) is not too sensitive to the shape (2nd order approximation). The frequency obtained will always be greater than the actual value. Furthermore, this method is also restricted to the first mode of vibration.

The Myklestad-Holzer method (Myklestad, 1944) was often used to compute higher modes. It is based on the stiffness matrix method commonly used today. The cantilever is divided into a

number of discrete masses interconnected with weightless beams. According to Myklestad, the number of masses should be twice the number of eigen-modes to be calculated.

Modern finite element software utilizes more modern matrix formulation based on the differential equation of motion. The system of equations is too large to solve with hand solutions methods. Based on subspace iterations as defined by Arnoldi, Lanczos etc., modern PC's can solve large systems of equations easily with simple programming routines. Although many advanced software packages are available for detailed dynamic structural analysis, a simplified lumped mass approach is often still used in tower and chimney designs. In the lumped mass approach, the stiffness between elements is modelled as springs with no mass. The mass of the member represented by the spring is then divided and placed at the end nodes of the spring. These simple methods are faster, well understood and researched, and are often accurate enough for simple geometries like those of chimneys and TV towers.

2. 3 Damping

When a guitar string is plucked, it keeps on vibrating for a while, but eventually dies out. The amplitude of the waves decreases with each surpassing cycle. This is due to an energy loss in the system to something else (sound, air friction etc) and the phenomenon is known as damping. As early as scientists realised that structures can resonate, they also discovered that other energy losses exists in the system (mostly a combination of aerodynamic damping and structural damping). These energy dissipaters were modelled as one energy term in the dynamic equation in order to simplify the complex damping phenomenon. The result of this is that damping could not be calculated accurately because there are so many unknown energy dissipation role players in this one mathematical term. The only way of knowing how large the 'energy extraction' of such dissipaters is, is to measure the decay of a structure's oscillating motion. Even today, the only knowledge available on damping values is measurements taken on completed structures where a test is conducted on the oscillation decay rate. This parameter is known as the 'logarithmic decrement' (logdec) and will be explained in further detail in chapter 4.

The logdec have been measured with tests on full-scale chimneys and towers of different dimensions. These tests serve as a database for future designers to consult in predicting a logdec for a new structure. But even the tests are subject to variation, depending on the method used. The principal is to apply a sudden force at the top of the structure and observe the decay in amplitude. This can be done by rockets, rotating eccentric masses or a point load induced by pulling the structure with a cable attached at the top and releasing at a certain load. (Pinfold, 1975).

2. 4 Wind loads

Together with seismic loads, wind is the dominant lateral loading a chimney or tower structure will face. Scenarios to be studied include a static wind load, a gusting dynamic wind load, a vortex shedding dynamic load and an ovalisation effect due to a distribution pressure around the shell. In towers and chimneys vortex shedding is often the most critical. This phenomenon may lead to resonance and failure, despite sufficient resistance to the other wind load scenarios.

Most TV towers and chimneys are well within the boundary layer of airflow. The boundary layer is the layer of air above the ground that is strongly influenced by the shape of the landscape. Depending on the topography, the boundary layer can be up to 1000m high. The equations of wind speeds with regards to height, however, are mostly accurate up to 300m (Dyrbye & Hansen, 1997). A commonly used formulation is the power law profile:

$$\frac{V_z}{V_{10}} = \left(\frac{z}{10}\right)^{\alpha} \tag{2-3}$$

where V_z is the wind speed at height z, V_{10} wind speed at 10m above ground level and α the ground terrain classification coefficient (0.16 for open country). The wind speeds (V) can be converted to an equivalent static pressure load (F) with a force coefficient (C_c) for the section shape area (A) and the air density (ρ).

$$P \propto V^2; \quad F = C_c A \frac{1}{2} \rho V^2 \tag{2-4}$$

Gust winds can cause resonance because of its periodic nature. Although gust behaviour is unpredictable, a history of gust winds can contain frequency components that match the structure's modal frequencies. Since gusting winds are unpredictable they are usually dealt with in a probabilistic approach. From statistical data reworked from measurements, hand calculation methods have been developed to simplify this complex phenomenon. A.G. Davenport (1967) proposed one such method known as the gust pressure factor approach. The mean wind pressure is multiplied by a factor G to give gust pressure load. G is defined as

$$G = 1 + g_p r \sqrt{B + \frac{S \cdot F}{\beta}} \tag{2-5}$$

where g_p is the peak factor, β the background gust energy, r the roughness factor, S the size reduction factor, F the gust energy ratio and β the structural damping factor. (Halabian *et al*, 2000). The procedure will be applied and described in more detail in chapter 4. The new pressure load is then applied as a statically distributed load on the structure.

Vortex shedding occurs as a result of vortices or eddies that form as air passes by the section profile. The air movement behind the section becomes turbulent when airflow passing the object creates alternating low-pressure vortexes on the section's downwind side (Wikipedia, 2005). This is caused by the vorticity in the moving air as a result of high shear strain rates in the airflow's boundary layer (see figure 2-2).

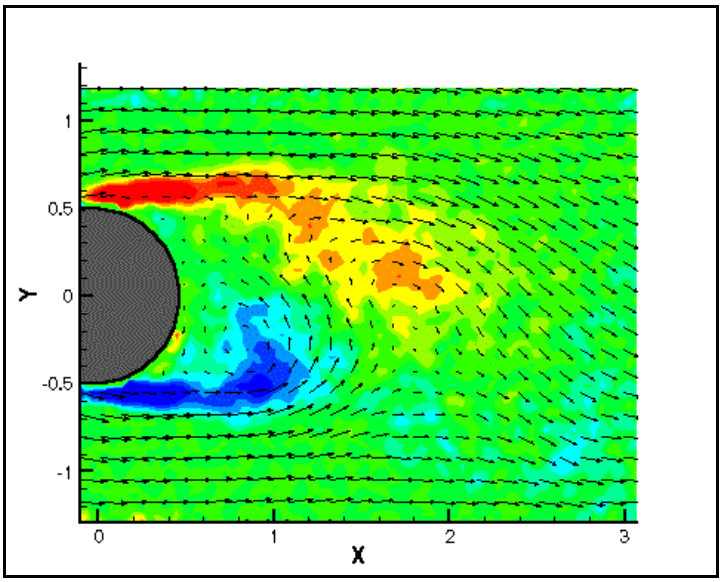

Figure 2-2: Vortex shedding behind a cylindrical section. (D. Cobden, 2003)

The vortex trail behind the cylinder may start alternating according to the size of the section and speed of the moving air. The Reynolds number (Re) characterises the airflow around a cylinder and thus is the characteristic ratio between inertia and viscous forces:

$$\mathrm{Re} = \frac{\rho \upsilon D}{\mu} \tag{2-6}$$

where ρ is the air density, v the air-flow velocity, D the cylindrical diameter and μ the dynamic fluid viscosity. The Reynolds number, in turn, determines the Strouhal number (S), which indicates the frequency of the above-mentioned alternating vortices.

$$N = \frac{S \cdot V}{D} \tag{2-7}$$

where N is the frequency in Hz, S is the Strouhal number, V is the approach speed of the moving air and D is the diameter of the section. If the Reynolds number falls between 200 and 200 000 the Strouhal number is 0.2 (Wikipedia, 2005). This is commonly used in chimney designs. Once the Strouhal number is determined, the critical airflow velocity for a certain frequency can be determined. If the critical airflow velocity of the first mode's natural frequency is outside the reach of the mean airflow, the structure is safe.

Ovalisation occurs in sections with large diameters and thin walls. This can be the effect of airflow around the section and the resulting cantilever bending moment which warps higher circular sections on the free end of the cantilever. At the leading edge of air flow the pressure is positive, but as the air moves around the section, suction occurs on the sides and at the back face. This can cause the section wall to warp or ovalise. Bending moments form along the circumference of the section in the wall. In reinforced concrete cracks will form and reduce the stiffness. This threatens limit states as defined in building codes. The maximum bending moment for a constant diameter tubular section with a constant parameter pressure load (in Newton-meters per meter height) are given by

$$M_o = 0.08qD^2 \tag{2-8}$$

where M_o is the moment due to ovalisation, q is a constant perimeter pressure in N/m^2 and D the diameter of the section. The wall thickness and reinforcement must be adapted to withstand the moment.

2. 5 Applicability to the solar chimney

If one could compare the solar chimney with a regular chimney by scaling it down, its wall thickness would be 0.3m thick at the base and 0.04m thick at the top if scaled down by the height to 200m and in the diameter to 20m. This is almost the equivalent of a steel chimney, but with a less elastic material. Complex cracking patterns can be expected with such unusual dimensions, and the structural behaviour would be different to that of either RCC or steel chimneys, not to mention TV towers. The hand calculation methods mentioned earlier would simplify the problem to an extent that the prediction/design becomes unreliable. Therefore it was decided to conduct a eigen-value analysis with finite element software.

Damping is still a poorly known parameter in dynamic analysis, and just like the pioneers of dynamic studies, approximate damping values will have to be assumed for the solar chimney until it can be measured on a full-scale structure. In chapter 4 we will continue the investigation into the phenomenon of damping by consulting other studies on the subject, to understand and hence predict it better.

The solar chimney exceeds the dimensions of the studied boundary layer. It would be naïve to assume the same conditions up to 1500m as in the first 300m of the atmosphere. Chapter 5 will have a look at what wind behaviour can be expected at these heights, and what local effects may occur around the section. At large deviations from the norm, the hand calculations developed for smaller chimneys and TV towers are not accurate any more. Transverse vortex oscillation may have a local effect on the solar chimney, but may not necessarily be a noteworthy global threat. Ovalisation might occur, but not only as a result of a static load.

The rest of this document will present detailed analytical methods to describe these behaviours accurately, and in more detail.

Chapter 3

THE FINITE ELEMENT MODEL

In order to analyze a structure dynamically, the simplest mathematical representation of the structure must be determined, but without compromising the validity of the model. Finite element models (hereafter referred to as FEM) simulate reality better when the mesh of the model is optimized by, for example, mesh refinement or increasing the degrees of freedom of the elements. There is also a point in mesh refinement where increase in accuracy become insignificant, and the amount of computing power becomes too much to be worth the effort and time.

If the mesh is very coarse one might save computing time, but the result deviates from reality to such an extent that it is not useful anymore. In quadrilateral shell elements (which was used in the solar chimney FEM model), a phenomenon may occur known as "locking". It is a result of excessive stiffness in one or more deformation modes due to quadrilateral shell elements having nonrectangular shapes; large aspect ratio's or subjected to large curvatures over the surface of the element. Locking does not imply complete rigidity, but it stiffens the structure globally, leading to results, which may not be considered as a realistic representation of the real structure. (Cook, Malkus, Plesha and Witt, 2002).

Thus, somewhere between these two extremes a model must be defined which is both realistic in representation but also affordable in terms of computing time, effort and power.

In this study the TNO Diana package was utilized to set up a finite element model and execute the mathematical analysis as described in this chapter. A Matlab™ script file was developed along with the execution of the Diana dynamic procedures in order to understand the fundamental principles behind the commercial package's analyses. The Matlab™ file implements the basic theory presented in this chapter. With the code, the user can execute a simplified form of a dynamic simulation and view it graphically. Further reference to the script file is made in Chapter 6.

3. 1 From Static to Dynamic

In a dynamic analysis the optimization of the problem described above is more critical, as the computing power required for a dynamic problem is larger than for a static analysis. The static equation to be solved is as follows:

$$\overline{\overline{K}} \cdot \bar{d} = \bar{R} \tag{3-1}$$

where $\overline{\overline{K}}$ represents the two dimensional stiffness matrix, *d* represents the vector of displacements at each node and $\bar{\bar{R}}$ represents the load vector. This represents a set of linear equations as many as the number of unknowns, being the degrees of freedom of the system, and the dimensions of $\overline{\overline{K}}$ (the stiffness matrix). If one considers the Dynamic differential equation, it becomes more complex:

$$\overline{\overline{M}} \cdot \bar{\ddot{x}}(t) + \overline{\overline{C}} \cdot \bar{\dot{x}}(t) + \overline{\overline{K}} \cdot \bar{x}(t) = \bar{F}(t) \tag{3-2}$$

where *t* represents time, $\overline{\overline{M}}$ represents the mass matrix (associated mass of the degrees of freedom), $\overline{\overline{C}}$ represents the damping matrix and *F* the load vector as a function of time. The equation (3-2) may be rewritten as a set of differential equations with as many unknowns as there are degrees of freedom, for one moment in time (*t*). Even when compared to the calculation of one value of t with the static equation, it is obvious that the computing power needed here is already much more. If the time variable is taken into account, the computing time must multiplied by the increase in the number of time steps in the dynamic analysis, which can be a few thousand even if a few minutes is being considered, depending on the length of a time step.

It is clear that it is essential not to waste computing time by making the FEM model too complex, therefore the optimization of the FEM model is a critical exercise before attempting a dynamic analysis.

3. 2 Meshing the static model

In order to find a suitable model, a sensitivity analysis with a basic wind pressure profile (as defined by van Dyk, 2004), needs to be conducted to see how the mesh refinement, positioning of steel reinforcement, wall thickness and type of ring stiffeners will influence the results. The ring stiffeners are composed of tension trusses configured like the spokes of a bicycle wheel, positioned horizontally, to keep the cylinder from folding into it self. These stiffeners are positioned inside the tower at various heights. Figure 3-1 shows the stiffener and reinforcement configuration.

To have a base point, the model was set up with the least possible number of elements, which allow the different physical features in the model to be simulated.

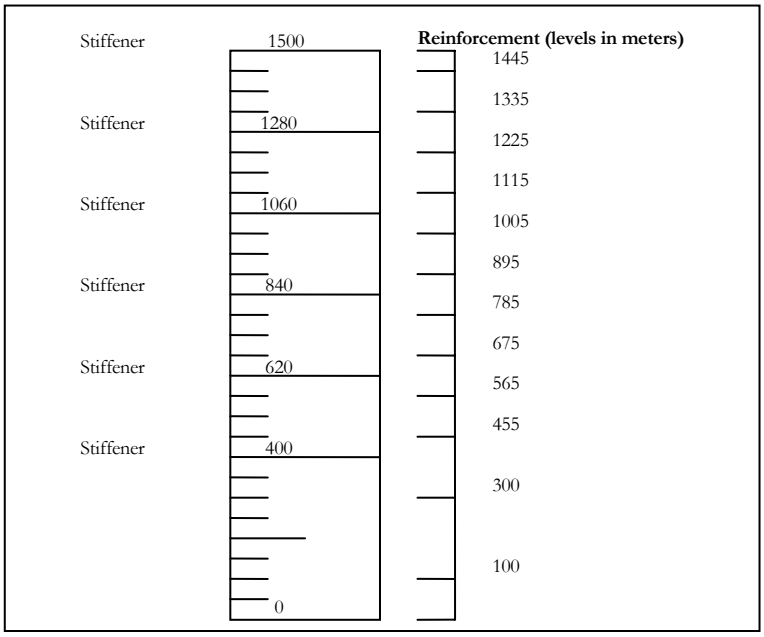

Figure 3-1: The stiffener and reinforcement layout of the solar chimney.

3. 2. 1 The Basic Model

It is important that the meshing of the structure does not influence the physical properties. In other words, there must be enough elements to take into account the changing reinforcement layers, the positions of the ring stiffeners, the wall thickness and the tensioned spoke-like members of the ring stiffeners. Although the dimensions of the chimney is briefly mentioned in chapter one, for explanatory purposes the dimensions will be looked at in detail in this section. The levels of the ring stiffeners and the detailing configuration of the wall reinforcement are the first constraints with regard to meshing. Because of their positions the number of rows of elements (in the height or z-direction) is limited to 28 (Figure 3-1). The ring stiffeners and the different reinforcement layers occur at different levels, dividing the structure into the least number of rows.

This implies that one element is between 50 and 55 meters high. A good aspect ratio to assume is no more than 1:2. The model is simulated with a half cylinder with a radius of 81.1 meters. This is valid because of the symmetry of the chimney in all directions and the simplification that the wind pressure profile is regarded symmetric around the perimeter of the tower, thus torsional modes will not be activated. When the chimney is modelled as a full cylinder, two eigen-modes will result for each eigen-frequency, the modes being 90 degrees in relation to each other with regard to direction. The perimeter of the half-cylinder therefore is radius times π, equal to 254.8 meters. To get the desired aspect ratio, 9 elements can be packed in a row along the parameter. This gives a total of 252 elements, which is the coarsest mesh with which all the geometrical features can be incorporated.

3. 2. 2 Mesh refinements

The solar chimney model is meshed with CQ40S quadrilateral isoparametric curved shells. Each element has eight nodes and each node in turn has five degrees of freedom, three translational and two rotational. The in plane torsion degree of freedom is ignored. Such nodes are known as 'drifting' nodes. Figure 3-2 shows the shell configuration

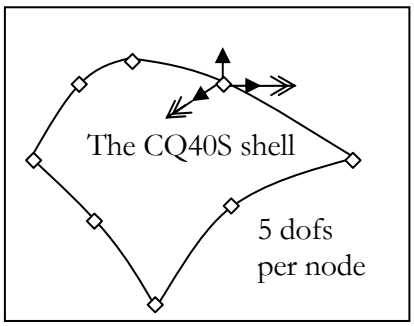

Figure 3-2: Diagrammatic representation of the CQ40S shell element.

In order to get an idea of the effect of different meshes the computed behaviour of the structure will be compared when finer meshed.

The next step is to double the number of elements by packing 18 elements along the parameter and keep the elements in the height direction the same. This results in 504 elements. The effect of this is that the aspect ratio of the elements has now been increased to 1:4. This is still an acceptable aspect ratio for the type of element used (Figure 3-2).

The number of rows in the height direction can be doubled to give 1008 elements. The aspect ratio is 1:2 again. From this point forward the process of first doubling the parameter and then the height will be repeated until the optimum mesh quantity is reached.

3. 3 Convergence

The displacement at the top of the structure (measured at the symmetry axis), under the same loading conditions for a certain mesh density were compared with one another (figure 3-3). The various meshed models were also tested with and without reinforcement layers in the CQ40S elements, to see what the effect would be in the sensitivity study.

Up to 1008 elements the displacements increased, each time a little less. This clearly shows the effect of locking and that the minimum model was too coarse to produce an accurate answer. But at 4032 elements the displacement was dropping slightly. From these results it can be deduced that convergence is reached somewhere between 1008 and 4032. But in order to avoid an aspect ratio of

1:4, and to meet the criteria of having as few elements as possible, the 1008 element model was chosen as the optimally meshed model.

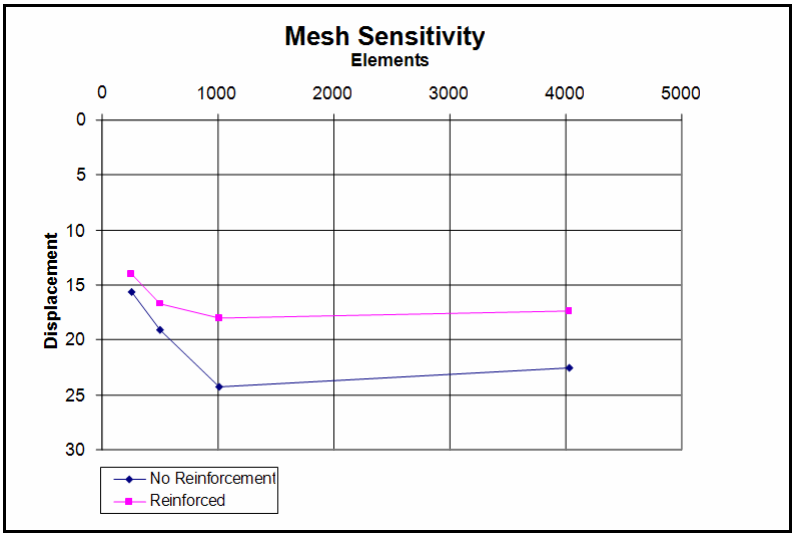

Figure 3-3: Displacement convergence with mesh refinement

Table 3-1 presents the displacement values of the different meshed models for reinforced and non-reinforced criteria.

Elements	**Maximum Displacement (m) at the top of the tower**	
	With reinforcement	*Without reinforcement*
252	14m	15.7m
504	16.7m	19.1m
1008	18.0m	24.3m
4032	17.4m	22.5m

Table 3-1: Horizontal displacements with increase in element mesh.

3. 4 Modes of Vibration

The applied forces causing oscillation do not need to be very large; it is the force's period that makes them dangerous to the structure. It simply implies that if the structure's natural vibration frequencies coincide with that of a small load, resonance will occur. The amplitude at resonance is indirectly related to the difference of the dynamic load's frequency and the structures eigen-frequency, as well as the energy dissipation ability of the structure. In most high-rise buildings 10% of critical damping is assumed to operate.

The structural integrity of the solar chimney in the light of dynamic behaviour mainly depends on two variables: the frequency components of the load, in this case wind, and the eigen- or natural frequencies of the structure itself. In this chapter the eigen-frequencies will be described briefly and the eigen-modes will be shown by means of graphs.

3. 5 The Eigen Problem

The eigen-modes and frequencies of a structure go together in pairs. For each eigen-frequency, there is a unique eigen-mode, or eigen-vector. The eigen-frequencies are frequencies at which the system will resonate if a load or loads are imposed on it at these specific frequencies. Another way to look at it is to say eigen-frequencies are the frequencies at which the system would oscillate naturally if it were given initial displacements in the shape of the associated mode shapes. Mathematically the eigen-value problem looks as follows:

$$\overline{\overline{K}} \cdot \overline{Y} = \omega \ \overline{K} \tag{3-3}$$

where Y represents the eigen-vector, K as previously defined and ω represents the eigen-value, or in the dynamic analysis case, the eigen pulsating frequency. Except for $Y = 0$, there are other pairs of the vectors Y and scalar values ω that satisfy Equation 3-3. Because this is a state where there can be movement of the structure without any loading, the dynamic equation can be set equal to zero. Strictly speaking, in theory, this is only possible if there was an initial force or displacement applied somewhere in the past, and if the system has no damping. So with the damping not taken into account, (3-2) becomes

$$\overline{\overline{K}} \cdot \overline{d} + \overline{\overline{M}} \cdot \ddot{\overline{d}} = \overline{0} \tag{3-4}$$

where $\ddot{\overline{d}}$ represents degree of freedom acceleration vector, K, M and d as previously defined. If $\overline{d}(t) = \tilde{\overline{d}} e^{i\omega t}$ and substituted in equation (3-4), and $e^{j\omega t}$ is taken out as a common factor, the equation can be rewritten as:

$$\left(\overline{\overline{K}} - \omega^2 \overline{\overline{M}}\right) \cdot \tilde{\overline{d}} = \overline{0} \tag{3-5}$$

The bracket term must be non invertible for d to have other values than 0, therefore the determinant of the bracket term is zero. This means that it is possible to solve for ω^2, which gives us the pulsation frequencies of the eigen solutions, and by back substitution it is possible to solve the corresponding vector d, and all multiples of it. The vector d is the mode shape of the specific eigen-solution.

3. 6 The Chimney model

In the case of a two degree of freedom system the solution is easy, and the two eigen-frequencies that exist for the system can be solved by hand. The solar chimney model has 1008 nodes each with 5 degrees of freedom. Hence the solution becomes more complex with the number of eigen-modes being around 5000. However, since the higher modes will correspond to high frequencies, we are not interested in all the eigen-modes, only those that fall in the danger zone of the pulsating load. The first ten eigen-frequencies, ignoring torsional eigen-modes, have been found to be as follows:

Eigen mode	1	2	3	4	5	6	7	8	9	10
Frequency (Hz)	0.101	0.177	0.286	0.324	0.331	0.424	0.432	0.438	0.453	0.465

Table 3-2: Frequencies of the various vibration modes.

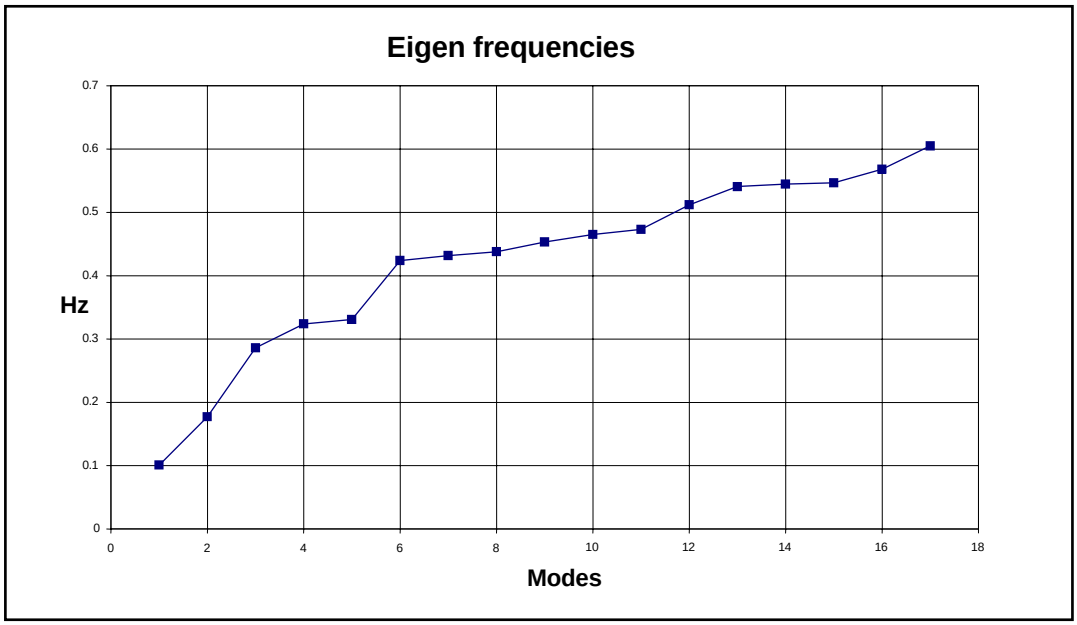

Figure 3-4: Eigen frequency curve for modal increase

The mode shapes turned out to be more complex than that of a normal cantilever column. Due to the thin wall of the structure in relation to its size, some of the mode shapes involve ovalisation of the parameter. It is interesting to note the irregularities in the increases of frequency shown by figure 3-4. This is not regarded as a problem or a significant phenomenon in the global behaviour of the chimney. Figure 3-5 show the first six symmetric mode shapes.

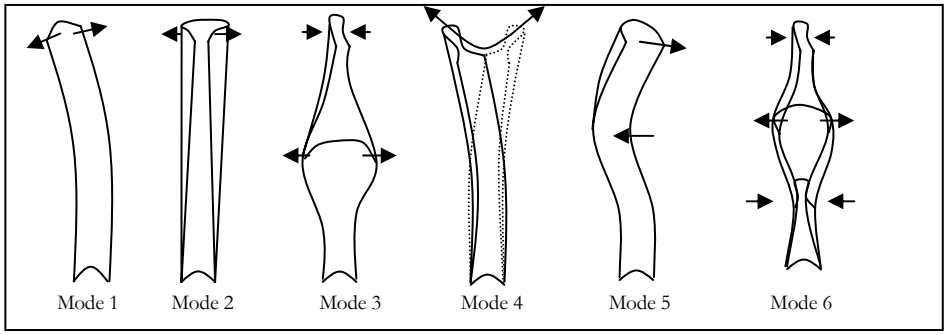

Figure 3-5: The first five eigen-modes

Take note that mode 1 and mode 5 are referred to as global mode shapes, since the whole structure participates as if it were a cantilever beam. Figure 3-5 only show the first six eigen-modes since the shapes thereafter are too complex to illustrate in such a simple way.

3. 7 The reduction of equations

The computing power and time needed to solve a 6000-degree of freedom (dof) system for 10 minutes of wind data is large. Fortunately, mathematicians, and the phenomenon of eigen-modes, provide a shortcut to approximate the answer very close reality. The principle is based on the fact that the response of the structure, for a given pulsating load, can be calculated as the weighted sum of all the eigen-modes. The specific load pulsation activates a part of every eigen-mode, and when all these partial responses are added together, the result is the global response. The higher modes may have little effect on the responding amplitudes of global modes; however, they may cause significant local stresses in local modes. If the frequency of the load is in the range of the first five global eigen-frequencies, say, up to the first ten global eigen-modes would be enough to take into account to get a realistic response, since there will be no load frequency component to activate the corresponding higher eigen-modes. For the solar chimney, the first 400 modes were taken, of which 10 shows global behaviour. The 400^{th} eigen-modes occurs at 3.93Hz, which is also beyond the significant influence of the gust spectrum (up to about 2 Hz). The following is a very brief mathematical description of how this procedure works.

It is important to take note of the orthogonal properties of the eigen-modes with respect to the stiffness and mass matrices. This means that

$$with \quad k \neq j \begin{cases} \bar{\phi}_k{}^T \cdot \overline{\overline{M}} \cdot \bar{\phi}_j = 0 \\ \bar{\phi}_k{}^T \cdot \overline{\overline{K}} \cdot \bar{\phi}_j = 0 \end{cases} \tag{3-6}$$

where $\bar{\phi}_k$ and $\bar{\phi}_j$ are any two of the eigen-mode vectors of the system containing $\bar{\bar{M}}$ and $\bar{\bar{K}}$. Thus the above set of equations is only non-zero when k=j.

If *y(t)* is the response of one mode where *y(t)* represent a single degree of freedom (the modal degree of freedom so to speak), then the global response *d* can be written as

$$\bar{d}(t) = \sum_j \bar{\phi}_j y_j(t) \rightarrow \bar{d}(t) = \bar{\bar{\phi}} \cdot \bar{y}(t) \tag{3-7}$$

where $\bar{\bar{\phi}}$ is a matrix with columns of mode vectors. By replacing (3-7) into (3-2) and pre multiplying with $\bar{\bar{\phi}}^T$ yields

$$\begin{aligned}
&\bar{\bar{\phi}}^T \cdot \left[\bar{\bar{K}} \cdot \bar{\bar{\phi}} \cdot \bar{y}(t) + \bar{\bar{C}} \cdot \bar{\bar{\phi}} \cdot \dot{\bar{y}}(t) + \bar{\bar{M}} \cdot \bar{\bar{\phi}} \cdot \ddot{\bar{y}}(t)\right] = \bar{\bar{\phi}}^T \cdot \bar{F}(t) \\
&\textit{rewritten:} \\
&\bar{\bar{K}}^* \cdot \bar{y}(t) + \bar{\bar{C}}^* \cdot \dot{\bar{y}}(t) + \bar{\bar{M}}^* \cdot \ddot{\bar{y}}(t) = \bar{F}^*(t) \\
&\textit{with} \\
&\bar{\bar{K}}^* = \bar{\bar{\phi}}^T \cdot \bar{\bar{K}} \cdot \bar{\bar{\phi}} \\
&\bar{\bar{C}}^* = \bar{\bar{\phi}}^T \cdot \bar{\bar{C}} \cdot \bar{\bar{\phi}} \\
&\bar{\bar{M}}^* = \bar{\bar{\phi}}^T \cdot \bar{\bar{M}} \cdot \bar{\bar{\phi}} \\
&\bar{F}^* = \bar{\bar{\phi}}^T \cdot \bar{F}
\end{aligned} \tag{3-8}$$

If it can be shown that the damping matrix is orthogonal with respect to the mode vectors, then it implies that all the terms of the * matrices lies on the diagonals. This means that it is possible to solve an *n* number of independent differential equations (where *n* is the number of chosen modal degrees of freedom). The equations can be decoupled to the following equation:

$$K^*_{jj} y_j + C^*_{jj} \dot{y}_j + M^*_{jj} \ddot{y}_j = F^*_j \tag{3-9}$$

This shows that each mode has a modal stiffness, damping, mass and portion of the external load to which it responds. Of course, each decoupled mode will behave differently towards the same pulsating load.

3. 8 Proportional damping

Damping is the absorption of energy, based on a structure's material and geometric properties. In order for things to move, to flex, to crack etc. energy is needed. This requires energy to be taken out of the global motion energy of the structure. Hence the energy equilibrium with stiffness energy, momentum energy and damped or dissipated energy is taken from the initial energy put into the system.

Damping will be explained in more detail in chapter 4. It is important to take note of how the damping matrix is set up to enable the decoupling of the degrees of freedom. If the orthogonal mass and stiffness matrices are multiplied by coefficients α and β, the damping matrix will also be orthogonal.

$$\overline{\overline{C}} = \alpha \overline{\overline{K}} + \beta \overline{\overline{M}} \tag{3-10}$$

In chapter 4 the effects of the α and β factors will be discussed in more detail. For now it is only necessary to understand that in order to obtain a frequency-response profile, some form of damping is necessary, otherwise the structure will resonate into infinity when the frequency of the force corresponds to the eigen-frequencies.

3. 9 The solar chimney resonance profile

In the case of the solar chimney the first 400 modal degrees of freedom (1st mode at 0.1 Hz, 400th mode at 3.93 Hz) were used to test the resonance response. A line load was applied over the height at one of the edges of the half cylinder and given varying frequencies from 0 to 0.4 Hz in increments of 0.01Hz. A damping coefficient of 0.1% of critical damping was assumed to keep the resonance from becoming infinite at the eigen-modes.

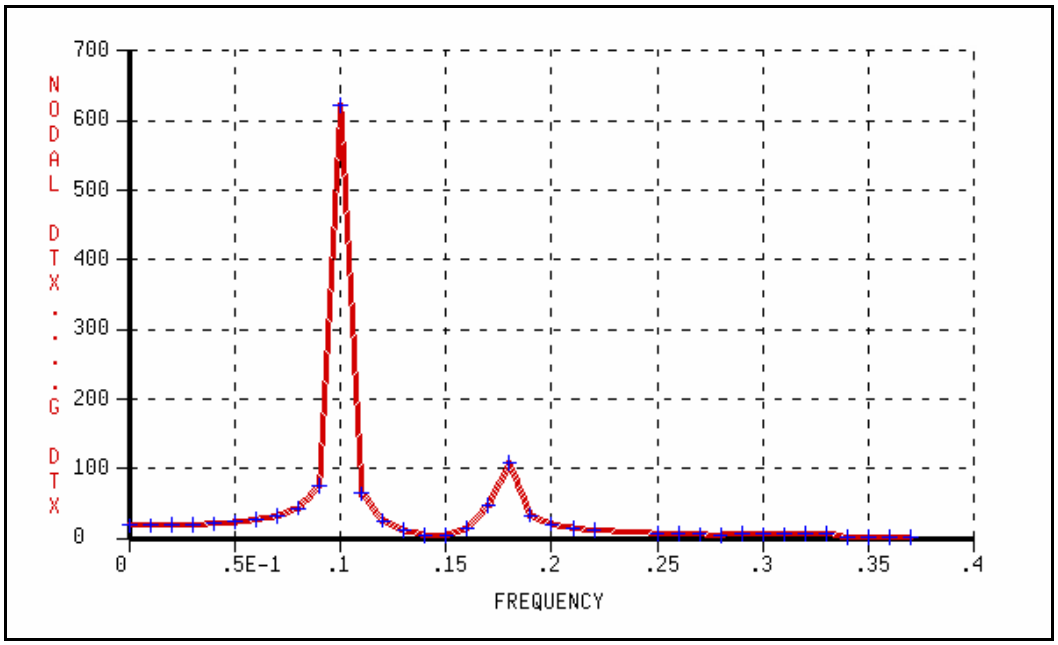

Figure 3-6: The resonance profile of an oscillating line load, constant over a frequency range

The first mode showed the most severe amplitude peak (Figure 3-6), where the second mode shows a substantial decrease. From the third mode onward the displacement amplitude becomes small in comparison to the first two responses. It is clear that the danger area of wind frequency will be the most critical at low frequencies.

3. 10 Closing remarks

This chapter provides background information on the theory of dynamics in the light of conceptualizing the dynamic finite element model. It is important to understand the definitions and limitations of the theory before attempting to define values of the parameters on which these formulations are based.

The next two chapters will investigate the parameters still unknown or unclear in order to complete the dynamic analysis, namely damping and dynamic loading. Chapter six outlines the results obtained from the dynamic analysis based on the theory as presented in this chapter.

C h a p t e r 4

ESTIMATING DAMPING CHARACTERISTICS

4. 1 General Remarks

As mentioned in chapter 2, the estimation of damping in an untested structural geometry is a difficult matter. Although a variety of literature is available on the subject of damping, it remains a poorly known aspect of general vibration analysis. Woodhouse (1998) proposed that the reason for this is that a fundamental, universal mathematical model of damping forces does not exist, and needs to be characterized experimentally.

As a result of the solar chimney's unconventional scale with regard to size, and the absence of a universal mathematical model to predict it, it may be dangerous to assign one damping configuration, and difficult to confirm it as exact. Instead, this chapter will consider different proposed methods and explain what their motivations are based on. From these approaches, a range of possible damping characteristics will be identified, and the dynamic model will be tested for its sensitivity toward these estimations.

Various methods of modelling damping and their mechanisms have been proposed in the literature. To understand which characteristics of the structure causes damping, this chapter will briefly discuss the different types of damping. Aerodynamic damping will be regarded as negligible for reasons later mentioned. It will be explained how types of material damping form the basis of what is commonly assumed for damping in concrete structures. To confirm the assumed type of damping, the methods of measuring damping in existing structures will be studied and a more detailed report will follow on measured values than presented in chapter 2.

Raleigh damping is an important mathematical method used to define the linear damping matrix in the second order differential equation of dynamic response. Methods for defining the Raleigh coefficients will be suggested and its relation to participating mass explained.

In addition to the traditional methods of modelling and characterizing damping, two alternative-suggested methods of predicting untested structures are briefly discussed. The applications of these methods fall beyond the scope of this thesis, but are included and recommended for future consideration.

The chapter ends with a discussion on the applicability of the different discussions on damping with regards to the solar chimney. A scope of damping values will be proposed based on existing measurements and methods of estimating damping with equations for untested cylinders.

4. 2 Types of damping

The amplitude of free vibration decays over time as a result of energy dissipation. This decay is generally termed the damping effect. The rate of decay can vary over time for different types of energy dissipation. Studying the pattern of amplitude decay of a free vibrating system can identify four such types.

4. 2. 1 Viscous Damping

Viscous damping dissipates energy proportional to velocity. Rayleigh (1894) first proposed the formulation for this kind of damping. The energy being dissipated per cycle is proportional to the frequency and the square of the amplitude (Cook *et al*, 2002). The damping is usually supplied by a drag force due to surrounding gas (aerodynamic damping) or liquid or by viscous dampers that could be added to the structure. One characteristic feature of viscous damping is the result of an exponential decay rate of a free-vibration response.

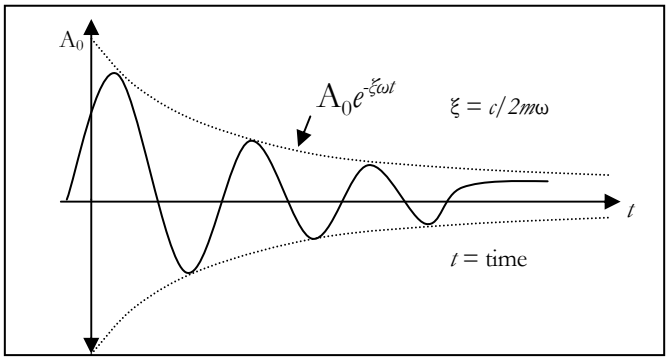

Figure 4-1: Logarithmic decay rate of free-vibration under viscous damping (Salzman, 2003)

Figure 4-1 shows the logarithmic decay diagram and equation, where A_0 is the starting maximum oscillation amplitude when the phase angle is one, ξ is a percentage of critical damping and ω is the pulsation frequency ($f2\pi$).

4. 2. 2 Coulomb damping

Also known as dry friction damping, it is the result of friction forces between dry surfaces, and may be categorized as material damping. The damping force is exerted as a result of friction due to a mass sliding over a dry surface (figure 4-2a). Thus the decay rate stays constant irrespective of the frequency, amplitude or velocity (figure 4-2b).

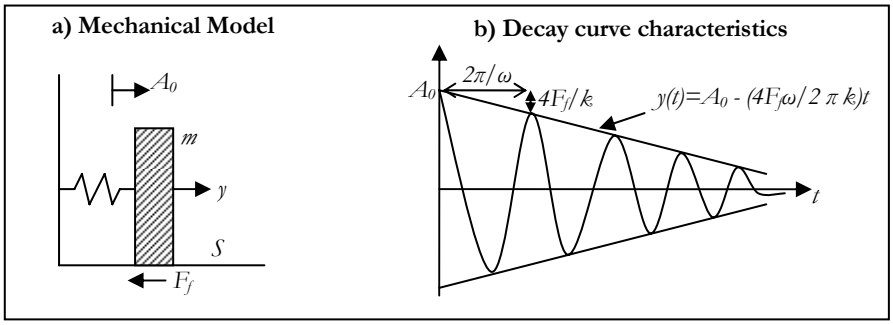

Figure 4-2: Linear decay of free vibration under coulomb damping (Salzman, 2003)

4. 2. 3 Hysteretic damping

Otherwise known as solid damping, it is the energy dissipation (transformed into heat) due to internal material friction during motion, and may also be classified under material damping. This happens as material matrix planes slip relative to one another. Such slip or dislocation is generally associated with plastic behaviour, which occurs at high stress levels. However, it may also occur on a small scale with nominal stresses in the elastic range. The energy dissipation per cycle is considered to be independent of frequency. However, it is approximately proportional to the amplitude of the deformed elastic body. The rate of reduction of the oscillation amplitude depends on the size of the area within the hysteresis loop.

Thus, the behaviour can be summarised as follows: The rate of decay, squared, is proportional to energy dissipation; energy dissipation is proportional to the hysteresis area; the hysteresis area is proportional to the deformation amplitude. As the amplitude increases, the hysteresis area enlarges as well, and dissipates more energy, implying higher damping. These loops are unique to the matrix structure of the structural material, and operate mostly in plastic deformable materials or composites.

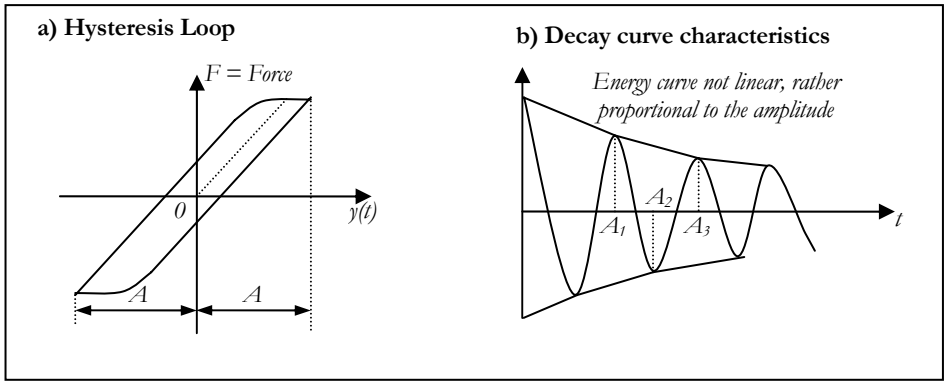

Figure 4-3: a) Force-Displacement Hysteresis Loop, b) decay of free vibration under hysteretic damping (Salzman, 2003)

4. 2. 4 Equivalent Viscous Damping

The original theory to describe internal damping was based on hysteretic damping and was proposed by Kelvin (1865). It was later discovered that the theory was not applicable to all solids, which contributes to the difficulty of developing a universal theory to describe solid damping for general applications (James *et al.*, 1964). Even though structures generally show a combination of linear and non-linear damping elements, it is the dependence on material type, material history, environment and test conditions that complicates the development of a general theory (Salzman, 2003).

Viscous damping is easy to employ in vibration analysis due to its simple mathematical formulation and velocity dependence. Even though analysts know viscous damping is not operating, but rather a combination of coulomb and hysteresis damping, it is easier to implement an 'equivalent' viscous damping (Tedesco *et al.*, 1999). Thus the linear equations of viscous damping are adopted or calibrated for a dynamic analysis. With the 'equivalent viscous damping' concept it is possible to evaluate internal damping of any kind of any member. Structural damping is then defined as the equivalent viscous damping ratio, ζ (Sun and Lu, 1995), which also indicates a percentage of critical damping. In this report the symbol ζ implies a percentage of critical damping where referred to equivalent viscous damping in structures, and ξ refers to the percentage of critical damping where referred to actual viscous damping, or when referred to the mathematical definition of viscous damping.

4. 3 Measuring damping

Three sources/mechanisms of physical damping have been mentioned, but usually it is simply modelled as equivalent viscous damping. To characterize this model (viscous damping), the parameter ζ must be determined experimentally, so some testing is inevitable. The same goes for stiffness (measure E and Poisson experimentally) and mass (density). The difference is perhaps that damping must be tested on a larger specimen (the structure itself) to capture all the effects, as opposed to small scale testing of elasticity and mass. The measured shape of the decay curve should then shed some light on the mechanisms of damping. However, as stated previously, no generalized equations exist for accurately capturing the various underlying energy-loss mechanisms. Consequently, in most structural systems damping has to be evaluated directly from experimental tests on large-scale specimens. Different techniques exist to determine the damping in a structure. They can be classified into two categories: free-vibration damping and forced excitation damping. The last mentioned technique is difficult to apply to large structures and is mostly used to conduct

small member or laboratory tests. Such tests can be used to characterise the damping in individual members, but cannot yet accurately relate to the global energy dissipation (damping). Therefore it will not be discussed further here. From these measurements parameters (such as ζ), can be determined.

Free vibration damping is measured by its logarithmic decrement (logdec) or logarithmic rate of decay. It is probably the most frequently used experimental damping technique (Clough and Penzien, 1975). Helmholtz (1877) first proposed the idea of free vibration decay of a viscously damped system, however, Rayleigh (1945) coined the term 'logarithmic decrement'. The traditional logdec technique (TLT) measures two amplitudes, A_1 and A_2, *n* cycles apart and gives the logdec value (δ) in the following equation

$$\delta = \frac{1}{n}\ln\left(\frac{A_1}{A_2}\right) \approx 2\pi\xi \Rightarrow n = 1 \tag{4-1}$$

which is related to ξ (damping ratio of critical damping) as shown above for small damping if n = 1. This assumes that viscous damping occurs, as depicted in figure 4-1. Critical damping is the least amount of damping energy needed to keep the system from oscillating. It can be shown in the following equation:

$$\xi = \frac{c}{c_{cr}} \Rightarrow c_{cr} = 2\sqrt{km} = \frac{2k}{\omega} \tag{4-2}$$

where c_{cr} is the critical damping, k the stiffness and m the mass.

The damped free-vibration system of figure 4-1 can be expressed as:

$$y(t) = Ae^{-\xi\omega t}\sin(\omega t + \phi) \tag{4-3}$$

where $Ae^{-\xi\omega t}$ is the exponentially decaying amplitude with a phase angle (φ) and pulsation frequency ω. As can be seen from this equation, the damping ratio is the parameter needed to characterize the damping matrix. The damping ratio is the ratio between the true damping and the critical damping value.

As mentioned in chapter 2, several databases with measured logdecs exist for different structures. Sky-scraper-like structures usually dissipate more energy in damping than tower-like structures due to a more complex member assembly. The averaged measured values for normal high-rise buildings will therefore not be applicable to the solar chimney. Tilly (1986) reports the following values for

high-rise chimneys and TV towers. The height of the structures is in the range of 200m and the logdecs vary from 0.03 to 0.06 approximately.

Measured Tower and Chimneys	Height (m)	Fundamental Freq. (Hz)	Damping (logdec)
Eggborough Chimney	198	0.38	0.03
Drax Chimney	259	0.25	0.05
Pembroke Chimney	213	0.43	0.04
Kingsnorth Chimney	198	0.38	0.03
Didcot Chimney	198	0.32	0.04
Fawley Chimney	198	0.46	0.03
London PO Tower	177	0.15	0.08
Martigues Chimney	210	0.35	0.03
Ambes Chimney	210	0.38	0.04
Ferrybridge Power station	126	-	0.06
Rugely Power station	137	-	0.06
York University Chimney	61	-	0.075
TV Tower Stuttgart	153	-	0.04
Munich TV Tower	290	0.18	-
Karlsruhe Chimney	180	0.26	-

Table 4-1: Height, fundamental frequency and logdec values for several chimneys and TV towers (Tilly, 1986; Pinfold 1975, Jeary 1974)

Pinfold (1986) presents another table with more natural modes and corresponding logdecs than the fundamental frequency for five of the above shown chimneys. With reference to this data, Pinfold states that the measured values of damping are independent of the natural frequencies and soil conditions. The scatter plot presented in figure 4-4 suggests, however, that a rough correlation may exist between the fundamental frequency and the damping logdec. The heights of the cases are plotted next to the dots, showing that the height is not correlated to the frequency or logdec. The linear tendency of the values shows a logdec of between 0.08 and 0.12 at 0.1 Hz, implying more or less 1.5% of critical damping.

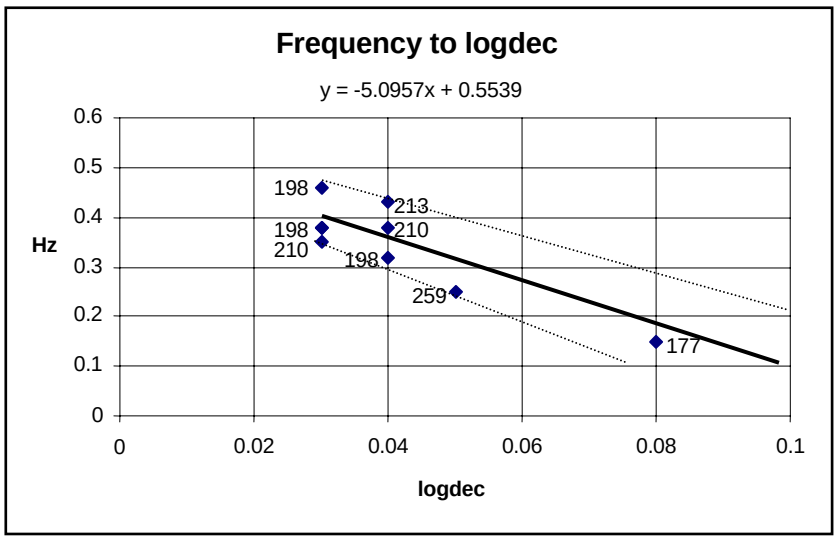

Figure 4-4: Linear estimation of the logdec at 0.1Hz based on values from Table 4-1

Jeary (1986) proposed a form of damping curve for general structures based on the proposals of Wyatt (1977), which proposed that the mechanisms of damping are friction, rather than the hysteric model previously assumed. This damping characteristic is depicted in figure 4-5.

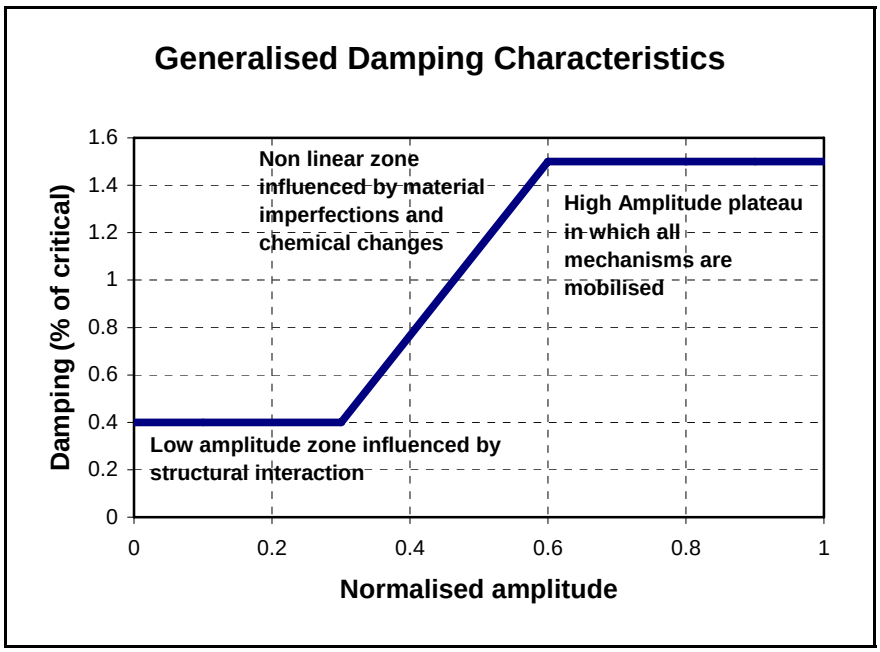

Figure 4-5: General damping prediction curve for tall concrete structures (A. Jeary, 1986)

4. 4 Rayleigh damping

Rayleigh's principle proposes to define damping as an energy loss due to a combination of a mass's movement through a medium and bending of a member or structural component. When a mass moves through a medium (like water or air), energy is lost because of drag. Little energy is lost at low frequency modes because of small drag that result from slow movement. At high frequency modes, more energy is lost because of higher oscillating velocities, resulting in higher strain and thus greater drag forces. Energy is transformed to heat when a piece of material bends in rapid succession as a result of internal material friction. Faster repetitive bending results in higher energy loss. Thus, mass proportional damping damps out lower modes, whereas stiffness proportional damping damps out higher modes.

Also known as proportional damping, this technique ensures an orthogonal damping matrix. In chapter 3 it was shown how this property enables the decoupling of the MDOF dynamic equation (3-1) to a set of linear SDOF dynamic equations by pre and post multiplying with the eigen-vectors. These methods also enable a reduction of variables as the decoupled equations for the higher modes may be ignored (also explained in chapter 3). The equation for Rayleigh damping is given in chapter 3 (3-10).

Choosing values for α and β can be difficult for structures with many degrees of freedom. The choice of α and β determines the damping proportion of the uncoupled system's critical damping value. Hence mathematicians have developed calibration methods to compute α and β. One method, described by Chowdhury and Dasgupta (2003) is to calibrate the proportions by means of interpolating the modal damping ratio for each uncoupled equation based on mass participation. The reasoning is as follows:

As the eigen-modes increase in frequency, their participating mass decreases. This is illustrated for the solar chimney in figure 4-5. The last mode's mass participation is small, and therefore has a low critical damping value. Since the damping ratio of each uncoupled system is a proportion of that system's critical damping, and since the damping of the system should be the same over all modes, the damping ratio (proportion) should increase with increasing modes to keep the damping capacity constant.

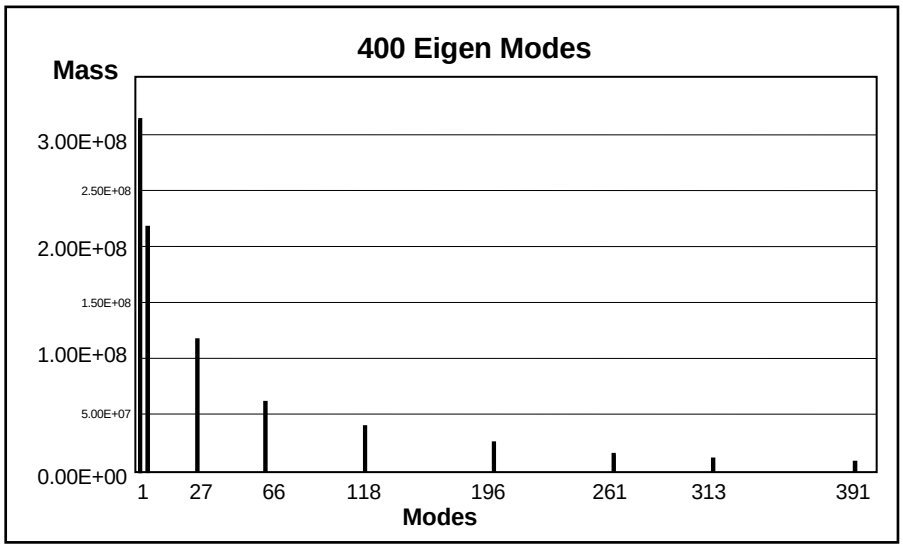

Figure 4-6: Mass participation of the solar chimney's global modes

This shows that, if higher mode damping contribution is significant, the results from a consistent damping ratio for all the modes will not give a realistic answer (Chowdhury, Dasgupta, 2003). The use of Rayleigh's principal can account for this discrepancy. One method of calibrating this change is by linear interpolation over the modes that contribute significantly to the participating mass. The mass participations of the modes are added until 95% of the total mass participates. The mode at which this happens is then noted as the m^{th} mode. To understand the reasoning behind this linear interpolation, it is important to understand what the α and β parameters represent. The following mathematical sequence demonstrates the Rayleigh-curve:

$$c = \alpha m + \beta k \quad ; \quad \frac{k}{m} = \omega^2 ; \quad \zeta = \frac{c}{2m\omega}$$
$$\zeta_i = \frac{\alpha m}{2m\omega} + \frac{\beta k}{2m\omega} \Rightarrow \quad \zeta_i = \frac{\alpha}{2\omega_i} + \frac{\beta\omega_i}{2} \tag{4-4}$$

where *m* refers to mass and *k* to stiffness. When the damping ratio ζ is plotted against pulsation frequency ω the first part of the graph is non linear, decreasing. As the alpha term tends toward zero (as ω increases), the beta term takes over and the curve tends to a linear increase. Flexible structures like antennas, long piles or tall chimneys exhibit this kind of behaviour. However, most civil engineering structures are reasonably rigid and the β term will dominate. Therefore the assumption can be made that the damping ratio for each mode is linearly proportional to the frequency of the system, also known as strain related damping (Chowdhury, Dasgupta, 2003).

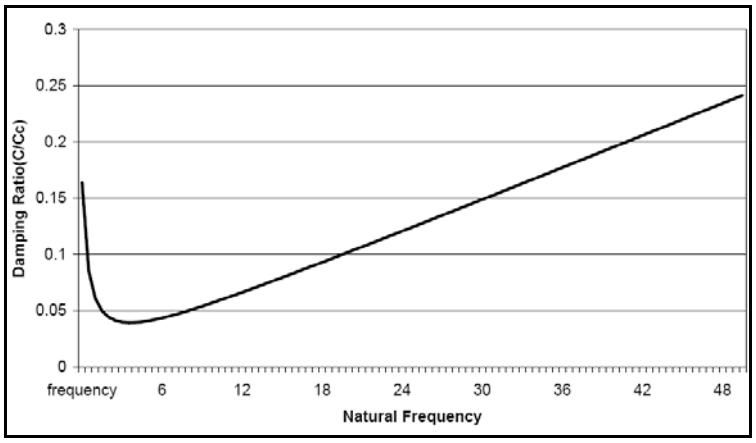

Figure 4-7: The proportional damping curve (Chowdhury, Dasgupta, 2003)

For special cases, such as the solar chimney, this is not always a good approximation. The third mode may contribute just as much as the first mode to damping, with the second mode contributing less. Furthermore, it is more difficult to estimate the damping ratio of the m^{th} mode than that of the lower modes. For any two values of ζ and ω, α and β can be solved as follows (Cook *et al*, 2002).

$$\alpha = \frac{2\omega_1\omega_2(\zeta_1\omega_2 - \zeta_2\omega_1)}{(\omega_2^2 - \omega_1^2)}$$
$$\beta = \frac{2(\zeta_2\omega_2 - \zeta_1\omega_1)}{(\omega_2^2 - \omega_1^2)} \tag{4-5}$$

By back-substitution into equation (4-4) the damping ratio for each mode can be calculated. Although the β term may cause the damping to become very large for higher modes, these modes usually contribute little to the global response of the system. An accurate calibration of the β value is important however, when it is essential to describe the damping of high-frequency vibrations (noise).

4. 5 Alternative damping methods

As a result of the limitations of the generally accepted methods of describing damping, and its dependence on the knowledge gained from measurements, researchers on the subject are trying to develop alternative ways of dealing with damping. There is a growing need for a generalised method for describing damping in any conceivable structural geometry. This section will look at two alternative methods that are being developed by referenced researchers.

4. 5. 1 Damped Spectral Element Method (Horr *et al*, 2003)

This technique proposes that the solution of the dynamic equation is done in the frequency domain. The general differential equation of motion is re-written in the spectral form. The solution to the problem in the time domain is then the Fourier transform of the solution in the frequency domain. The mathematical formulation for an axial element is done as follows (^-terms represent frequency domain):

$$\frac{\partial^2 u}{\partial x^2} = \lambda \frac{\partial^2 u}{\partial t^2}; \quad \lambda = \frac{\rho}{E} \rightarrow \quad \frac{\partial^2 \hat{u}}{\partial x^2} + \omega^2 \lambda \hat{u} = 0 \rightarrow \quad \frac{d}{dx}\left[EA \frac{d\hat{u}}{dx} \right] + \omega_n{}^2 \rho A \hat{u} = 0 \qquad (4\text{-}6)$$

Where u implies displacement at a point x along the element, t refers to time, λ is a constant material coefficient, ω is the pulsating frequency, E is the material elasticity modulus and A the element's sectional area. The relation to the traditional way of writing the matrices for the dynamic solution can be represented as follows:

$$\overline{\overline{\hat{K}}} = \overline{\overline{K}} - \omega^2 \overline{\overline{M}}; \quad \overline{\overline{\hat{K}}} \cdot \quad \overline{\overline{U}} = \overline{\overline{F}} \qquad (4\text{-}7)$$

Where $\overline{\overline{\hat{K}}}$ is donated the complex dynamic stiffness matrix. The E-modulus in this matrix is described by a complex term, where the constitutive relationship is formulated using the complex uniaxial, biaxial and triaxial moduli. Using only the first fractional derivative term in each series of the constitutive equation of concrete material, and taking the Fourier transform, a complex relation between stress and strain can be obtained. In the following equation a, b, c, e, and f are model parameters.

$$\begin{aligned} &\sigma(t) + aD^b \overline{\overline{\sigma(t)}} = e\varepsilon(t) + fD^c \overline{\overline{\varepsilon(t)}} \rightarrow \quad Fourier \rightarrow \quad \hat{\sigma}(i\omega) + a(i\omega)^b \hat{\sigma}(i\omega) = e\hat{\varepsilon}(i\omega) + f(i\omega)^c \hat{\varepsilon}(i\omega) \\ &\hat{\sigma}(i\omega) = \frac{e + f(i\omega)^c}{1 + a(i\omega)^b} \hat{\varepsilon}(i\omega) \rightarrow \quad \hat{\sigma}(i\omega) = \hat{E}(\omega)\hat{\varepsilon}(i\omega); \quad \hat{E}(\omega) = \frac{e + f(i\omega)^c}{1 + a(i\omega)^b} \end{aligned} \qquad (4\text{-}8)$$

By rewriting the λ term in (4-6) in terms of the complex frequency (iω) (by substituting E with $\hat{E}(\omega)$) the complex form of the Elasticity modulus is obtained. Now the dynamic stiffness matrix includes the fractional derivative module in the spectrum and will decrease the sectional modulus in the element due to cracking, crushing and yielding. Thus the damping effects are already included in the dynamic stiffness matrix, and there is no need for a damping matrix anymore.

In order to assess damping, this non-linear approach proposes an alternative method to the classical proportional damping technique. But the method relies strongly on the non-linear frequency behaviour of material such as concrete. Until the damping (cracking, crushing and yielding) properties are better understood, the practicality of this method stays fairly futuristic.

4. 5. 2 Reinforced beam computational logdec method (Salzman, 2003)

The total logdec of a concrete beam at any point in its service life can be calculated as the sum of the untested logdec (before cracking) and the tested logdec (after cracking). The idea of formulating an equation for the untested logdec was first proposed by Lazan (1968) who claimed that it would be a function of the properties, number and location of the reinforcing bars.

Although damping capacity equations exists for the prediction of logdecs in solid concrete cylinders based on the properties of the concrete constituents (Swamy and Rigby, 1971), this formulation could not be applied to other concrete members. Salzman (2003) further investigated Lazan's theory by means of extensive testing of reinforced concrete beams with varying reinforcement configurations. From experimental tests the following equation was suggested:

$$\delta_{untest} = 0.223 \times \left(\frac{\rho_t}{s_t} + \frac{\rho_c}{s_c} \right)^{0.19} ; \rho_t = \frac{A_{st}}{bd}; \quad \rho_c = \frac{A_{sc}}{bd} \tag{4-9}$$

where s_t and s_c are the tension and compression reinforcement spacing respectively. Salzman found the variation effects of concrete compressive strength and reinforcement yield strength to be negligible for the tested beams. To calculate the total logdec value, a method for calculating the tested logdec was developed as well. An equation was developed to predict the residual deflection (Δ_r) of the beams. The total logdec is then given by the following expression:

$$\delta_{total} = \beta_{fl} \Delta_r + \delta_{untested}; \quad \beta_{fl} = 0.0007 e^{0.018 f_{cm}}; \quad 22.5MPa < f_{cm} < 90.7MPa \tag{4-10}$$

where f_{cm} is the concrete compressive strength.

Although this study is limited to certain beam geometries, this investigation bring analysts one step closer to being able to assess the damping parameters in reinforced concrete members accurately.

4. 6 Applicability to the solar chimney

With reference to the different types of damping, the solar chimney will mainly be a combination of coulomb and hysteretic damping. Viscous damping, which will exist as a result of aerodynamic damping, will be minimal, as the weight and size of the structure in comparison with air density and the low speed at which the structure passes through it, will cause minimal drag effects. However, it would not be unrealistic to model the damping as viscous, as the combined hysteretic and coulomb damping will have a similar effect. The theory of equivalent viscous damping applies.

Although the theory states that measured logdec is independent of frequency, measurements from different tower-like structures shows a tendency to higher logdec values with a decrease in the first eigen-mode frequency. The measurements shown in section 3 are not enough to prove this argument, but it forms a basis of what range of damping might be applicable to the solar chimney. From the available data, a logdec value of between 0.09 and 0.12 can be estimated for the fundamental vibration frequency of the solar chimney. This implies 1.43% to 1.91% percent of critical damping. This range agrees with the generally accepted range of damping ratio for concrete structures in the high amplitude range, as presented by Jeary (1986).

From the author's frequency analysis results presented in chapter 6 it is shown that the second mode's resonance peak is about six times lower than the first mode. Furthermore, there are little signs of high frequency resonance even at 1% of critical damping. The need to damp out higher modes is therefore not critical, and the lower frequency modes are dominated by the first mode. The need for calibrating each modal damping value does not arise yet, but depending on the wind loads (described in the next chapter) it might be important in some cases.

For the first load cases, a range of one to five percent modal damping will be tested. This will result in less damping at higher modes than actually exists. As this is conservative with respect to resonance response, the need for calibrating higher modal damping values will arise if higher modal resonance proves to be a problem in the case of the current assumption.

The Damped spectral element method will not be applied in this study as this method requires an in detail understanding of the non-linear behaviour of reinforced concrete. This type of research falls beyond the scope of this study, but in the light of the concluding remarks, the author finds it appropriate to present the possibility of this kind of analysis in this chapter.

Chapter 5

CHARACTERISING WIND

5. 1 General Remarks

Wind is the result of air moving in the atmosphere due to pressure differences. The speed and density of moving air exerts a force on any static object in its way. This force changes with time as the velocity and direction of air changes. The density of air varies in height as well, resulting in different speeds at different levels.

In most cases, structural dimensions are so small in comparison to the scale of the differences in air movement, that it can be assumed the structure is experiencing a constant pressure load, uniformly distributed over the whole exposed area. However, skyscrapers and high towers experience a variation in wind speeds with height. Building codes prescribe a vertical wind speed profile for tall structures, but this profile is limited to the layer in which air movement is highly effected by ground friction.

This chapter will look at the different variations of air movement potentially affecting the dynamic response of the solar chimney. Static or mean wind speed profiles are discussed in the light of the height of the solar chimney. It also looks at what happens in the higher parts of the atmosphere, above the boundary layer.

Air movement is not static. Different techniques exist to describe this fluctuation in velocity. A brief description is given of how a measured gust history is transformed to a gust spectrum. Scientists have proposed generalised gust spectra's; these are also briefly explained.

To understand local air movement, it is essential to understand the weather systems of the area under concern. The Upington area and its synoptic weather systems are discussed in the light of a meteorological study conducted by Environment Management CC in 1999. The effect of these systems on the vertical profile of air movement is also discussed.

The chapter ends with a short description of the possibility of stochastic analysis methods and an explanation of how the knowledge gained will be applied in the solar chimney analysis. A table of load cases is presented at the end of the last section.

5. 2 Static wind loads

Static wind loading is described by the criteria of the turbulent wind field. This implies that the following assumptions have been made with regard to the wind description:

Above geostrophic wind height (where the wind is independent of surface friction), the wind is assumed uniform horizontally.

A 10-minute observation period is applied to calculate the mean wind velocities. Therefore the wind is regarded as stationary at a certain height.

The direction of wind does not change with increase in height. Although this is not true (change in height does occur due to Coriolis force) it is so small that it does not affect tall structures. The total deviation over 1km height is about 20 degrees (Dyrbye & Hansen, 1997).

The total wind is then described as the mean wind plus gust or turbulence components. If the effect of the turbulence component does not need to be taken into account, only the mean wind will be applied to the structure, being regarded as a static pressure load (see figure 5-1).

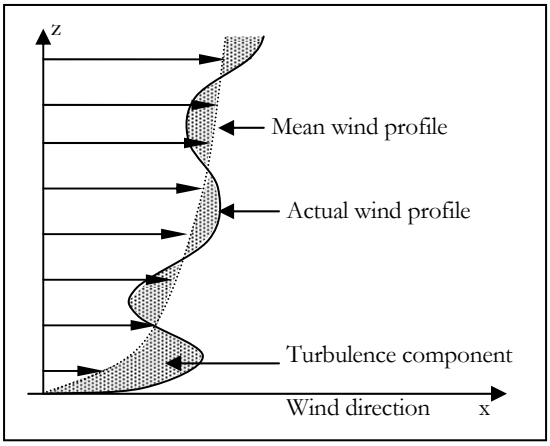

Figure 5-1: Momentary wind velocities (Dyrbye & Hansen, 1997)

The mean wind velocity profile is a smooth curve that can be represented by a mathematical formula. Different codes use different formula's to describe this curve. The most common formulation, the power law profile, has already been described in chapter 2. It was also mentioned that these formulations are subject to the effects of ground roughness and the boundary layer. This layer is more or less the height at which the effect of ground friction dies out (1km above ground), and the wind patterns are governed by geostrophic or gradient winds. Thus, 3 regions occur: friction influenced, boundary and geostrophic. The difference between geostrophic or gradient winds and wind in the boundary layer is the forces working in on a particle of air (see figure 5-2).

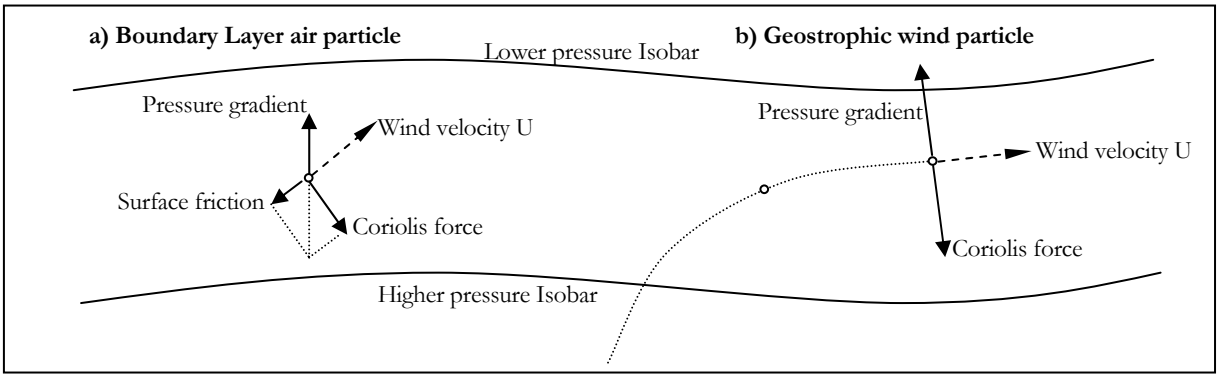

Figure 5-2: Force diagram of a) boundary layer and b) geostrophic wind (Dyrbye & Hansen, 1997)

Figure 5-2 also shows how the friction component of the boundary layer wind affects the direction with height (known as the Ekman-spiral).

Two characteristic length scales therefore affect the mean velocity curve. The surface friction close to the ground dominates the one and the other is dominated by the free flow at the top of the boundary layer. For the first part, Eurocode 1 (Dyrbye & Hansen, 1997) prescribes the logarithmic profile up to 200m above the ground:

$$U(z) = u_* \frac{1}{\kappa} \ln \frac{z}{z_0}; \quad u_* = \sqrt{\frac{\tau_o}{\rho}} \tag{5-1}$$

where τ_0 is the shear stress at the ground, ρ the air density, u_* the friction velocity, κ the von Karman constant (≈ 0.4) and z_0 the roughness length (0.01 for open land with little vegetation and few houses).

The corrected logarithmic profile is a more precise expression for heights above 200m above the ground. Harris and Deaves (1980) developed the following formula:

$$U(z) = \frac{u_*}{\kappa}\left[\ln \frac{z-d}{z_0} + 5.75a - 1.88a^2 - 1.33a^3 + 0.25a^4\right]$$
$$where: \quad a = \frac{(z-d)}{z_g} \; and \quad z_g = \frac{u_*}{6 f_c} \tag{5-2}$$

where f_c is the Coriolis parameter, d is the displacement of the base level due to obstacles like a forest or buildings in a city (d=0 otherwise), z_g is the height of gradient wind, and other parameters as previously defined. Up to 300m above ground the last three terms of (5-2) do not contribute significantly. This equation is valid up to the height where airflow becomes geostrophic and

stabilizes in velocity over height. The wind speed is then a function of the local weather system and isobar gradient.

The advantage of the logarithmic and corrected logarithmic profiles is that it can characterise wind velocity over two distinct air layers, tying it into the constant geostrophic region. The advantage of the power-law profile is its simplicity, fairly accurate up to 300m. Above this level the profile becomes very unrealistically exaggerated.

5. 3 Dynamic wind loads

The turbulence component shown in figure 5-1 is what causes the fluctuating nature of airflow referred to as gust. It is this component that will cause a structure to respond in a dynamic way. To characterise this behaviour is difficult, as gust is a random process. Its characterisation depends on the nature of the instantaneous fluctuations of pressure; hence it cannot be determined by normal averaging accelerometers. The whole process of obtaining data is unique in itself.

5. 3. 1 Measuring wind frequencies

The surrounding terrain plays a large role in the gust profile at a certain place on earth. It is unique in relation to space and time. To measure recurring frequency components, an average value of wind speed is needed over frequency instead of time. In order to obtain this, the Fourier transform may be taken of a time history of gusting wind (figure 5-3).

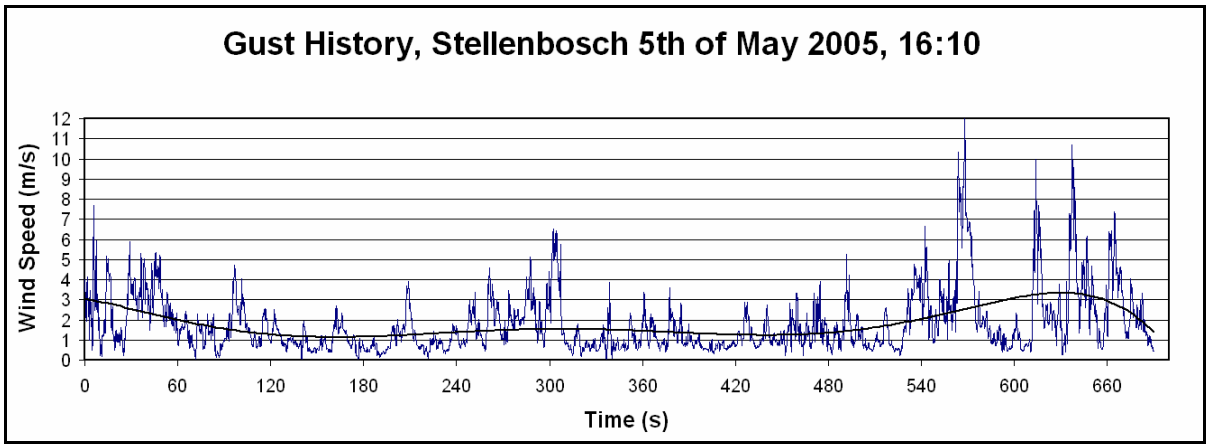

Figure 5-3: Typical gust history.

The longer the span of time the gust history is recorded over, the lower the frequency components will be resulting from the Fourier analysis. The following figure shows the frequency spectrum for the above time history. A curve was fitted to estimate the tendency of the frequency components.

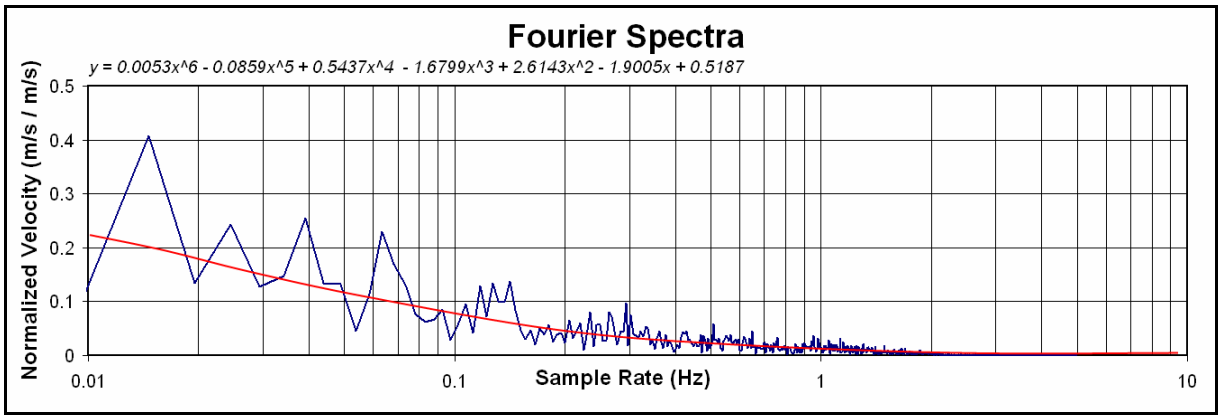

Figure 5-4: The log-scale velocity frequency spectra of figure 5-3.

The above graph was generated from measurements taken by the author with a home built anemometer at the University of Stellenbosch and University of Port Elizabeth in gusting wind conditions. The exercised confirmed the applicability of Davenport's spectral model of gust as will be explained in the following section. The development and design of this instrument is explained in Appendix A.

5. 3. 2 Generalised gust spectrums

Various scientists have done research to develop a generalised spectrum of gust that can be calibrated according to roughness and mean wind speed. These generalised formulas are derived from measured data from a number of different sites with different mean wind speeds and different roughness characteristics. Normalising the gust power spectrum with the square of the standard deviation of the mean wind and multiplying with the frequency can describe the frequency distribution of along wind gust components. The result is known as the non-dimensional power spectral density function $R_N(z,n)$ and is formulated as follows:

$$R_N(z,n) = \frac{nS_u(z,n)}{\sigma_u^2(z)} \tag{5-3}$$

where $S_u(z,n)$ is the gust power spectrum, n is the frequency and σ_u is the standard deviation of the mean wind speed. Note that when the power spectrum for total velocity needs to be calculated, $(\sigma_u)^2$ can be replaced by the average wind speed squared $(U)^2$ times the roughness coefficient k_r. (=0.005 for open grassland with few trees – Dyrbye and Hansen (1997)).

There are a few variations of the dimensionless power-spectral density function, but for simplicity only the relevant model by Davenport (1962) will be discussed. Figure 5-5 shows Davenport's power spectral density function (in a combined form of (5-3) and (5-4)) compared with Kaimal's equation.

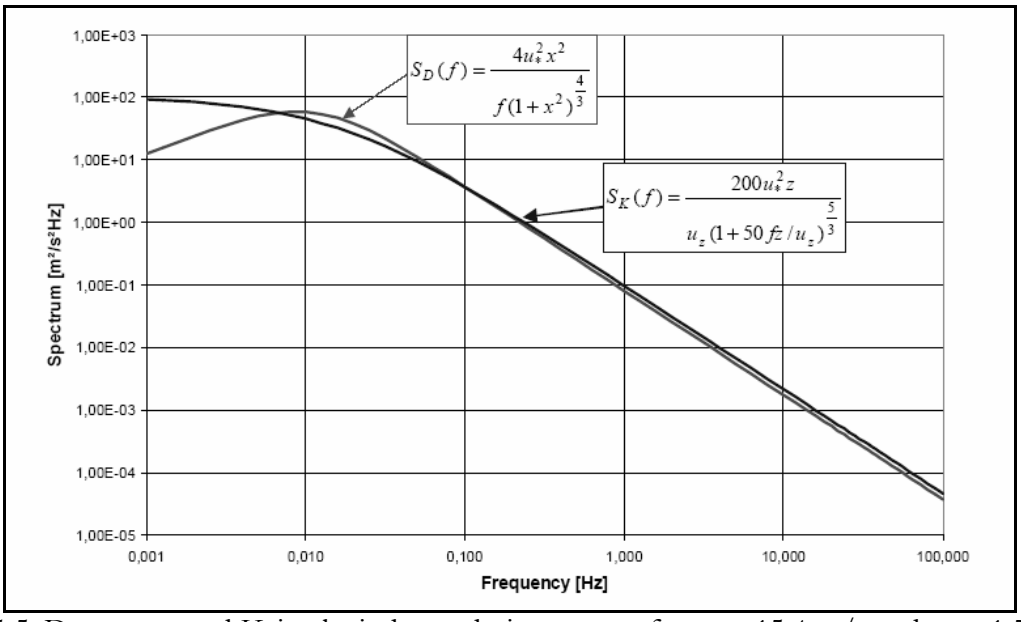

Figure 5-5: Davenport and Kaimal wind gust design spectra for u_z = 15.4 m/s and σ_u = 1.54 m/s (Emde *et al*, 2003)

Comparative studies have shown that the results of other spectrums show little difference to the Davenport spectrum in the high frequency range. Davenport proposed the following equation for the dimensionless power spectrum (Dyrbye & Hansen, 1997).

$$R_n(z,n) = \frac{2}{3}\frac{f_L^2}{(1+f_L^2)^{4/3}}$$
$$f_L = \frac{nL}{U(z)}; \quad L \approx 1200m \tag{5-4}$$

where U(z) is usually taken at 10m above ground level. When substituted into (5-3), the gust power spectrum can be calculated. The term in (5-3), $(\sigma_u)^2$ is related to the friction velocity u_*. It can also be assumed to be 10% of the mean velocity at a height of 10m.

With the gust power spectrum known, the velocity of each frequency component is known. The spectrum can be applied to the reduced system of equations of the physical model to calculate the resonating response at the eigen-frequencies.

5. 3. 3 Cross Correlation

Up to now the fluctuating behaviour of air has been discussed in the light of what happens at one particular point in space. For small surfaces it can be assumed that the behaviour of other spatial points close to the point under consideration will be quite similar. But for large structures, there might be no direct relationship between points at the bottom compared to points at the top. It is

therefore necessary to have a way of measuring the correlation of pre-selected points along the structure. Separate formulations exist for the horizontal and vertical cross correlation of airflow. However, air flow is better correlated in the horizontal than vertical direction, and furthermore, the geometry of tower-like structures often vary in the vertical direction. Davenport (1962) suggested an exponential expression for the vertical cross correlation of two points at a certain frequency *n*.

$$\psi_u(r,n) = \exp(\frac{-Crn}{U}) \tag{5-5}$$

where C is a non-dimensional decay constant, r is the vertical distance between two points and U the average wind speed. Davenport (1977) later suggested an expression for transverse correlation as well. However, there are two main points of critique against this approach:

The function is always positive for two points resulting in positive only values for the co-spectrum integral over the plane perpendicular to the mean wind velocity. This is in conflict with the definition of longitudinal gust component that should have a mean value of zero.

The function approaches unity for low frequencies at a constant separation distance. This is not always true, especially at large separations where the lack of correlation may be characteristic for low frequencies.

Krenk (1995) has modified the correlation expression, by assuming locally isotropic turbulence, with an exponential equation, avoiding the above-mentioned inconsistencies. The expression is based on the general form of a spectrum proposed by von Karman (1948)

$$\psi_u(\kappa_1, r) = \frac{2}{\Gamma(\gamma)}\left[\left(\frac{\kappa_1 r}{2}\right)^{\gamma} K_{\gamma}(\kappa_1, r) - \left(\frac{\kappa_1 r}{2}\right)^{\gamma+1} K_{1-\gamma}(\kappa_1, r)\right]; \quad \kappa_1 = \sqrt{\left(\frac{2\pi n}{U}\right)^2 + \left(\frac{1}{L}\right)^2} \tag{5-6}$$

with Γ as a Gamma function and K_{γ} and $K_{1-\gamma}$ as modified Bessel functions. This expression requires a more in depth explanation of stochastic functions, so it will not be discussed in further detail in this report.

5. 4 Weather systems affecting Upington

The direction, mean stationary and dynamic components of any real-time vertical wind profile are largely dependent on the local weather system present in the area. These local systems are, in turn, the effect of global air circulation. It is useful to take note of the weather systems near Upington in order to understand what variations of the mentioned components of wind may occur.

Upington's synoptic circulation is primarily influenced by the southern subtropical high-pressure zone (continental and the South Indian high pressure zones) and by transitory ridging anti-cyclones following the frontal depression path over the sub-continent (Burger and Scorgie, 1999).

During winter one of two scenarios can cause extensive wind activity. High-pressure cells break loose from the south reaching subtropical high-pressure zone. These anti-cyclonic cells move over the inner part of the sub-continent to be merged with the south Indian high-pressure zone. As they reach the east coast, a surface trough may develop over the west of the sub-continent, creating a pressure gradient resulting in strong westerly winds.

Low-pressure systems (cyclones) move from the south west of the sub-continent fuelling with moist air over the ocean as it approaches land. This creates a cold front; creating strong wind conditions as high-pressure air diverges in front of it. Severe wind conditions exist when a cold front approaches from the south. Figure 5-6 illustrates a ridging anticyclone moving toward the east over the escarpment. To the west another high-pressure system is taking shape. A cold front is passing over the southeast coast, which is typical of frontal systems moving from the southwest.

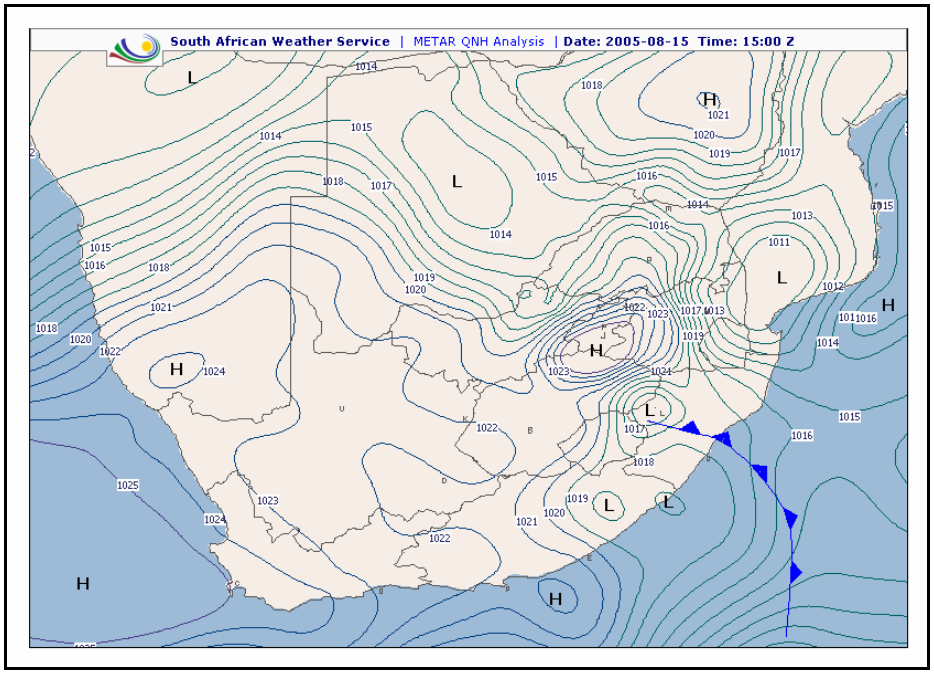

Figure 5-6: A synoptic chart of Southern Africa showing ridging anticyclones and a cold front (South African Weather Service)

During summer, hot conditions exist over the interior as air descends and heats adiabatically. Hot, high pressure, moist air moves in from the west coast and lifts upward due to the rising escarpment. Any disturbance can trigger upward drafts of this warm, moist air. During winter, cold fronts can cause the start of upward circulation, as the air in front of it needs to give way. As the

moist air rises and cools, condensation takes place and a large cumulonimbus cloud take shape (figure 5-7). The air movement caused by such a system can, for a short while, be very intense.

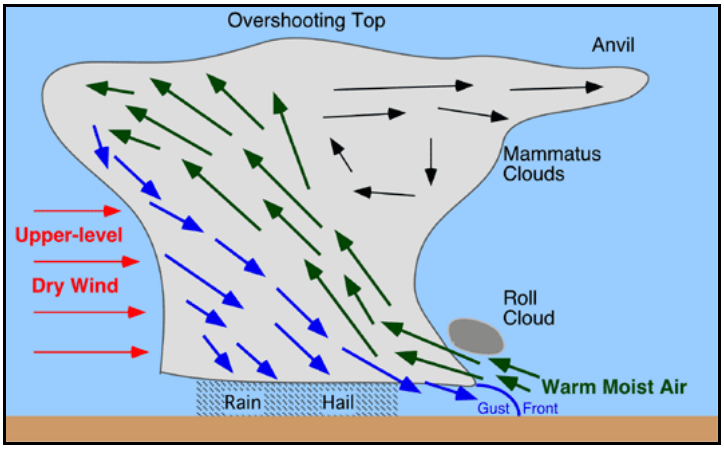

Figure 5-7: Formation of a thunderstorm (Pidwirny, 1995)

5. 5 Vertical direction profile

The above mentioned weather systems effect the direction and speed of winds at certain heights, depending on the characteristics of temperature inversions. Although the mathematical formulation of a vertical profile can show an extreme average wind speed, it cannot predict the direction variations over or above the boundary layer. In the case of tall structures, this phenomenon is important, as different directional pressure loads can cause oscillation of the structure in higher eigen-modes.

A study was conducted by Environmental Management Services CC to undertake a meteorological investigation for the Sishen region close to Upington, where the solar chimney is proposed to be located (EMS 1999). Although the study does not cover the dynamics of thunderstorms, it gives insight in the characteristics of the lower and upper air layers during anti-cyclonic conditions.

From the report it is clear that anticyclones (high pressure systems) cause temperature inversions at certain pressure heights. These inversions are situated at more or less 700hPa (≈3km amsl), 500hPa (≈5km amsl) and 300hPa (≈7km amsl). Cyclonic activity and cold fronts can reduce the base of the first inversion layer during winter, to fall well within 700m to 1500m agl (above ground level). Ridging anticyclones cause the first inversion layer to occur at 780hPa (≈1300m agl) on average. These systems are associated with strong winds. Figure 5-8 shows inversion layers for different South African weather stations at various pressure levels.

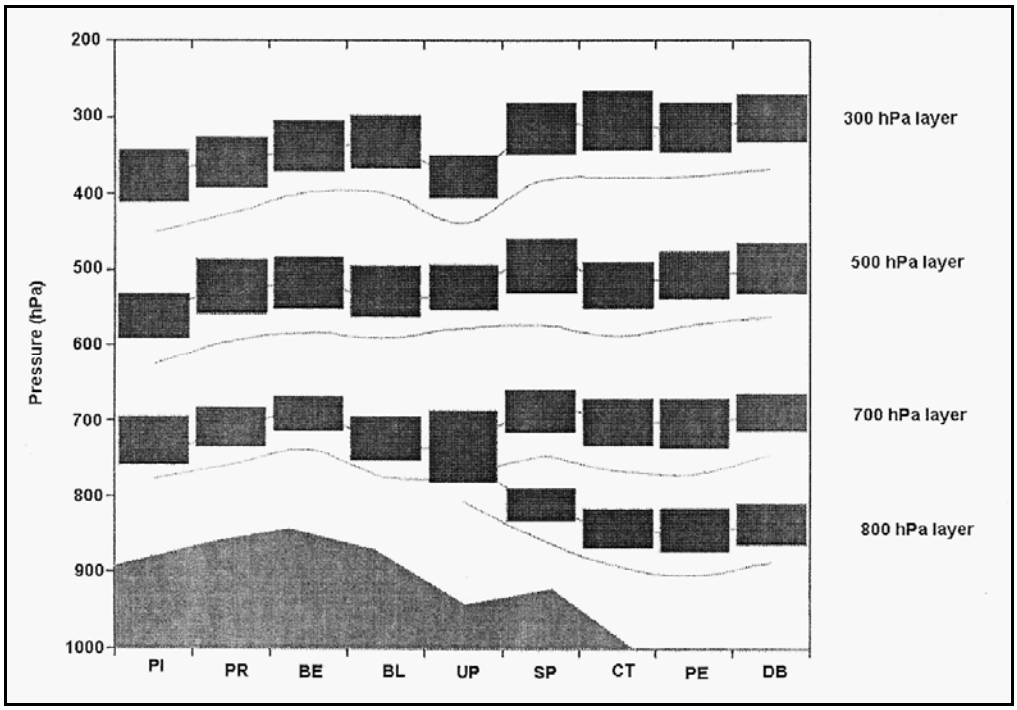

Figure 5-8: Upper air inversions over South Africa. UP represents Upington (EMS 1999).

Theron and Harrison (1991) describe temperature inversions to be dynamic and thermodynamic interfaces at which airflow interfaces reverse. While the surface winds occur below the temperature inversion, gradient winds start to prevail above the inversion level. This type of airflow is better correlated over height, and can result in steady winds of up to 30m/s below 2000m agl. Figure 5-9 shows radio sonde readings of wind speed and direction over Upington.

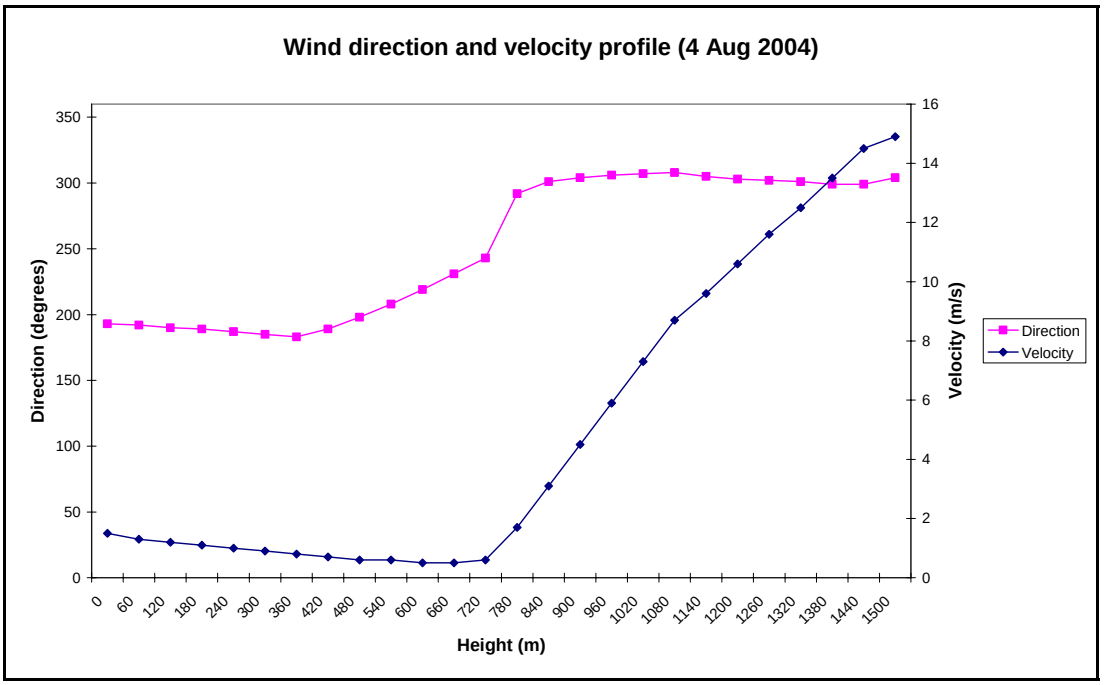

Figure 5-9: A typical effect of a temperature inversion on wind velocity and direction (at 780m).

Thunderstorms can cause airflow inversions as a result of local air movement in and out of the system. As the cumulus cloud sucks in air from the surrounding area it builds until it reaches its anvil stage. When the cloud becomes saturated, downbursts develop as turbulent air leaves the cloud downward through its centre. This type of air movement is known as a downburst.

Downbursts occur in the form of eddies tumbling down the inside of the cumulonimbus cloud. When they reach the ground they spread out sideward and lift the warmer moist inflowing air upward. Downbursts occur suddenly and violently, causing gust winds near the surface as a result of turbulent eddies. Such turbulence may contain higher frequency components than normal gusting turbulence. If eddies reach diameters of up to 1000m, they can cause wind direction inversions similar to a temperature inversion, but with more severe gust in the upper level.

The precise dynamics of downbursts and gusts in thunderstorms are unpredictable and random. It is therefore difficult to describe this phenomenon in mathematical terms. Figure 5-10 shows the dynamics in a downburst under a thunderstorm cloud.

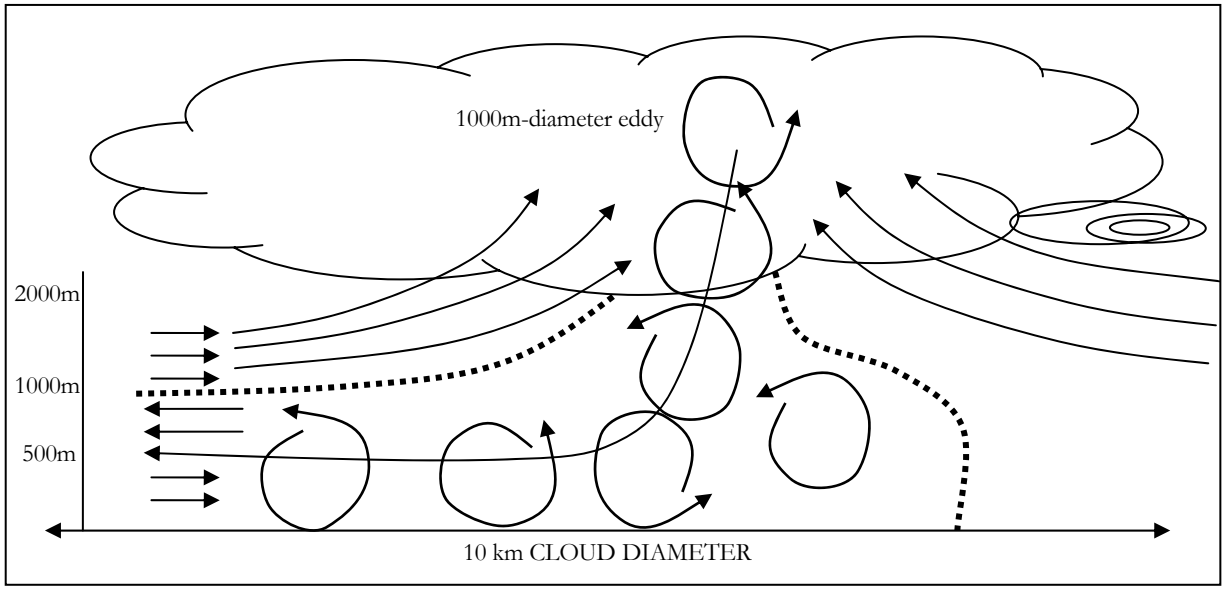

Figure 5-10: Development of airflow inversions in a Thunderstorm

5. 6 Stochastic analysis of wind

From the above discussion, one can conclude that there are three random variables with regard to wind: Recurrence of wind velocity at one spatial point, correlation between wind velocities at spatial points and wind direction. All three load-variables can vary at random independently. The best way to treat them in a dynamic analysis would be to characterise their statistical regularities and incorporate them in the dynamic transfer function.

This is possible with the stochastic dynamic analysis approach, where provision is made for a load cross correlation matrix. The answer obtained from this analysis is a stochastically described response. The response amplitude will have a probability distribution, making it possible to choose what value of certainty is satisfactory. From classical probability theory maxima values and extreme values can be calculated.

The cross correlation matrix will consist of correlation descriptions for each degree of freedom in terms of the others. The correlation models, mentioned in 5.3.3, might be of particular use here. Within the cross correlation matrix the terms on the diagonals will have a probabilistic description of what the correlation of spectral pressure energy (derived from velocity) is over time at the point itself.

To develop such a model will need mathematical expertise and time. It is worth mentioning this technique, but due to the nature of this study it will not be exploited further here.

5. 7 Wind load simulation for the solar chimney

Although it may be impossible to predict the worse case scenario of wind load on the solar chimney, using the above techniques and measured records can make an accurate estimation in predicting a vertical distribution of pressure load.

5. 7. 1 Vertical profile

The vertical profile will be calculated with a combination of (5-1) and (5-2) up to 1000m. In the zone from 200m to 1000m, the wind is highly to partially influenced by surface friction. Above 1000m the wind speed will stay constant, as geostrophic wind is assumed to take over at this level. The speed will, in a second load case, be adapted to match the maximum geostrophic wind speeds measured over De Aar (45.2m/s), another Karoo weather station southeast of Upington (see figure 5-11). The calculated vertical profile is presented in Appendix D.

5. 7. 2 Gust component

The gust component will be simulated by means of a spectral distribution. As shown by tests conducted at two gusty locations in South Africa, Davenport's power spectral density for gusting wind is a realistic description and applicable in the relevant frequency range. By using this power density spectrum, the gust speed component at each relevant frequency increment can be calculated. A time history was generated to compare the model with measured data and is presented

in Appendix B. However, when applied in the Diana analysis, the gust spectrum was expressed as a percentage of the mean wind speed.

5. 7. 3 Directional component

From the meteorological knowledge of the Upington region, it is clear that wind direction inversions are a frequent phenomenon. This can affect the response of higher modes in the solar chimney. To test this effect three direction load-cases will be applied. The first will be in one direction only; the second will turn 180 degrees at 750m; the third load case will change 180 degrees at 500m and change back to the first direction at 1000m high. Load Case 3 may result from airflow inversions due to thunderstorm activity (see figure 5-10).

Table 5-1 summarises the load case numbering applied to the solar chimney.

Directional variation	**45.2m/s Extreme maximum**	**30m/s Maximum average**
0 – 1500m	Load Case M.1	Load Case A.1
0 – 750m – 1500m	Load Case M.2	
0 – 500m – 1000m – 1500m	Load Case M.3	

Table 5-1: Load Cases applied to the solar chimney

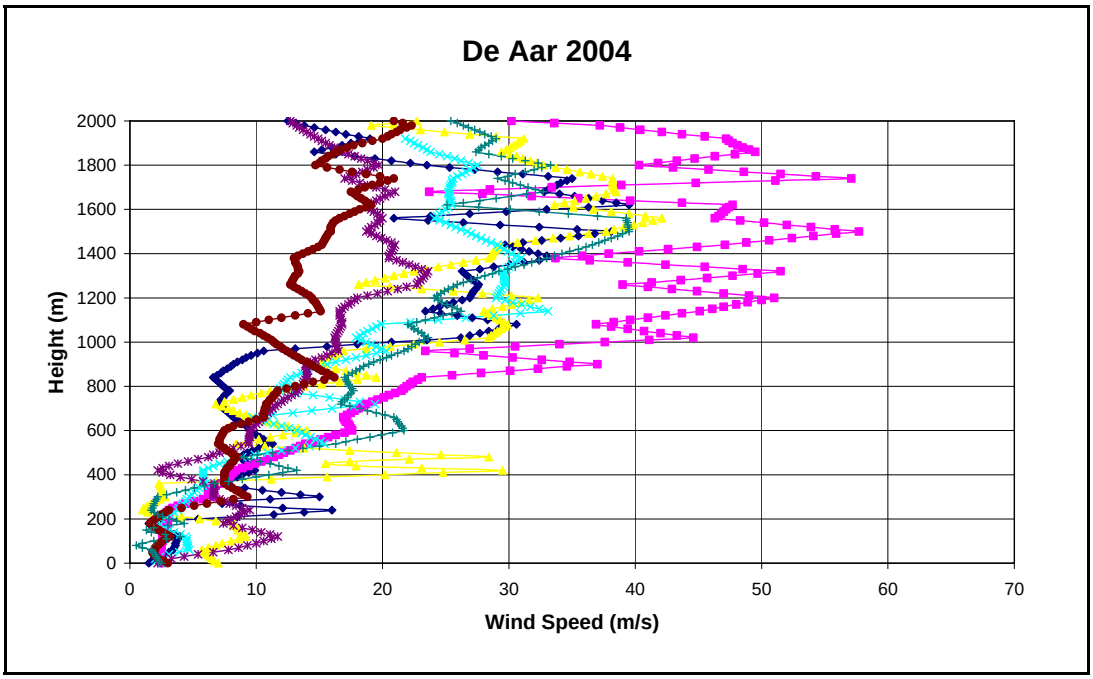

Figure 5-11: De Aar gust velocities for January 2004 (South African Weather Service, 2004)

5. 8 Chapter Summary

This chapter investigates the behaviour of gusting wind over a higher profile than commonly used in the building industry. The popular power law profile is not applicable where wind profiles need to be calculated above the boundary layer. The gradual change from friction influenced wind to free flowing geostrophic wind is taken into account by the corrected logarithmic profile, and therefore provides a more realistic estimation of the vertical wind profile.

Gusting wind is a random process that can be described in the frequency domain by means of a power spectral density function. The chapter mentions the author's own experimental gusting results as confirmation to the utilization of Davenport's power spectral density function. Further information on this topic is presented in Appendices A and B.

The chapter explains the weather systems prevalent in the Upington area in order to understand the geostrophic air flow behaviour. Furthermore, the investigation done by Burger and Scorgie (1999) points out that temperature inversion may have a noteworthy effect on the local direction of the vertical profile over the height of the chimney. This is confirmed by radio sonde data obtained from the South African Weather Service.

The chapter ends with an explanation of how the above mentioned information will be applied in the dynamic analysis of the finite element solar chimney model.

C h a p t e r 6

RESULTS OF THE DYNAMIC ANALYSIS

6. 1 Introduction and Outline

It is clear from the foregoing chapters that the solar chimney is subject to a range of possible loads and energy dissipaters. The ideal choice of parameters for the analyses conducted in this study would be such that the results represent the behaviour under realistic, extreme dynamic loads and damping values encountered in the structure's lifetime. However, chapters 4 and 5 made it clear that it is not possible to define an exact extreme load. It would be more realistic to identify a range of parameters that may encompass the extreme load case.

This chapter will present the results of the various dynamic analyses based on the damping and loading ranges as proposed and motivated in chapters 4 and 5.

It sets out to explain the method of presenting the response and how it should be interpreted. For a more complete and in depth explanation the reader will be referred to the Appendices concerned.

Two possibilities of dynamic amplitude spectra's are shown briefly. The reason for the difference ties in with the explanation on response representation.

The results presented start with a comparison of a range of damping factors, from 1% to 5% of critical damping. The significance of the results is commented upon, and an equation presented to characterize the trend.

Three possible vertical directional profiles are compared and discussed. To amplify the effect the results will be based on the extreme load case as defined in chapter 5.

The difference in the maximum mean velocity load case and the extreme velocity load case will be highlighted and commented upon.

Due to the pressure distribution around the cylinder a local dynamic effect occurs at the ring stiffeners. This ovalisation phenomenon will be shown graphically and discussed briefly.

This chapter will only comment on the results where it is important to understand and interpret the behaviour correctly. Critical comments will be made in the next, concluding chapter.

6. 2 Dynamic representation

Representing dynamic results require some fundamental understanding of representing response in the frequency domain. In this study all dynamic results will be shown in the form of response spectral graphs.

The simplest way to present a dynamic result is by means of an animation, showing the motion of the structure over time. A time-domain analysis can yield such a result, but since the goal of the study is to investigate resonance, it is important to assess the extent of the structure's response at different frequencies. By considering a load history as the sum of a number of sinusoidal loads (load spectrum), the response can be described as the sum of a number of sinusoidal responses (response spectrum). Each response occurs at a different frequency. From such a result it is easy to see the effect of different amplitudes plotted against their corresponding frequencies. It is thus more intuitive to see at which frequencies extreme resonance may occur. A frequency domain analysis was conducted with finite-element dynamic software package, TNO Diana. It is, however, important to bear in mind that a frequency's amplitude in a spectrum resulting from such an analysis is a vector of (part of) the true response. A time history can be generated from the various response spectra if needed.

Appendix B shows the mathematical procedure to generate a velocity time history from a gust power spectral density (PSD) equation. The aDFT is generated from the history or directly from the PSD. The amplitudes of the aDFT are a function of the size of the frequency increment chosen when converting from a PSD to an aDFT. The frequency increment in the aDFT is a function of the total time over which the data set was recorded. It is not known what these parameters are as the time history under concern was generated artificially by the author, from Davenports's (1967) gust PSD. Therefore the pulsating frequency bandwidth has to be estimated.

By guessing the recording time and time steps, two possible frequency increments were suggested: 0.01Hz and 0.02Hz. The higher frequency increment resulted in higher amplitudes, which, conservatively, was used in the dynamic loading spectrum. For presentation purposes the response spectra's are shown from 0 to 0.5Hz in 0.01Hz increments, as there is negligible or no response at higher frequencies. The response at a multiple of 0.01Hz is the response value of the gust energy root mean square (RMS) with a 0.02Hz bandwidth.

Figures of the model will show the dynamic amplitude of the oscillation with a graded colour scheme. These values are the complex magnitude of the complex result that describes the

oscillation motion. A representation of the shape will also be displayed with the colour scheme. These figures are usually over exaggerated by a factor, and show the motion at a certain phase angle (usually the furthest away from the neutral position). Figure 6-1 shows the first mode at 0.1Hz for a 42.5m/s wind with 1% of critical damping.

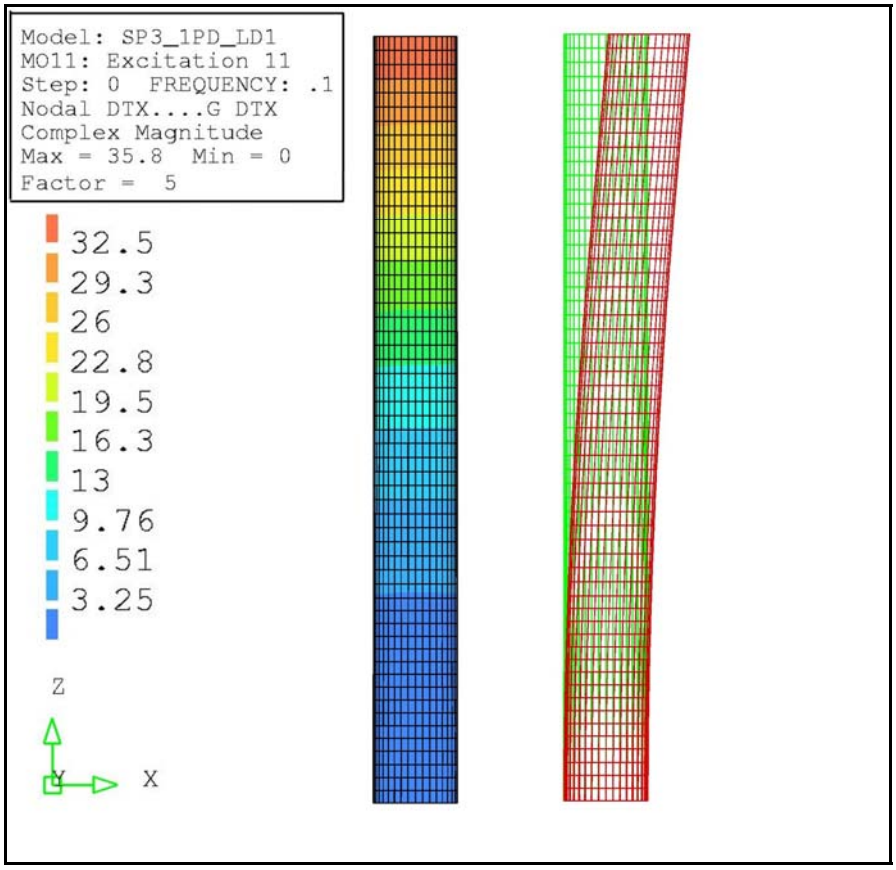

Figure 6-1: Eigen-mode 1 at 0.1Hz, 42.5m/s wind load, 1% damping

6. 3 Damping sensitivity

To estimate the effect of damping on the system, the simulation was done with varying damping values, ranging from 1% to 5% in increments of 1%. Although higher damping will occur at higher modes, the same percentage of critical damping was assumed for all modal frequencies, as the effect of the higher modes was very little even with low damping. Therefore, this approach can be considered as conservative concerning higher resonance modes. Figure 6-2 shows the response spectra's at the maximum response at the top of the tower.

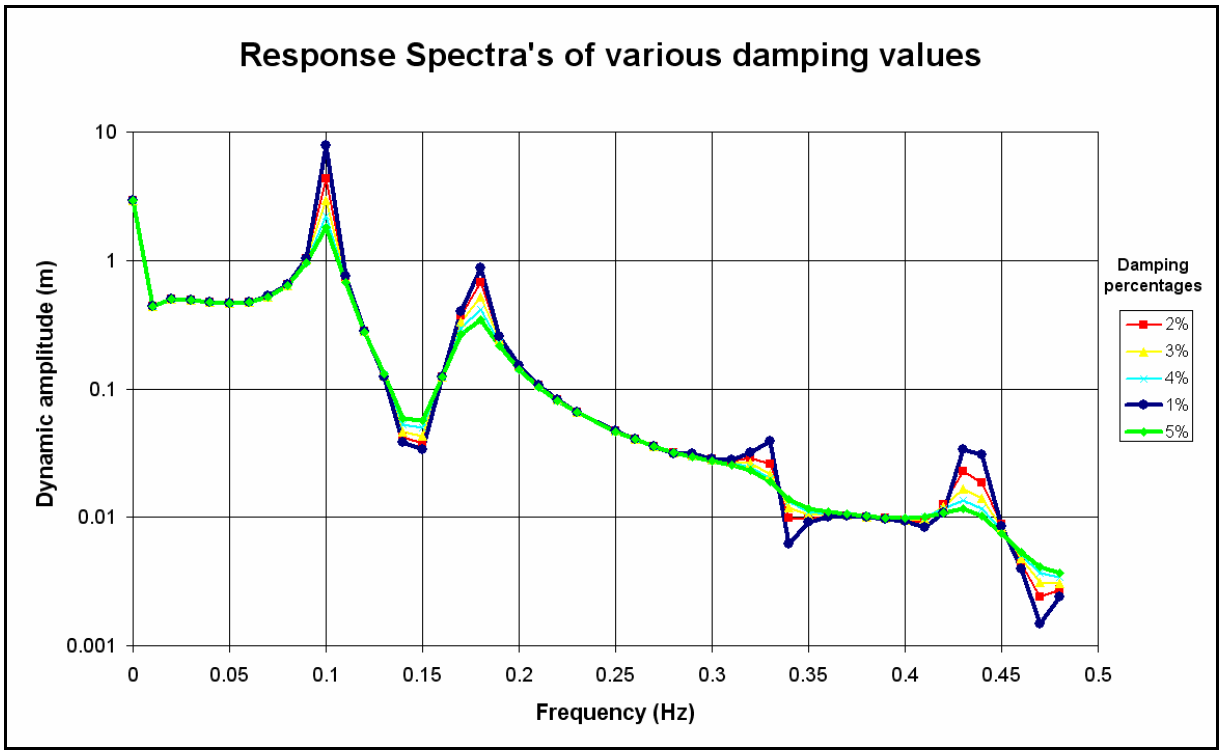

Figure 6-2: Response spectra's of various damping values

The dynamic amplitude curve becomes less as the percentage of critical damping increases. Figure 6-3 presents an equation for the rate of decay of dynamic amplitude, at the fundamental structural frequency, for a 30m/s gust wind blowing in one direction.

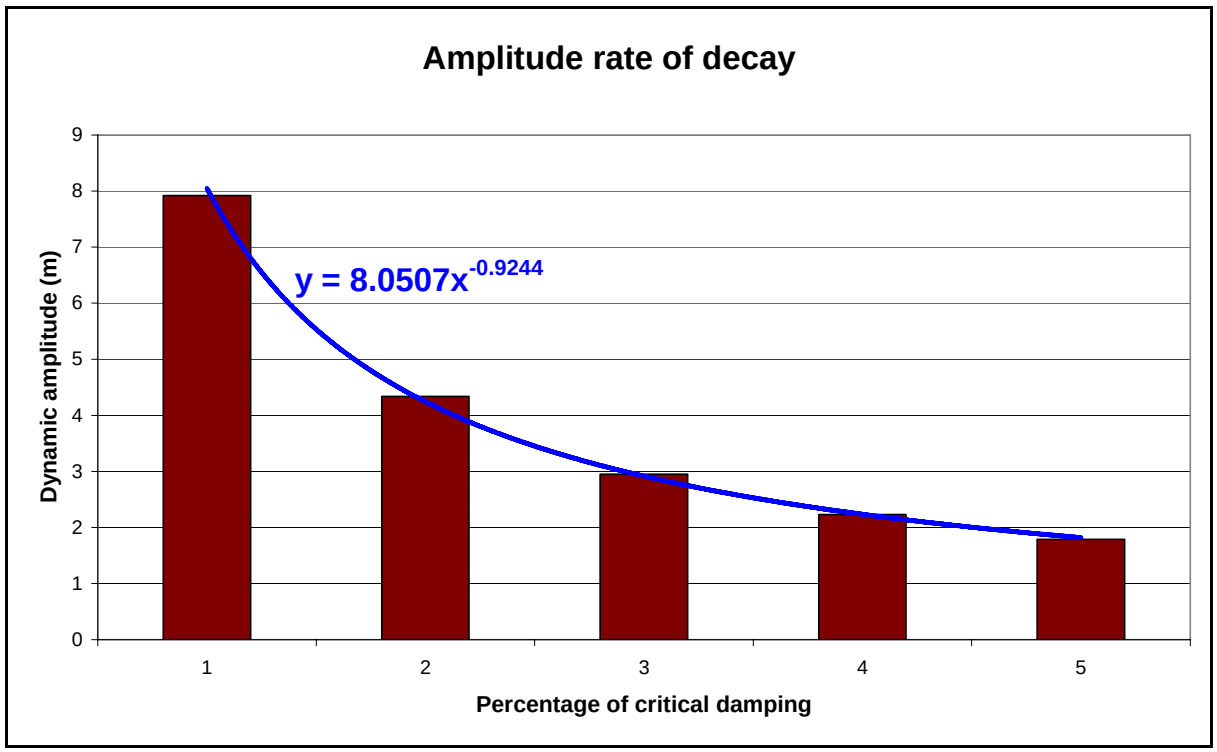

Figure 6-3: The decay rate of Response amplitude with increase in damping

Between one and 3 percent of critical damping, the increasing effect of damping has a considerable effect on reducing the resonance amplitude. From 4% to 5% the amplitude decreases with 0.44m as opposed to a 3.58m difference between 1% and 2%. From 5% damping onward, the decreasing amplitude effect becomes small. At 5% damping the dynamic amplification factor is 1.6.

6. 4 Inverting load directions

Three load cases were tested (at 1% of critical damping) with regard to inverting wind directions. The analyses assumed maximum wind velocity (42.5m/s maximum) and gust conditions to show the response more clearly. The three load cases (LC) are shown in figure 6-4 and proposed and argued in section 5.7.3.

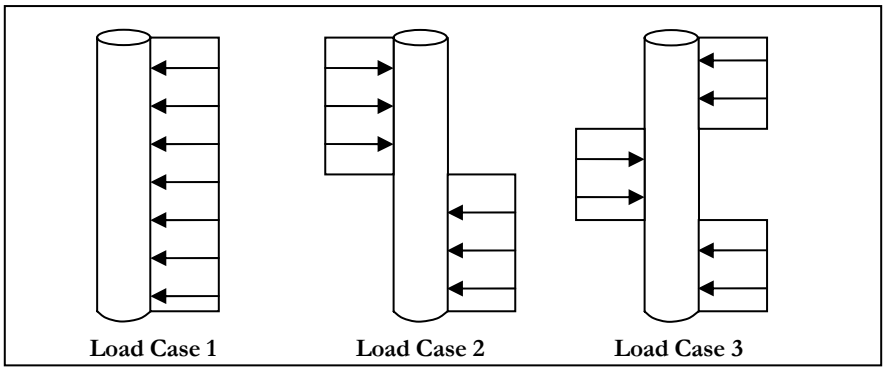

Figure 6-4: Three inverting wind load cases showing direction, not wind speed, which varies over height.

The static response (at 0 Hz) will be different for the three load cases as the resulting load vector changes. Figure 6-5 shows the log-scale response to frequency (at the top of the tower next to the symmetry axis) for LC1 to LC3.

As a result of the change in direction, it is expected that LC2 and LC3 can amplify eigen-modes where the eigen-vectors correspond to the load vectors. LC3 resembles the fifth eigen-mode shape (figure 3-5), thus it is not surprising that, even though the static response is less, LC2 and LC3 show much higher amplitudes at 0.33Hz (mode 5) than LC1. At 0.1Hz (mode 1) LC3 shows the smallest amplitude since the height of the top pressure distribution (that activates mode 1) is the smallest. At the static state, however, LC2 shows the smallest deflection as the resulting pressure load on the whole tower is minimal. Figure 6-6 shows the global response of the fifth mode for LC3.

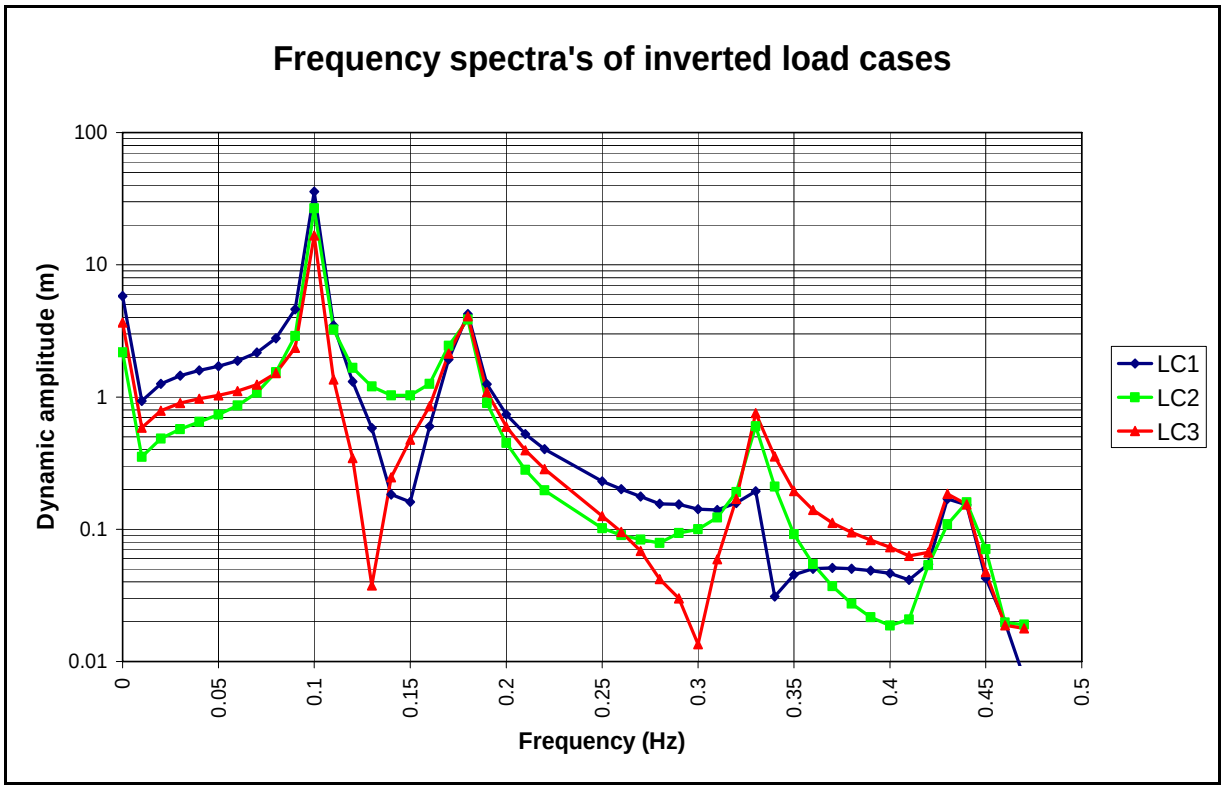

Figure 6-5: Logarithmic plot of LC1 to LC3 dynamic amplitudes

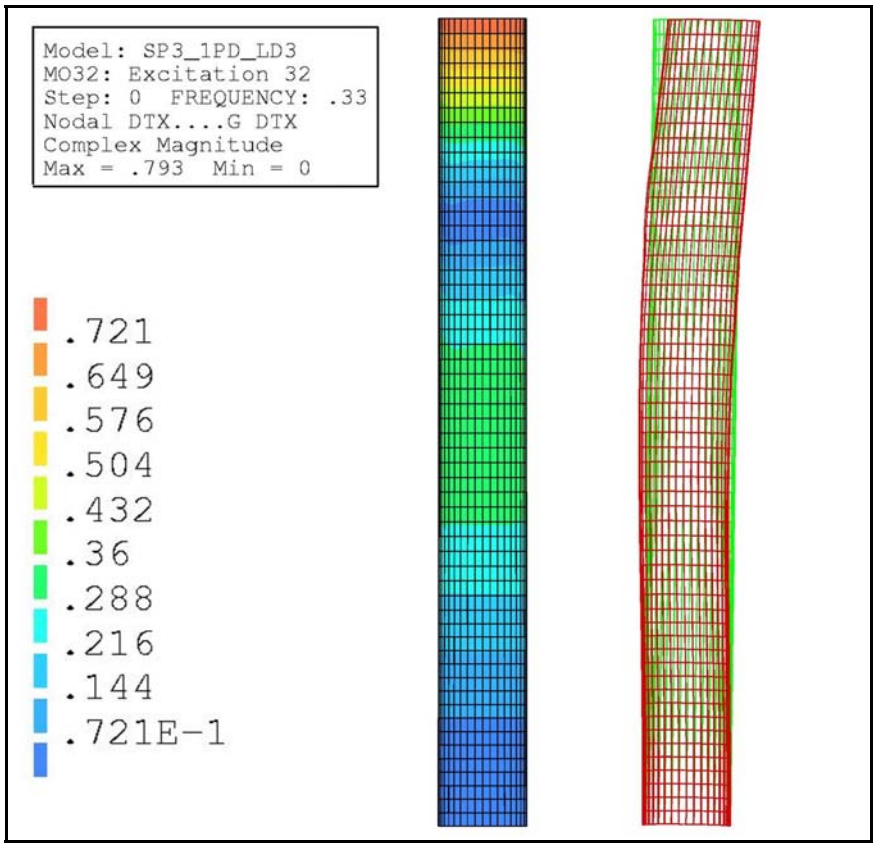

Figure 6-6: Response at the fifth eigen-mode for LC3

The amplitude response of LC1 at 0.33Hz is 0.19m. With LC3 it is 0.793, just over 4 times higher. Although these amplitudes seem small in comparison to the amplitude at the first mode (16.7m for LC3) it can still result in significant stress levels as the oscillation period is much less (3 seconds appose to 10 seconds) and the length over which the displacement occurs is much less (i.e. the curvature is larger for a given displacement).

At 0.43Hz, another significant resonance occurs at the 7th mode. As this is a local eigen-mode activated by the local pressure force in the top part of the chimney, this peak shows the same amplitude for all three load cases. Figure 6-7 shows the dynamic response at 0.43Hz.

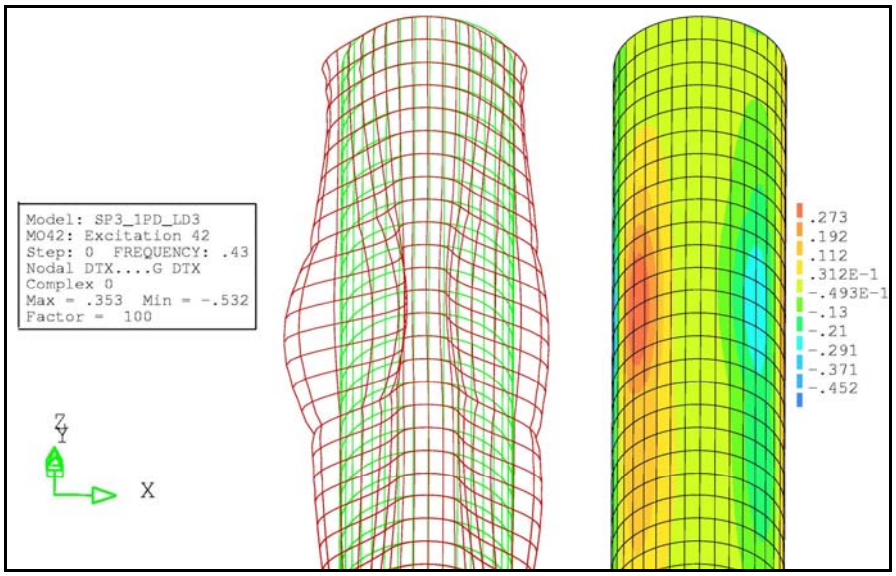

Figure 6-7: Directional response at 0.43Hz, Load Case 3, 100 times enlarged.

6. 5 Two measured mean velocities

Although the EMS report (1999) mentioned in chapter 5 states that the maximum geostrophic winds measured over Upington does not exceed 30m/s, measurements over de Aar, also located in the Great Karoo, showed averages of 42.5m/s at geostrophic heights. A 42.5m/s mean velocity with a 6m/s gust was applied to the tower to see if the greater velocity would result in different behaviour. Figure 6-8 shows the 30m/s vs. the 42.5m/s wind load dynamic amplification factors at the top of the tower.

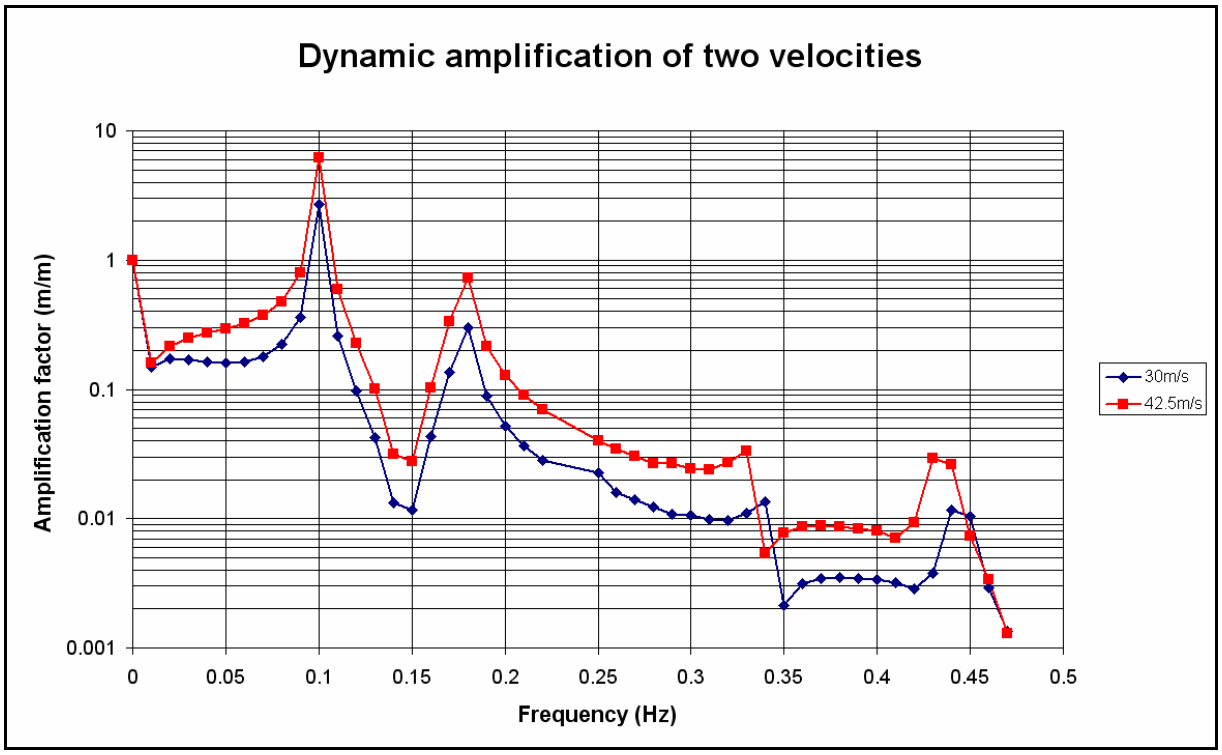

Figure 6-8: Two tested mean wind velocities

When increasing the mean geostrophic velocity by a factor of root two, the whole vertical velocity profile merely shifts with root two at each level as well. The static response curve doubles, since the relation between wind speed and wind pressure is quadratic. Not only do the values increase non-linearly, the peak of the PSD shifts to slightly higher frequencies.

The factor of the gust amplitudes to the mean wind speed is higher at 42.5m/s than previously. From 0 to 0.1 Hz the effect of the shifted PSD peak can clearly be seen in the logarithmic dynamic amplification spectrum, presented in figure 6-7. The maximum dynamic amplitude at 30m/s is 7.92m at 0.1Hz with a static displacement of 2.91m and the root mean square value (calculated from 0.01 Hz to 0.48 Hz) is 8.22m. At 42.5m/s the maximum amplitude is 35.8m at 0.1 Hz with a static displacement of 5.81m and the root mean square value (calculated from 0.01 Hz to 0.48 Hz) is 36.986m.

6. 6 Ovalisation

As a result of the pressure distribution around the parameter of the solar chimney and 2nd order reaction to bending, the circular section shape is warped. This is the same deformation industrial chimneys experience, mentioned in chapter 2. The difference is, in this case the warping is dynamic. Figure 6-9 shows the dynamic amplitudes of the oscillation and its relative static deformation.

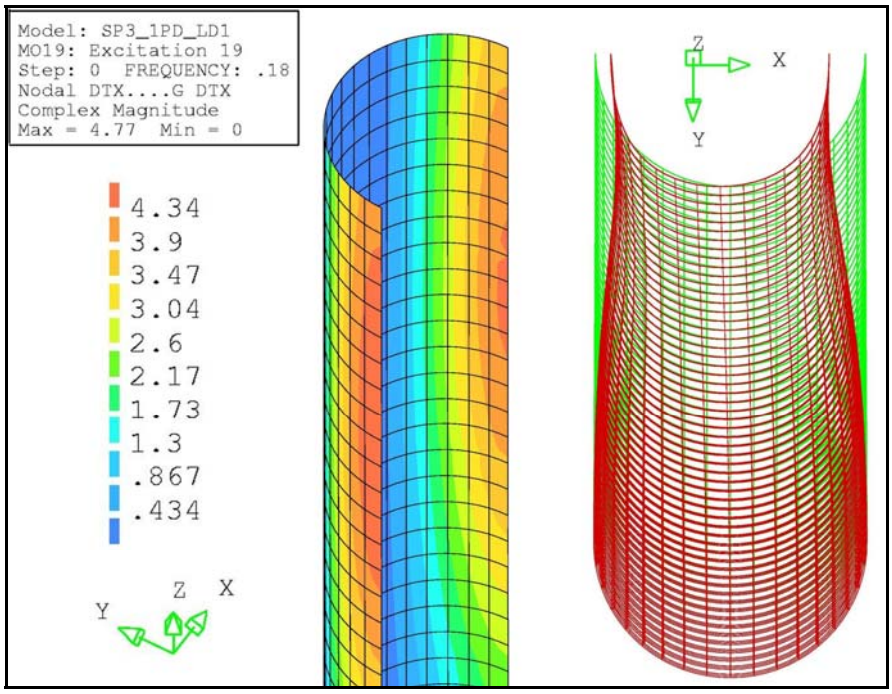

Figure 6-9: Ovalisation at the second eigen-mode

As the wind gusts by the chimney and fluctuates in speed, the pressure distribution fluctuates as well. The resonance effect may be amplified if the frequency of vortex shedding is close to the frequency of the second eigen-mode. This is not taken into account in this study. The situation is simplified in the sense that it is assumed that the pressure distribution remains the same for any wind speed. This, however, is not exact, because the pressure distribution is Reynolds Number dependent. Further studies on the flow regime around the perimeter should take note of this limitation in this analysis.

Another simplification one needs to bear in mind is the constraint assumption at the ring stiffeners (see chapter 3). Schindelin (2002) proposed that the ring stiffener constraints could be modelled by restraining the vertical-directional rotation dofs (see figure 6-10).

For a load operating in the horizontal plane, the only degrees of freedom at the ring stiffeners are in the x or y (horizontal) directions. This means that the elements can stretch and compress only in their longitudinal reinforcing directions. The concrete shell element is the stiffest in this direction. The least stiffness is in the bending direction perpendicular to the element plane, which, in this case, is restrained by the vertical rotational constraints (figure 6-10). The validity of this approximation will depend on the actual constraining effect of the eventual implemented ring stiffener system.

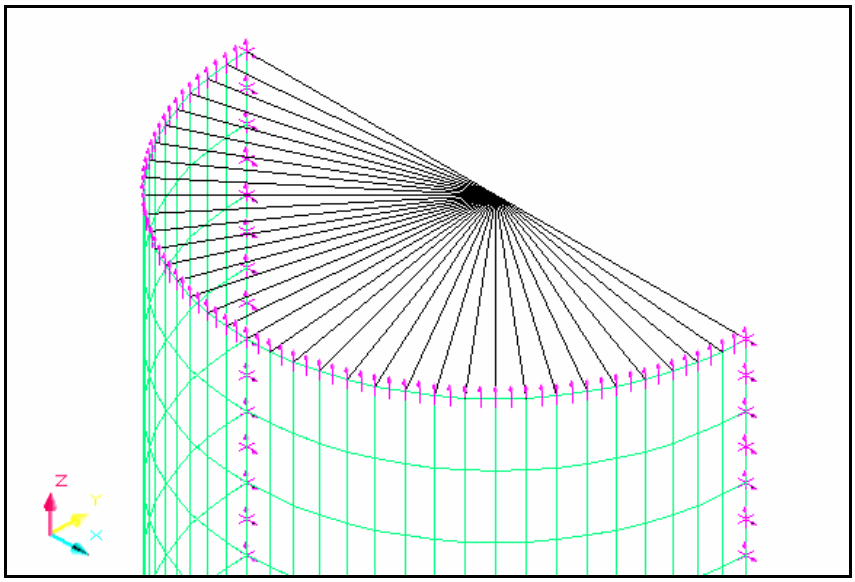

Figure 6-10: Vertical rotational constraints at the ring stiffener elements

6. 7 Matlab model

As mentioned in chapter 3, a Matlab™ model was developed parallel to the Diana model, consisting of 6 spring elements and 6 lumped masses. The model was used as a learning and experimental tool to steer the Diana analysis. The simplicity of this model made it possible to experiment with the load spectra and histories easily. Another powerful advantage of the simplicity is the generation of displacement frames, fast after one another. This enables the Matlab™ user to generate a real-time visualisation of the response. The code for this program is presented in Appendix C and can be found on the CD accompanying this document.

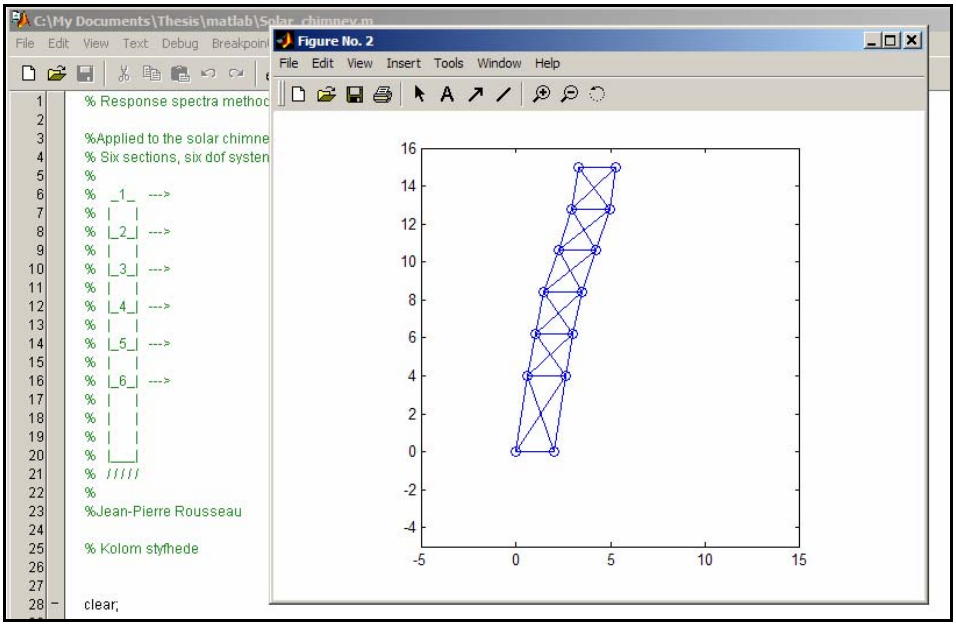

Figure 6-11: The Matlab response visualisation (solar_chimney.m)

6. 8 Results summary table

Table 6-1 summarises the results obtained from the dynamic analysis (figures 6-5 and 6-8).

	30 m/s wind	**42.5 m/s wind**		
Freq	***LC A.1***	***LC M.1***	***LC M.2***	***LC M.3***
Hz	*m*	*m*	*m*	*m*
0 (dc-value)	2.91	5.81	2.18	3.66
0.01	0.435	0.935	0.353	0.587
0.02	0.501	1.26	0.484	0.789
0.03	0.493	1.45	0.573	0.902
0.04	0.473	1.59	0.649	0.972
0.05	0.465	1.71	0.736	1.03
0.06	0.477	1.88	0.864	1.11
0.07	0.524	2.17	1.08	1.24
0.08	0.646	2.78	1.54	1.52
0.09	1.04	4.6	2.9	2.36
0.1	7.92	35.8	26.7	16.7
0.17	0.398	1.93	2.44	2.13
0.18	0.872	4.24	3.86	4.07
0.19	0.256	1.25	0.901	1.09
0.2	0.151	0.739	0.45	0.598
0.22	0.0822	0.404	0.197	0.285
0.3	0.0286	0.142	0.1	0.0135
0.31	0.0281	0.14	0.123	0.0593
0.32	0.0318	0.158	0.191	0.17
0.33	0.039	0.194	0.601	0.754
0.34	0.00621	0.031	0.21	0.356
0.4	0.00929	0.0464	0.0187	0.0732
0.41	0.00828	0.0414	0.0208	0.0629
0.42	0.0109	0.0544	0.0535	0.0669
0.43	0.0339	0.17	0.109	0.185
0.44	0.0306	0.153	0.16	0.154
0.45	0.00852	0.0427	0.0707	0.0475
0.46	0.00394	0.0197	0.0197	0.0188
0.47	0.00149	0.00748	0.019	0.0178
RMS	**8.2207**	**36.9861**	**27.7163**	**17.8918**

Table 6-1: Summary of the dynamic analysis for different load cases

6. 9 Closing remarks

In this chapter it was shown that the structure is sensitive to a variation in damping of up to 3%. The dynamic amplification is also sensitive to maximum gust velocity. A 30m/s and 42.5m/s wind profile is simulated. The first eigen-mode shows the most severe dynamic amplification. Inverting wind directions cause oscillating amplitude amplification at the fifth eigen-mode. The 2nd and 7th modes resonate in all load cases as a result of the wind pressure distribution around the circumference of the tower. This causes dynamic ovalisation. Although this effect is noteworthy, the simplification of the ring stiffener modelling must be kept in mind.

The reader is reminded that simplified assumptions were made concerning the load cases (highly correlated wind profile) and the response representation (computation of the response spectra and not the real-time response).

The results presented in this study focused on the dynamic amplitude displacements only. From these results it is possible to calculate stresses, cracking, internal forces etc. It is possible to view some of these parameters directly from the Diana output files, but since this study focused on the dynamic behaviour; these results were not included in this chapter.

The next, concluding chapter will suggest further steps in utilising these results, show where there is scope for improvement and how it can be used in the economic planning of the solar chimney project.

More detail on the results presented can be found in the appropriate Appendices or on the data CD. A full record of the analysis files, as well as the model files, is also available on the CD.

Chapter 7

CONCLUSIONS AND RECOMMENDATIONS

7. 1 New knowledge

The goal of this study is to better characterise the dynamic response of the solar chimney structure, rather than to produce an exact result. Although the contributing factors in the dynamic force-equilibrium equation are not exact, a wide scope of new insight has been gained through this investigation.

It is has been shown that the traditional design approach used for reinforced chimneys and towers has reached its limit in the context of dynamic behaviour of the solar chimney.

A modal reduced-, frequency-dynamic analysis is proposed and executed on an optimally meshed finite element model. Up to 400 eigen-modes is calculated in order to characterise the mass participation of global and local eigen-shapes.

The complexity of damping in concrete structures, and the difficulty in predicting the energy dissipation in the solar chimney, comes to the reader's attention. An explanation on the physical significance of various forms of damping verifies the proposed equivalent-viscous-damping assumption. For the first time since the chimneys structural investigation realistic damping estimations are made from measured values on existing structures, and utilized in the dynamic analysis.

The magnitude of gusting wind and its effects on the dynamic behaviour of the chimney has not been characterised up to now. A realistic gust history is generated from a power spectral density and applied as a dynamic load on the structure. The vertical power-law static wind profile is critically revised and a new approach is implemented to represent realistic wind conditions.

The results from the dynamic analysis describe the solar chimney's feared resonant behaviour. Response shapes show that global, as well as local, modal vibrations may threaten the chimney's structural integrity. The scope of the first resonance mode's vibrating magnitude is clear from the analysis results. It sketches a new picture of the structure's behaviour in gusting wind conditions.

7. 2 Conclusions

As is shown above, a substantial increase in clarity concerning unknown variables in the dynamic equation has been gained. Although, in reality, the load varies stochastically over the chimney height, a highly correlated load is conservative and a realistic extreme assumption. The unknown factor in dynamic loading has thus greatly been reduced.

The factor of damping will be known with more certainty once the tower is built and the logarithmic decay of dynamic response has been measured. Nevertheless, by literature study about damping characteristics of towers and chimneys, as well as damping mechanisms, a realistic range in damping level has been determined and applied to the model. Thereby, realistic responses have been predicted.

From the results in chapter 6 it can be concluded that noticeable resonance behaviour will occur at yearly reoccurring gusting speeds (30 m/s). At 50-year (or more) reoccurring speeds (45.2 m/s), as shown by records of the De Aar weather station, the resonance amplitude may exceed static limitations as defined in building codes, based on the slenderness ratio of the structure. Although these amplitudes are subject to the percentage of critical damping in the structure, which exact value is unknown, conservative projections of energy dissipation must be kept in mind when estimating conservative amplitudes, as these above-mentioned results are based upon.

The study highlighted the complexity in understanding, estimating and simulating the factors that contribute to dynamic behaviour. It is clear that noticeable resonance will occur, no matter how conservative these factors are regarded to be. The contribution of this study in the development of the solar chimney project is that it proves that dynamic behaviour will certainly be a consideration factor in the geometric design and the reliability estimation of the chimney structure.

7. 3 Recommendations

In chapter 2, two further research developments were presented which may, in future dynamic studies, be able to predict damping accurately by means of mathematical formulation. It was shown how non-linear material behaviour could be modelled in the frequency domain with a dynamic finite element type approach. Further study in this field will enable the developers of the chimney, and for other similar structures, to predict dynamic response with more confidence and certainty.

The load, due to wind, is to a large extent a stochastic phenomenon. A probability approach may describe the chance of different oscillating amplitudes (resulting from a stochastically described load) better in stochastic terms. Finite element based approaches exist to take such factors into

account, as explained in chapter 4. This load uncertainty should be accounted for in further reliability investigation on the solar chimney.

Despite the insight into the wind action and the wind-structure dynamic interaction developed in this study, several unanswered questions remain as to the structural integrity of the solar chimney structure during high velocity wind excitation. The low fundamental eigen-frequency makes it vulnerable to resonant response, which will cause dynamic amplification of pushover deformation of up to a factor 3, considering what is believed to be a realistic damping level. The dynamic response in terms of material (cracking, fatigue) and geometric instability (local/global buckling) must be studied in follow up research. Realistic load cases of correlated wind velocities, as well as wind inversions have been proposed, under which actions these detailed analyses may be performed for realistic estimations of the structural integrity.

REFERENCES:

Publications

Bokelman, K. (1982). *The effect of soil-structure interaction on the dynamic response of a multi-flue chimney*, Thesis presented for the degree of Master of Engineering at the University of Stellenbosch.

Burger, L.W. and Scorgie, Y. (1999). *Meteorological investigation for the solar chimney prooject proposed for Sishen, Northern Cape*, Report No. EMS/99/SCP-01, July 1999.

Chowdhury, I. and Dasgupta, S. P. (2003). *Computation of Rayleigh Damping Coefficients for Large Systems*, Department of Civil Engineering, Indian Institute of Technology, India.

Clough, R.W. and Penzien, J. (1975). *Dynamics of Structures*, McGraw-Hill, New York, N.Y.

Cook, R. D.; Malkus, D. S.; Plesha, M. E.; Witt, R. J. (2002). *Concepts and Applications of Finite Element Analysis*, John Wiley & Sons, New York.

Davenport, A. G. (1967). *Gust loading factors*. Journal of Structural Division, ASCE vol. 93: p11-34.

Drmac, Z., Veselic, K. (2005). *New Fast And Accurate Jacobi Svd Algorithm: I*. Lapack Working Note 169, Netlib - http://www.netlib.org/ .

Dyrbye, C. and Hansen, S.O. (1997). *Wind loads on structures*, John Wiley & Sons, Chichester.

Halabian, A. M.; El Naggar, M. H. (2000). *Probabilistic Analysis of Tall Structures under Strong Winds with Application on TV-Towers*, 8th ASCE Specialty Conference on Probabilistic Mechanics and Structural Reliablility.

Harris R.I., Deaves D.M., (1980). *The structure of strong winds. The wind engineering in the eighties.* Proceedings of CIRIA Conference 12/13 Nov., Construction Industry, Research and Information Association, London, p.4.1-4.93

Horr, A.M.; Safi, M.; Asadpour, N. (2003). *Damped Spectral Element Method for Global Dynamic Analysis of Chimneys*, Tehran, Iran.

Houghton, E.L. and Carruthers, N.B. (1976). *Wind forces on buildings and structures: an introduction*, John Wiley & Sons, New York.

Jackson, R. K. (1978). *A guide to chimney design*. IPC Science and Technology Press, England.

Jeary, A. P. (1974). *Damping measurements from the dynamic behaviour of several large multi-flue chimneys*. The Institution of Civil Engineers, London.

Jeary, A. P. (1986). *Damping in tall buildings*. Conference on the second century of the skyscraper. ASCE/ Council on tall Buildings. Chicago.

MacDonald, A.J. (1975). *Wind loading on buildings*, Applied Science Publishers Ltd, London.

Mainçon, P. (2003). *Introduction to Structural Dynamics Lecture notes*, Department of Civil Engineerng, University of Stellenbosch, South Africa.

O'Leary, D. P. (,2001). *Methods of Conjugate Gradients for Solving Linear Systems* - A Century of Excellence in Measurements, Standards, and Technology, p81-p85, NIST Special Publication 958.

Pinfold, G.M. (1975). *Reinforced Concrete Chimneys and Towers*, Viewpoint Publications, London.

Salzman, A. (2003). *Damping Characteristics of Reinforced and Prestressed Normal- and High-Strength Concrete Beams*. Paper presented for the fulfilment of the degree Doctors of Philosophy, Griffith University, Australia.

Schlaich, J. (1995). *The Solar Chimney: Electricity from the Sun*. Edition Axel Menges

Schlaich, J., Bergermann, R., Schiel, W., Weinrebe, G. (2004) *Sustainable Electricity Generation with Solar Updraft Towers*, Structural Engineering International, p225 – 229.

Schindelin, H., (2002), *Entwurf eines 1500m hohen turms eines solar aufwindkraftwerkes – parameteruntersuchung zur geometrieoptimierung*. Diplomarbeit, Bergische Universität Wuppertal

Smith, Doug, (1974). *A Case Study and Analysis of the Tacoma Narrows Bridge Failure*, Carleton University, Ottawa.

Swamy, R.N. and Rigby, G. (1971). *Dynamic properties of hardened paste, mortar and concrete, Materials and Structures: Research and Testing*, **4**(19), p13-40.

Tedesco, J.M., McDougal, W.G. and Ross, C.A. (1999). *Structural Dynamics: Theory and Applications*, Addison Wesley Longman, Menlo Park, California.

Tilly, G.P. (1986). *Dynamic behaviour of concrete structures*, Elsevier, Amsterdam.

Pidwirny, M. (1995). *CHAPTER 7: Introduction to the Atmosphere.* PhysicalGeography.net - http://www.physicalgeography.net, 2005.

van Dyk, C. (2004). *The realisation of the solar chimney inlet guide vanes.* Thesis presented in partial fulfilment of the requirements for the degree of Master of Civil Engineering, University of Stellenbosch.

Woodhouse, J. (1998). *Linear damping models for structural vibration*, Journal of Sound and Vibration, **215**(3), p547-569

Internet resources

SkyscraperPage.com - http://www.skyscraperpage.com , 2005

Enviromission Ltd. – http://www.enviromission.com.au , 2003

Eskom – http://www.eskom.co.za , 2005

EyeWitness to History - http://www.eyewitnesstohistory.com, 1997. "The San Francisco Earthquake, 1906".

Matlab™ - http://www.mathworks.com, 2005

PHYS 224A, Thermal Physics – http://faculty.washington.edu/cobden/224/index.htm, 2003

Schlaich Bergermann – http://www.sbp.de/en/fla/projects/solar/aufwind/index.htm, 2003

TNO Diana - http://www.tnodiana.com, 2005

Wikipedia, the free encyclopedia - http://en.wikipedia.org/wiki/Main_Page, 2005

Personal correspondence

Adam Goliger – CSIR/WNNR: Correspondence regarding gust-wind measurement instrumentation.

Alan Jeary –University of Western Sydney, Australia: Correspondence with regard to damping in chimneys.

Cobus van Dyk – University of Stellenbosch, Structural department: Personal correspondence regarding previous research on the solar chimney.

Dr. Phillippe Maincon – University of Stellenbosch, Structural department: Personal correspondence regarding spectral analysis.

Riaan Smit - South Africa Weather Bureau Cape Town office: Personal discussion with regard to downburst activity from thunderclouds

Tracey Gill - South African weather Bureau Pretoria Office: Correspondence with regard to upper air measurements at Upington and De Aar.

APPENDIX A

DEVELOPMENT OF A WIND GUST ACCELOROMETER

A.1 Wind data

The solar chimney provides a few new challenges regarding wind resonance: There is no structure in the world with the same dimensions as this one. No structure's eigen-frequencies are in the solar chimney's range. The structure's geometry is relatively fixed due to very specific physics requirements in order to operate efficiently. Very little damping exists due to the absence of masonry walls, office separators, windows etc. Although the solar chimney has been subjected to regular wind design for high rise buildings in past research, this is not a realistic scenario when considering a structure of such massive dimensions and low eigen-frequency.

The mathematical way to approach the problem is to characterise the frequency composition of gusting wind and see to what degree it awakens the resonating modes of vibration. The lowest eigen-frequencies of the chimney are between 0.1 Hz and 0.5Hz. This implies a re-occurrence time of between 10 and 2 seconds. To accommodate the shortest re-occurrence time, at least ten measurements between the time-interval must be taken to assure a reliable break-up of frequency components. This implies the coarsest measuring rate may be one measurement per 0.2 seconds, or 5 Hz.

Unfortunately all wind data available in South Africa, according to the national weather bureau, is 10 second data based on 3 second averages. Even the anemometers available on the market can only provide a 3 second average based on the revolutions of a three armed cup. After extensive searching for 5 Hz gust data, it was decided to design an in-house strain-reading based wind meter and to take samples and investigate independently. Measurements were first taken on the 31st of June '05 at the Engineering faculty building's roof (5 stories high). The building is located in an urban area, thus the gust profile was largely influenced by houses, trees and other urban obstructions. The second set of measurements was taken on the main building of the University of Port Elizabeth on the 20th of July '05. The building is 20 stories high and is surrounded by a scrub-vegetation nature reserve near the sea. Port Elizabeth is known for severe gusting wind conditions (30m/s average), as was experienced on this day. The results of both locations confirmed that

Davenport's equation for gust winds fit the gust behaviour in South Africa, for low speeds, high frequency measurements as well as severe gust conditions. This will be shown in appendix B.

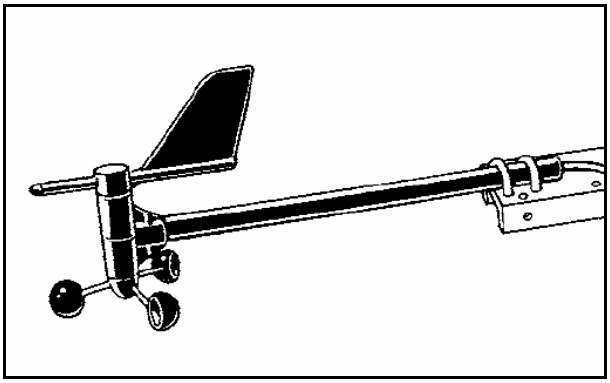

Figure A-1: A conventional wind meter

A.2 The wind meter

The goal of designing an in-house tool was to measure the frequency components of gust at a sample rate much higher than that available on the market, and to compare it with a artificially generated gust history by means of Davenport's power spectral density (PSD) presented in Appendix B. Most anemometers work with a rotating part of which the revolutions are measured. The disadvantage of such a device is that the measuring frequency is dependant on the wind speed. Another criterion for the measuring device is to react to wind speed changes instantaneously. As little momentum as possible must be stored in the part of the instrument measuring the wind energy.

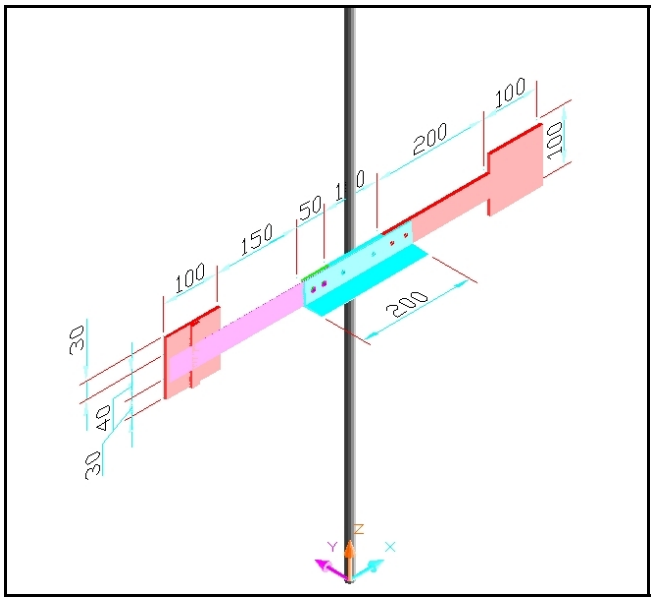

Figure A-2: The developed strain-gauge wind meter

It was decided to base the measuring component on strain-gauge readings. A cantilever plate would have a rectangular pressure surface which will result in a line-load at the free end of the cantilever. This would result in a moment at the fixed end, which in turn causes strains at the upper and bottom surfaces of the plate. Two strain-gauges read the difference in electrical potential energy of a small current running through them. This is converted to a digital output stream to a computer, which reads the energy difference as mili-volts per volt (mV/V). By mathematical calibration it can be recalculated to pressure or wind speed.

A.3 The design sheet

Design for strain measuring windmeter:

Max strain capability

Known capacity:	3 = 2 * 2.14 * ε / 4 000		
ε =	2803.730	µm/m	
	0.002803730	m/m	
E =	210	GPa	
σmax =	588.783	MPa	

Safety Factor: 3

σ =	196.261	Mpa

Section Property I: 3.333E-12 M^4

Moment = σ * I / y

M =	1.308	Nm

Force:

arm =	0.2	m
F =	6.542	N

Wind: F = 0.63 * Cd * A * v^2

Cd =	1.18	flat rectangular surfaces ratio 1:1
A =	0.01	m2
F =	6.542	
v =	29.665	m/s

Calibration

Reading: 50
equals 0.05 mV/V
equals 6.633 m/s wind

Factor 0.132

APPENDIX B

POWER SPECTRAL DENSITY TO TIME HISTORY AND BACK

B.1 Understanding the PSD concept

A power spectral density (PSD) is a powerful tool when random behaviour of a process needs to be simulated. It describes the amplitude-frequency distribution of a process by normalising each amplitude-frequency discreet point with its own frequency. This is done to overcome the time increment constraint when measuring a process. When two measurements, time apart, is recorded in a amplitude time history measurements (e.g. gusting wind), the amplitude energy over a time interval of Δt is contained or represented by that discreet point measurement. It would be more general to have a mathematical description of the amplitude-energy over frequency that is not time-step dependant since the time step is subjective to the measured data (which may differ from one case to another). This can be achieved by squaring the amplitude of the discreet Fourier transform (DFT) and dividing with the frequency step Δf.

As this procedure removes the frequency, it becomes problematic when one needs to reverse the process. In the following Matlab-code the Davenport PSD is reversed-engineered to generate a time-history of gust. Different time steps and number of measurements were tested to see what combinations resulted in a realistic gust history representation. The time-step proved to dominate the sensitivity of the generated history, however, the margins of variation was very distinct and not extremely different. The most conservative amplitude spectrum resulting from the trail tests was used in the dynamic analysis. Figure B-1 shows the non-dimensional spectrum (see chapter 5).

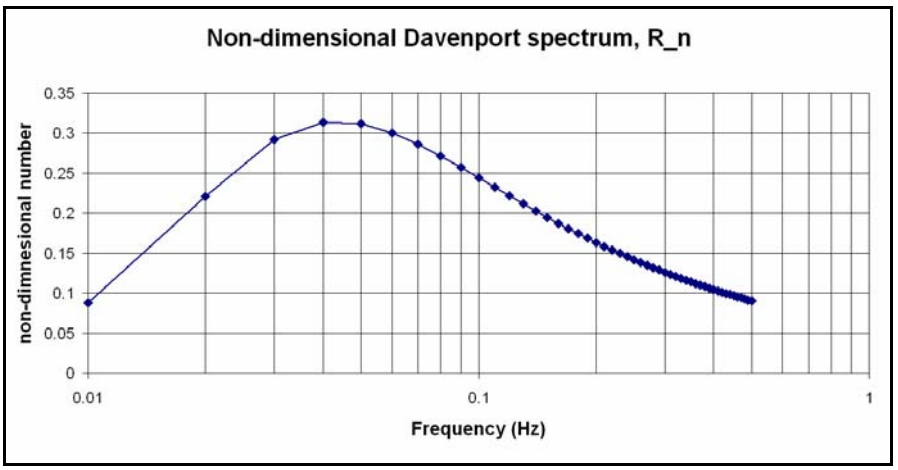

Figure B-1: Davenport's model

B.2 The PSD Matlab code

```
% Davenport spectral density function

%Constants
clear;

L = 1200;   %m
U = 30;     %m/s
sigu = 3    %m/s

T=60;       %recorded time (s)
dt=0.1;     %time step increment
fs = 1/dt;  %measuring frequency
N=T/dt;     %number of time steps
df = 1/T    %frequency increment
maksf = N*df    %maximum frequency on spectra

phi = 2*pi*abs(rand(N,1));  %random phase angle

n=df:df:maksf;
t=dt:dt:T;


S_u = (sigu^2)*(2*((n*L/U).^2)./(3*(1+(n*L/U).^2).^(4/3)))./n;
% davenport power spectral density function

fig =figure(1);         %davenport's PSD plot
plot(n,S_u);
axis([0.01 1 0 100]);   % Get the axes right
drawnow;                % and show it all on the screen for a nice
movie effect


A = (sqrt(2*S_u*df*2*pi));  %computing the amplitude spectrum

fig =figure(2);         %plotting the amplitude spectrum
plot(n,A);
axis([0.01 1 0 10]);    % Get the axes right
drawnow;                % and show it all on the screen for a nice
movie effect

v = N*A.*(exp(i*phi')); % adding the random phase angle

vh = real(ifft(v))+30;  % inverse fourier transform to
                        % obtain the time history
fig =figure(3);
plot(t,vh);

Sp = abs(fft(vh))/(N/2);    % compute the amp spectrum from the time
history
Sp(1,1)=Sp(1,1)/2;
vhv=vh';

fig     =
figure(4);clf;set(fig,'DoubleBuffer','on');set(fig,'color',[1 1 1]);
```

```
plot(n,Sp);
axis([0.01 1 0 10]);          % Get the axes right
drawnow;                      % and show it all on the screen
```

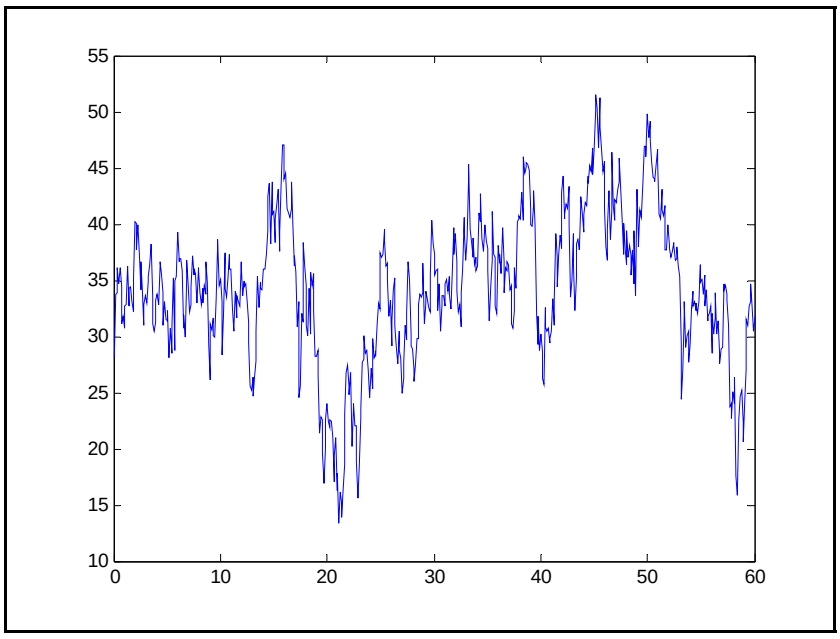

Figure B-2: Artificial wind gust history (30m/s average)

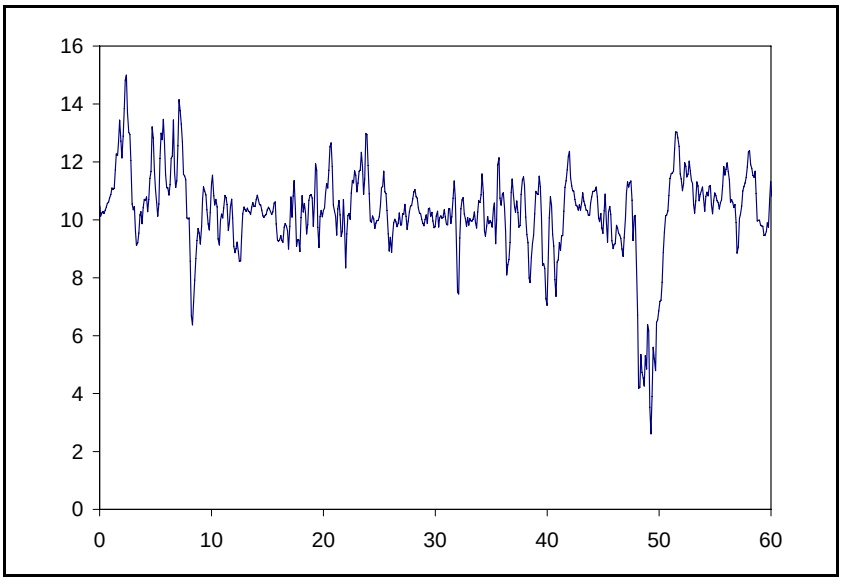

Figure B-3: Gust history measured at UPE, Port Elizabeth (10m/s average)

APPENDIX C

MATLAB DYNAMIC SIMULATION

C.1 Lumped Mass model

The Eurocode, as well as other international codes, suggests different methods for earthquake design, varying in complexity. One such method is the lumped mass cantilever model. A building can be modelled with beam elements representing the vertical members and their stiffness, and lumped masses at the nodes representing the dead and live loads at each floor. A simplified modal dynamic analysis is then executed by spreading the earthquake acceleration load over the height of the building, applying a mass-weighted portion at each node.

The same strategy was followed in conceptualising the modal dynamic analysis approach for the solar chimney. Although the end results was computed with a fully meshed three dimensional model, a lumped mass model was developed parallel to the finite element model in order to understand concepts such as mass participation, reduction of modal degrees of freedom and applied wind load. One major advantage of the Matlab program is its simplicity. The wind load was also applied in real time instead of in the frequency domain. The result is that the model's response could be visualized in real time. If the Fourier transform of the response at the top node is taken, the same type of response spectrum will result as presented in chapter 6. Otherwise said, if the results in chapter 6 are inverse-Fourier transformed with a random phase angle, a real-time response can be calculated.

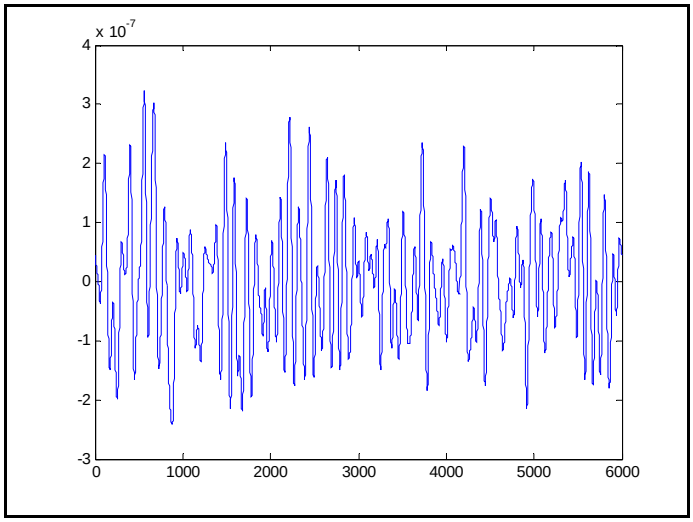

Figure C-1: Time history of the matlab model's response

C.2 The lumped mass model's code:

```
% Response spectra method
% A lumped mass model
% applied to the solar chimney
% Six sections, six dof system
%    _1_    --->
%   |   |
%   |_2_|   --->
%   |   |
%   |_3_|   --->
%   |   |
%   |_4_|   --->
%   |   |
%   |_5_|   --->
%   |   |
%   |_6_|   --->
%   |   |
%   |   |
%   |   |
%   |___|
%   / / / / /
%
%Jean-Pierre Rousseau

clear;

% general properties
E = 30E9;         %Pa E-modulus of concrete
Es = 170E9;       % Pa E-mod of steel

I1 = 482.55E3;   %m^4
I2 = 482.55E3;   %m^4
I3 = 635.36E3;   %m^4
I4 = 1.3077E6;   %m^4
I5 = 1.9802E6;   %m^4
I6 = 2.9278E6;   %m^4
I7 = 3.2336E6;

Is = pi*80^3*0.000; %m^4

A1 = 150.80; %m^2
A2 = 150.80; %m^2
A3 = 198.55; %m^2
A4 = 408.66; %m^2
A5 = 618.77; %m^2
A6 = 914.83; %m^2
A7 = 1.0103E3;

L1 = 220;       %m

% Stffnesses
f=0.02;%0.0833333;  %a factor to adapt the eigenfrequencies to match
the solar chimney's.

k1 = (12*E*I1/L1^3+12*Es*Is/L1^3)*f;
```

```
k2 = (12*E*I2/L1^3+12*Es*Is/L1^3)*f;
k3 = (12*E*I3/L1^3+12*Es*Is/L1^3)*f;
k4 = (12*E*I4/L1^3+12*Es*Is/L1^3)*f;
k5 = (12*E*I5/L1^3+12*Es*Is/L1^3)*f;
k6 = (12*E*I6/L1^3+12*Es*Is/L1^3)*f;
k7 = (12*E*I7/L1^3+12*Es*Is/L1^3)*f;

% Stiffness matrix

K = [ k1    -k1      0      0       0       0   0
     -k1  (k1+k2)   -k2     0       0       0   0
      0     -k2     (k2+k3)     -k3     0       0   0
      0     0       -k3     (k3+k4)     -k4     0   0
      0     0       0       -k4     (k4+k5)     -k5 0
      0     0       0       0       -k5     (k5+k6)     -k6
      0     0       0       0       0       -k6     (k6+k7) ]

% section weights

dens = 2500 %kg/m3

M1=A1*L1*dens;    %kg
M2=A2*L1*dens;
M3=A3*L1*dens;
M4=A4*L1*dens;
M5=A5*L1*dens;
M6=A6*L1*dens;
M7=A7*L1*dens;


% Mass matrix

M =[ M1  0   0   0   0   0   0
        0   M2  0   0   0   0   0
        0   0   M3  0   0   0   0
        0   0   0   M4  0   0   0
        0   0   0   0   M5  0   0
        0   0   0   0   0   M6  0
        0   0   0   0   0   0   M7];

[phi,h] = eig(K,M)     %mode shapes

w=diag(sqrt(h));
f=w/(2*pi);           % Eigenfrequencies in cycles/sec (Hz)
T=1./f;

%Normalize the eigen vectors

Np = size(phi(:,1));
for k=1:Np(1)
    p(k)=max(abs(phi(:,k)));
    ph(:,k)=phi(:,k)./p(k);
end
ph

% Modal mass participation
```

```
m1=phi'*M*phi
m2=ph'*M*ph
r=[1 1 1 1 1 1 1]'
L=phi'*M*r

eM=L.^2


T1 = sum(eM)
T2 = sum(diag(M))

ePM = eM/T1*100

% Rayleigh damping calibration

alpha=0.005;
beta=0.5;

z = 0.01:0.01:0.5;
for  k=1:50
    bet_v(k) = (alpha/(2*z(k)) + beta*z(k)/2);
end

fig     =
figure(1);clf;set(fig,'DoubleBuffer','on');set(fig,'color',[1 1 1]);
plot(z,bet_v);hold on;


C = beta*K+alpha*M;

% Time steps

dt = 0.1;     % delta time

% The time history
T_H = dlmread('wind.asc','\t'); %The wind load file
T_H = [T_H*3     T_H*2.8     T_H*2.2      T_H*1.2     T_H*1.1
T_H*1       T_H*0.9];

% matrix of time history space
dim_N = size(T_H);  % Number of time-steps
N = dim_N(1);

X_f = zeros(7,N);   % matrix of displacements space
G_f = zeros(N,7);
for k=2:(N/2)
    G_f(k,:)=1;
end

dw = 2*pi/N/dt;     % delta omega

vo_f = fft(T_H);    %fourier transform
v_f = vo_f.*G_f;

for k=1:N
```

```
    w = dw*(k-1);
    L = (K+i*w*C-(w^2)*M);
    X_f(:,k) = L\(v_f(k,:)');

end

X = ifft(X_f');

%Animation Plot
fig     =
figure(2);clf;set(fig,'DoubleBuffer','on');set(fig,'color',[1 1 1]);
dispf = 5e6;   % amplify the displacements to make them visible
%%%%%%%%%%
for t = 1:3000;    % for each movie frame
    d1 = dispf*real(X(t,1));
    d2 = dispf*real(X(t,2));
    d3 = dispf*real(X(t,3));
    d4 = dispf*real(X(t,4));
    d5 = dispf*real(X(t,5));
    d6 = dispf*real(X(t,6));



    DisNodPos1 = [d1 d2 d3 d4 d5 d6 0];
    DisNodPos2 = [15 12.8 10.6 8.4 6.2 4 0];
    floors1 = [d1 d1+2 d2     d2+2 d3     d3+2 d4  d4+2 d5   d5+2 d6
d6+2 0 +2 d6 d6+2 d5 d5+2 d4 d4+2 d3 d3+2 d2 d2+2 d1 d1+2];
    floors2 = [15 15      12.8 12.8   10.6 10.6   8.4 8.4     6.2 6.2
4    4        0 0 4 4 6.2 6.2 8.4 8.4 10.6 10.6 12.8 12.8 15 15];

    clf;
        % Plot the elements
        plot(DisNodPos1,DisNodPos2,'bo-');hold on;
        plot(DisNodPos1+2,DisNodPos2,'bo-');hold on;
        plot(floors1,floors2,'bo-');hold on;


    axis equal;axis([-5 15 -5 16]);        % Get the axes right
    drawnow;                               % and show it all on the
screen for a nice movie effect
    pause(0.01);
end

fig     =
figure(3);clf;set(fig,'DoubleBuffer','on');set(fig,'color',[1 1 1]);
plot(real(X(:,4)));
fig     =
figure(4);clf;set(fig,'DoubleBuffer','on');set(fig,'color',[1 1 1]);
plot(real(X(:,5)));
fig     =
figure(5);clf;set(fig,'DoubleBuffer','on');set(fig,'color',[1 1 1]);
plot(real(X(:,6)));
fig     =
figure(6);clf;set(fig,'DoubleBuffer','on');set(fig,'color',[1 1 1]);
plot(abs(v_f(:,6)));
fig     =
```

```
figure(7);clf;set(fig,'DoubleBuffer','on');set(fig,'color',[1 1 1]);
plot(FFTSHIFT(abs(v_f(:,6))));

% This code is only for explanitory purposes. The results obtained
% from this analysis is inacurate as the load distribution over the
% structure is not realistic. It only emulates the solar chimney
% behaviour. NB. THIS SIMULATION IS NOT EXACT!
```

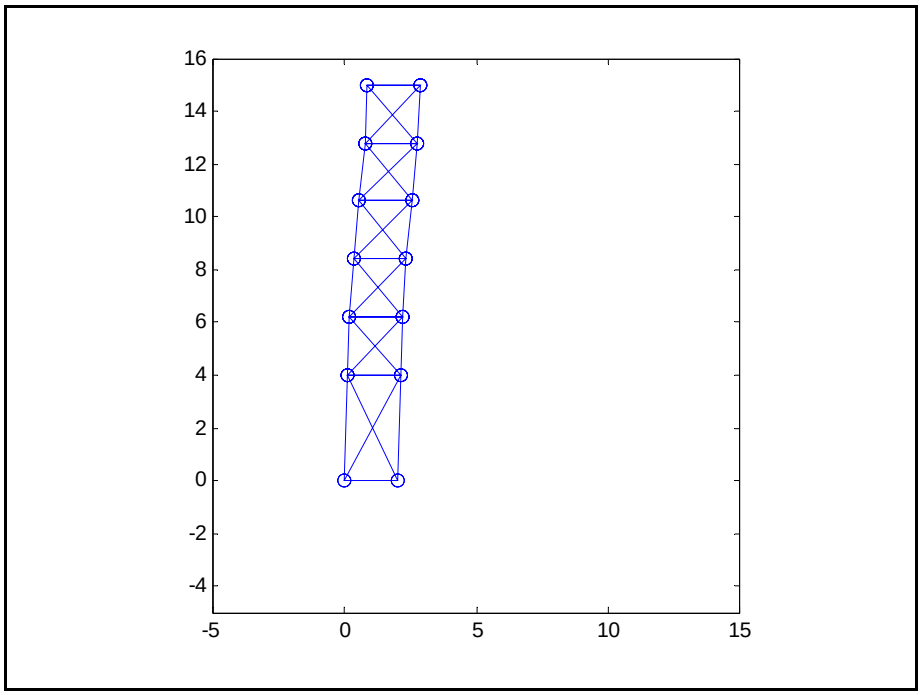

Figure C-2: Real-time visualization of the lumped massed Matlab model

APPENDIX D

COMPUTATION OF THE STATIC WIND PROFILE

D.3 Mathematical composition

As explained in chapter 5, the vertical wind profile can be described in three layers: (1) Surface – highly influenced by friction, (2) boundary layer- partially influenced by surface friction and (3) the geostrophic layer where wind follows the isobar direction unaffected by friction, and fully dependant on coriolis force. The wind profile in the last mentioned layer varies according to the prevalent weather system, but the root mean square (RMS) value will stay fairly constant over a short interval of time (between 10min to an hour). Thus the wind profile above the boundary layer can be assumed constant over height at the average peak velocity measured in the geostrophic layer.

The boundary layer profile can be computed with the corrected logarithmic profile (5-2) only. Between ground and about 300m, the last three terms does not contribute significantly, and assuming d=0, the corrected logarithmic profile nearly matches the logarithmic profile. Such small difference between the two profiles, so close to the base of the structure, will hardly be noticed in the first modal response. Thus it is considered reasonable to simulate the entire wind profile up to 1000m above ground level

D.4 Comparing the profiles

The following sheet shows the difference between the logarithmic and the corrected logarithmic profiles. Even at higher altitudes the logarithmic profile is still fairly similar to the corrected logarithmic profile. The excel equations for both profiles is shown in the second and third line of the data sheet. The rest of the values are all based on these equations. Figure D-1 compares the average and maximum profiles to the previously assumed power law profile.

A	B	C	D	E	F
	u*	**von karman**	**z0**	**zg**	
height	0.94	0.4	0.05	1.00E+03	7.71E-05
0	10	10.00			
10	14.57	**=$B$3/$C$3*(LN(A5/$D$3)+5.75*(A5/$E$3)-1.88*(A5/$E$3)^2-1.33*(A5/$E$3)^3+0.25*(A5/$E$3)^4)**			
20	**=$B$1/$C$3*LN(A6/$D$3)**				
40	18.38	16.33			
60	19.50	17.56			
80	20.29	18.49			
100	20.90	19.28			

A	B	C	D	E	F					
200	22.81	22.12								
300	23.92	24.16								
400	24.71	25.78								
500	25.33	27.10								
600	25.83	28.15								
700	26.25	28.96								
800	26.62	29.54								
900	26.94	29.88								
1000	27.23	30.00								
1200	27.74	30								
1300	27.96	30								
1400	28.16	30								
1500	28.35	30								

Table D-1: Computation of the Logarithmic profiles

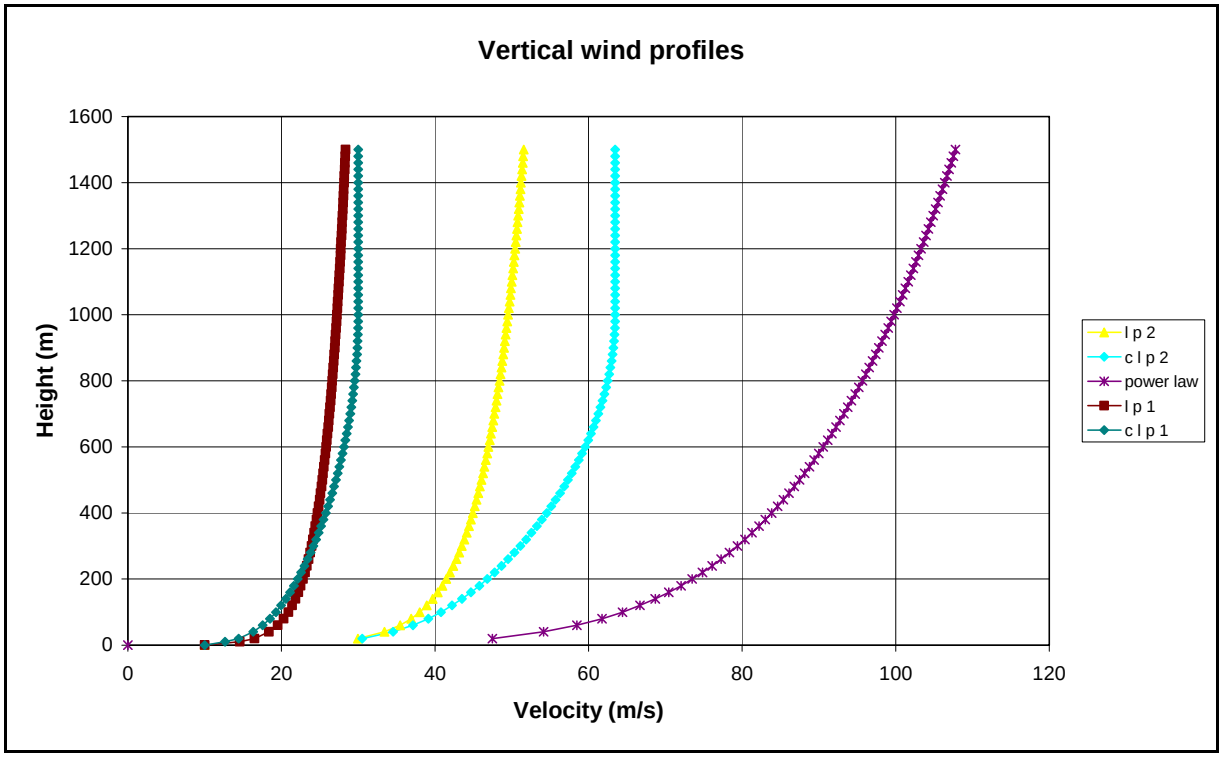

Figure D-1: Comparative vertical wind profiles

APPENDIX E

JDIANA: TNO DIANA AND JAVA

E.1 Background

In order to understand the need to develop a custom alternative interface for TNO Diana, it is important to understand how Diana is used in a research context and how it communicates between its different components.

The heart of Diana is the solver, the part of the package that handles the mathematical computation of a model. It reads a text file containing all the information of the model and builds a calculation storage file named the filos file. Here it can store temporary and intermediate calculation results to be accessed later. The filos file operates like a random access memory (RAM) extension while the calculation runs. Although this process might be slower for small models than utilizing RAM directly, it is more stable and much less of a risk when analysing large models that might take a few days to reach convergence. Furthermore it enables the solver to run effectively on very slow PC's as well. The result is written in a text-base file and the filos file left as is to enable the user to use the stored calculation database in a next iteration, saving the user the time of re-analysing the whole model.

The graphical user interface of TNO Diana, named iDiana, operates independently from the solver programme. It utilizes a 3d-CAD like interface in parallel with a command line based input language, where the user can build the model interactively or by command input, defining parts, their mesh densities, reinforcements, constraints and loads. The command line interface can effectively be utilized by running script files to execute repetitive modelling commands. The command line history is stored in such a script file which can be executed later if the model is lost and need to be re-generated and can easily be manipulated with a spreadsheet programme such as Excel. After a model has been defined in iDiana, a Diana script file is generated with a .dat extension, which is the input file for the solver programme described above.

Between these two interfaces a level of input-file manipulation was needed for possible iterative computations for the solar chimney. Once the .dat file is generated, it cannot be manipulated by iDiana anymore. The iDiana model needs to be adjusted and a new data file generated, or the old one overwritten. This implies that small changes such as reinforcement cover, wind load variation,

material strength etc. needs to be updated through the graphical user interface. In the case of reinforcement, the whole model needs to be re-detailed in order to change a small difference in a one shell that affects the whole structure. This is extremely time-consuming.

Another time-consuming parameter experienced with the iDiana interface is the definition of area or shell loads. In the case of wind, where the pressure varies with height and parameter, it would be extremely tedious to define every individual shell's area load in the graphical interface.

With these needs in mind a Java program was developed with which a user can read a Diana .dat file to edit parameters. The .dat file is stored in ANSI format, which makes it easy to edit in a text editor such as Notepad. The problem with manual editing lies in the complexity of the .dat file and the way in which parameters and data is sorted and stored. The Java interface makes it possible to sort the parameters, manipulate them mathematically with custom modules, and write them back into the .dat file, write a new .dat file or write a portion of the .dat file. Being able to access different segments of the file, it made the calculation of various parameters much more convenient. The program and source code is available on the CD accompanying this document.

E.2 Diagramatic representation

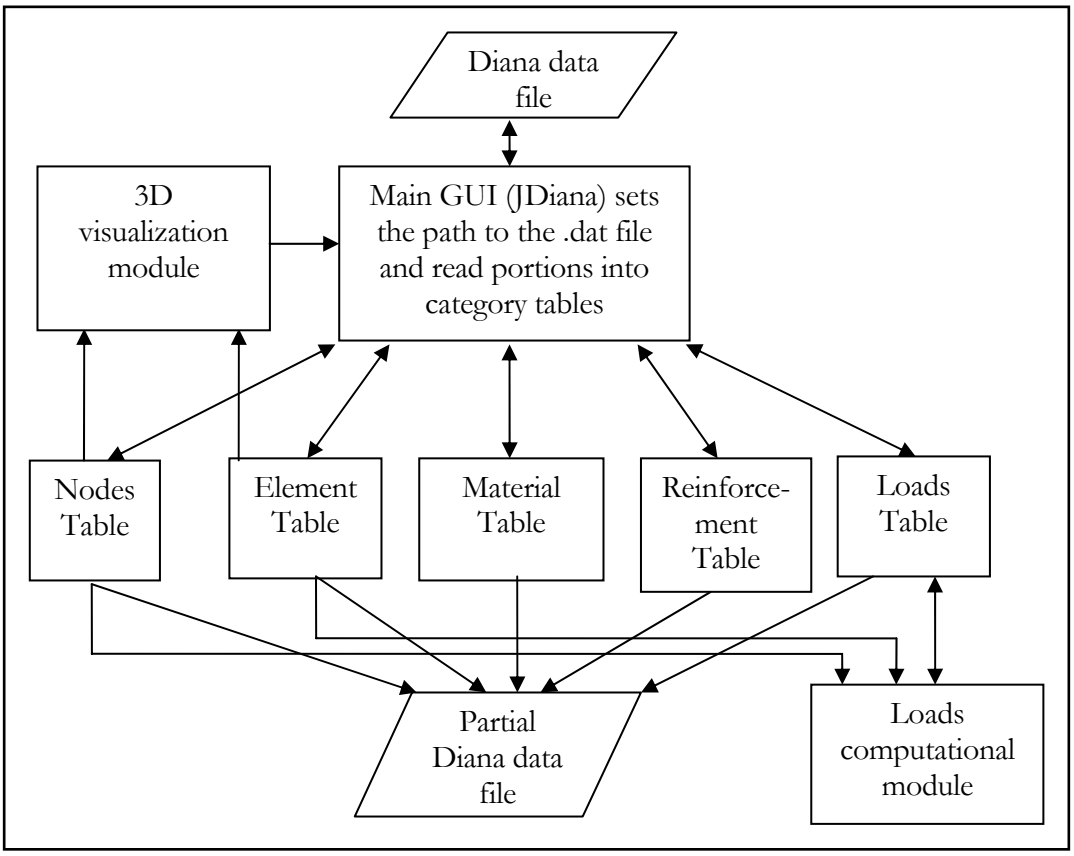

Figure E-1: Graphical representation of iDiana